PRODUCTION OF NEUTRON-RICH RARE ISOTOPES NEAR N = 126 VIA MEDIUM ENERGY FRAGMENTATION

By

Kenneth Taylor Haak

A DISSERTATION

Submitted to
Michigan State University
in partial fulfillment of requirements
for the degree of

Physics and Astronomy - Doctor of Philosophy

2024

ABSTRACT

The production of neutron-rich rare isotopes near $N = 126$ seeks to elucidate the limit of existence for nuclear matter and explain the origin of heavy elements. In the most recent development, eight new isotopes, ^{182,183}Tm, ^{186,187}Yb, ^{189,190}Lu, and ^{191,192}Hf, were discovered in medium energy fragmentation and are presented here. This work marks the first time a ^{198}Pt primary beam was used to produce neutron-rich heavy isotopes near $N = 126$. Two primary beam energies were explored, 85 MeV/u and 186 MeV/u. A total of 60 production cross sections were measured in the 85 MeV/u ^{198}Pt + ^{9}Be reaction, and 50 production cross sections were measured in the 85 MeV/u ^{198}Pt + Ni reaction. The ^{198}Pt + ^{9}Be cross sections were compared to `EPAX3` , `COFRA` , `ABRABLA07` , and `LISEAA` , showing the most consistent agreement with `LISEAA` . The Ni target cross sections were systematically greater than the Be target cross sections by roughly an order of magnitude. This result suggests that heavy neutron-rich targets may aid in production of neutron-rich isotopes for medium energy fragmentation. Several pick-up reactions between ^{198}Pt and three separate targets (Be, Ni, C) were observed for the first time at intermediate energies. Nuclei up to two neutrons greater than the primary beam were observed. This work also led to the development of a novel charge state analysis for cross section calculations. The probability distribution for the charge state of the projectile residue immediately after reaction is generated from Monte Carlo calculations and optimization to experimental data. By using this new method, it was observed that not all primary beam electrons are stripped from the projectile residue during a fragmentation reaction. The number of electrons which remain on the projectile residue immediately after reaction (named Ne_R) were observed to be inversely proportional to the number of protons removed in reaction.

I dedicate this work to my family.
I hope I have brought a sense of pride, how ever small, to each of your lives.

TABLE OF CONTENTS

LIST OF TABLES

LIST OF FIGURES

Chapter 1

Introduction

Terra incognita is Latin for unexplored territory. This phrase was first used in Ptolemy's *Geography* around the year 150 AD and was later reintroduced during the Age of Exploration in the 15th century. Unexplored territory was often either costly or challenging to reach. It required a great deal of resources and ingenuity to make it through rough waters, thick jungles, and over steep mountains. Likewise, the Chart of Nuclides (see Figure 1.1), in the context of nuclear physics, contains several regions which are difficult to access. These areas draw a parallel to the unexplored territory on old maps of Earth, due to cost and technological constraints of discovering a new nuclide. Therefore, the unexplored area of the Chart of Nuclides has been aptly named Terra Incognita [1].

Since the discovery of the first unbound nuclei [2], there has been a continuous effort to define the limits of existence for nuclear matter by charting the unexplored territory of what would eventually be represented as the Chart of Nuclides. Currently, the neutron-rich region near neutron number $N = 126$ is the new world, ripe for discovery. This region is relatively unexplored compared to other areas in the Chart of Nuclides. The nuclei in this region also hold the answers to the creation of the heaviest elements found in nature [3]. The latest discoveries of neutron-rich rare isotopes near $N = 126$ are over a decade old and were produced by high energy fragmentation of heavy elements, such as lead and uranium [4, 5]. The next step toward pushing the boundary of discovery was carried out with medium energy fragmentation of ^{198}Pt and is described in this work.

1.1 Background

A nuclide is often addressed with the misnomer “isotope." Isotopes are atoms of the same element that differ by the number of neutrons contained in the nucleus. A nuclide is a distinct nucleus of an atom, characterized by a specific number of protons and neutrons. In this thesis, the common practice of using the term isotope synonymously with nuclide is adopted. There are roughly 280 isotopes found naturally on Earth [8], which is a small subset of the 3373 isotopes that have been discovered in the course of human history [9]. Most natural elements contain multiple isotopes in varying abundances. For example, platinum occurs naturally in six different isotopes ^{190,192,194,195,196,198}Pt, which occur at abundances 0.01%, 0.8%, 32.9%, 33.8%, 25.2%, and 7.4%,

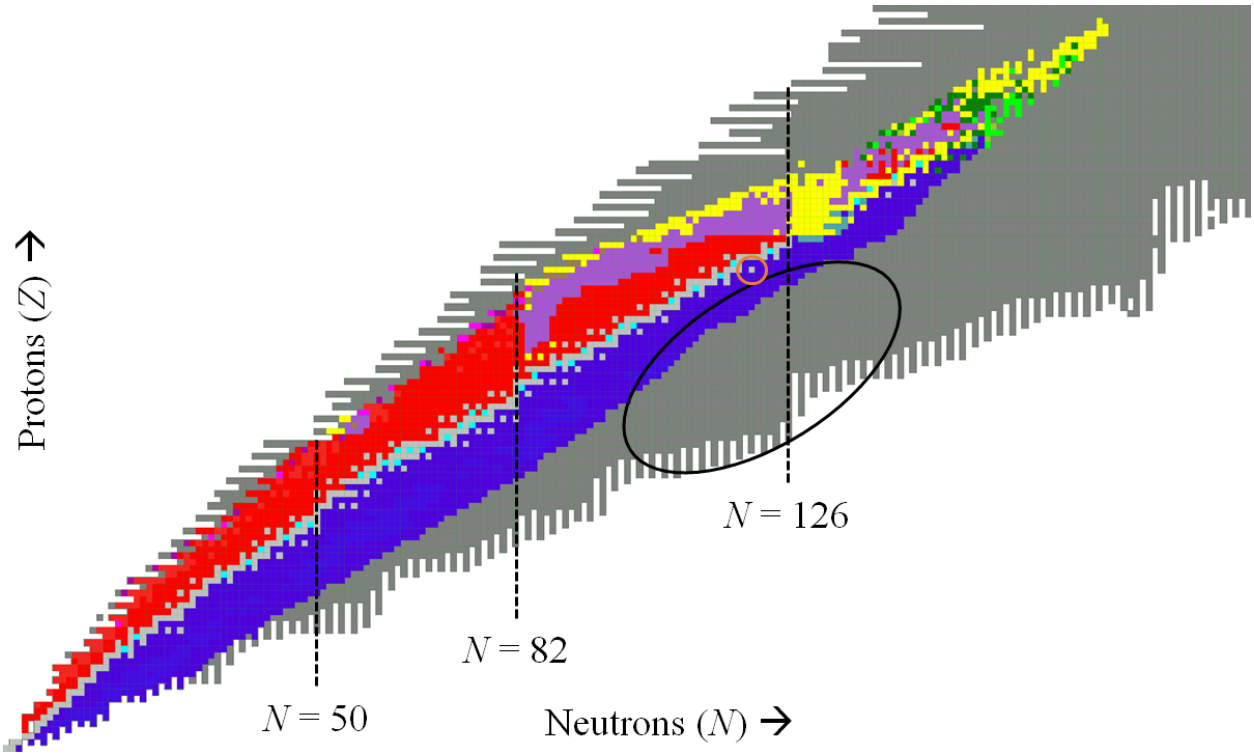

Figure 1.1: The Chart of Nuclides was generated in LISE^{++} using the UNDEF1 mass model [6, 7]. The magic numbers N = 126, 82, and 50 are denoted with a dashed black line. The region of interest for this work is denoted by the ellipse drawn with a solid black line. The orange circle slightly to the left of N = 126 denotes ^{198}Pt, the primary beam used in both fragmentation experiments presented in this thesis. The different colors on the chart indicate different types of radioactive decay. Red is β+ decay, blue is $\beta-$ decay, and yellow is α decay. Stable nuclei are shown in light grey, and terra incognita is shown in dark grey.

respectively [10].

Atomic nuclei have varying degrees of radioactive stability. Radioactivity is observed when a nucleus spontaneously emits energy as a particle or a wave. Commonly emitted particles include α, β^-, or β^+ particles, which are more easily understood as a helium nucleus, an electron, and a positron, respectively. These processes change of the number of neutrons and protons of the nucleus and thus the identity of the nuclide. Certain nuclides are sufficiently stable that an emission of one of these particles has never been observed, and these are considered “stable." Stable nuclei comprise the majority of matter we see in our everyday life, whether it is the atomic nuclei of ^{12}C in the soil, ^{14}N in the air, or ^{16}O in water. The Chart of Nuclides helps visualize stable nuclides with a line that runs through the middle of the chart (shown in light grey in Figure 1.1)

Nuclei can also be bound or unbound. Certain combinations of protons and neutrons do not stick together and exist for incredibly short times, which are shorter than the time for a neutron or proton to cross the nucleus. This may occur if protons are added to an already proton-rich nucleus or neutrons are added to an already neutron-rich nucleus. For example, if one neutron is added to ^{12}Be to create ^{13}Be, the extra neutron simply “drips" out of the nucleus within an incredibly short time interval. This perspective of the atomic nucleus gives rise to the term “dripline." The dripline is the boundary of the Chart of Nuclides, and it defines the limits of existence for nuclear matter. Quantitatively, an unbound nuclide beyond the neutron dripline can be defined by its neutron separation energy, S_n. If S_n is negative, the nuclide is unbound. For instance, measurements have shown that ^{13}Be has $S_n = -510$ keV, indicating it is unbound [11].

A relatively small portion of the Chart of Nuclides has been explored to the dripline. For each element, the proton dripline is defined by the lightest bound isotope, while the neutron dripline is defined by the heaviest bound isotope. The proton dripline has been established up to ^{26}P and the neutron dripline has been established up to ^{39}Na [9, 12]. While these nuclides are the complete extent of the dripline from hydrogen, there are several scattered observations of unbound nuclides beyond these limits, such as ^{54}Cu which demonstrates the proton dripline for copper. The dark grey region in Figure 1.1 shows how far the dripline could possibly extend away from stability as

nuclides increase in mass. However, this region is only a theoretical prediction. The true extent of the Chart of Nuclides is uncertain and better constrained with new discoveries of nuclides at the dripline.

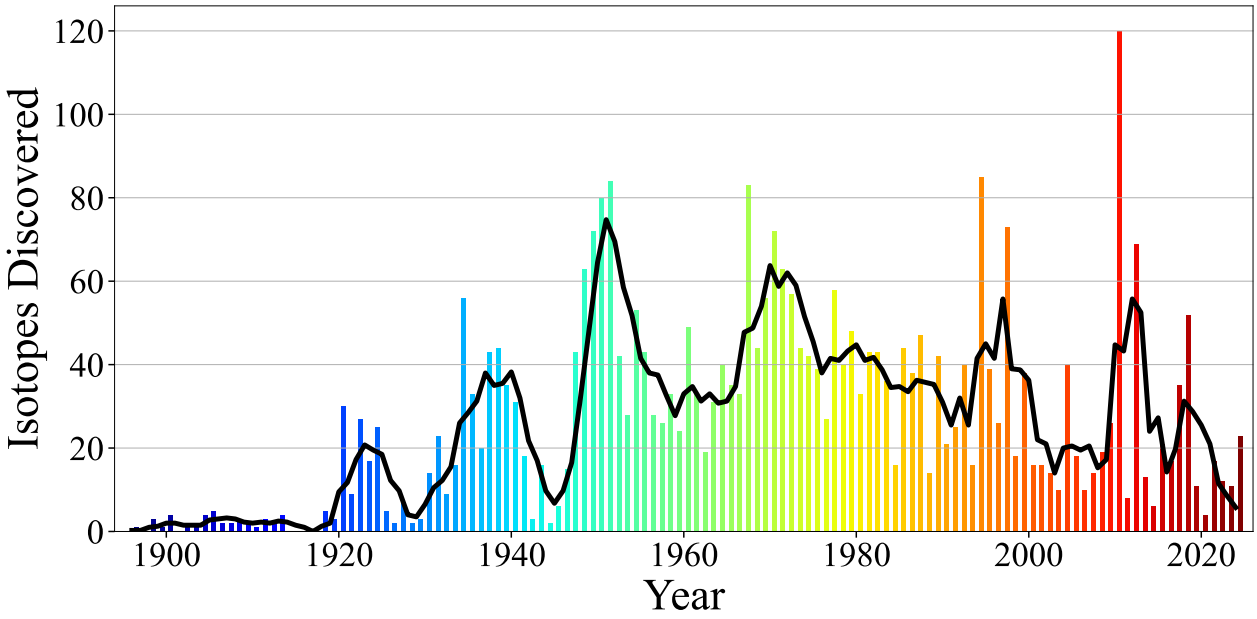

Figure 1.2: The discovery of isotopes is separated by historical breakthroughs in technology. The colors indicate the transition from one main method of discovery to the next. From left to right, the colors purple, dark blue, light blue, blue-green, green-yellow, orange, and red represent radioactivity, mass spectroscopy, the first accelerators, reactors, fusion evaporation, early projectile fragmentation plus in-flight fission, and next generation facilities, respectively.

New isotope discoveries and the exploration of the Chart of Nuclides has progressed in several waves, with each wave being the result of a new technology (see Figure 1.2). The discovery of nuclides technically began with radioactivity at the beginning of the 20th century, but the first notable wave of discoveries happened in the 1920s with the advent of mass spectroscopy. It was at this time the majority of naturally occurring nuclides were discovered, as each element was systematically studied with mass spectroscopy and their relative isotopic abundances were documented. Shortly after, the first accelerators were constructed, and it became possible to experimentally study the collision of atomic nuclei at energies high enough to induce nuclear reactions. After a short pause on discoveries during the early 1940s, consistent progress has been made toward filling in the Chart of Nuclides. Nuclear reactors became a widely studied technology in the 1950s leading to another

spike in new isotope discoveries. Fusion evaporation was the next step in history and became the main nuclear reaction mechanism for rare isotope production for the next couple decades. Most recently, projectile fragmentation and in-flight fission saw widespread use in the production of exotic nuclides, starting in the 1990s.

Projectile fragmentation is a nuclear reaction mechanism in which a fast heavy-ion collides with a stationary target atom and fragments into lighter nuclei. This reaction is commonly viewed in a two step process called abrasion-ablation, and is depicted with a simple cartoon in Figure 1.3. Initially, the projectile collides with the target, losing several nucleons and becomes energetically excited. Next, the excited pre-fragment quickly emits protons and neutrons, releasing excitation energy in the process. Projectile fragmentation is fundamentally characterized by a fast heavy projectile and a light target atom. It is an advantageous means of production because the prefragment is moving at close to the initial beam velocity, and the product can exit the target to be analyzed at a later stage. This is different than slower or smaller projectiles, which create reaction products that remain in the target and require chemical separation to be extracted.

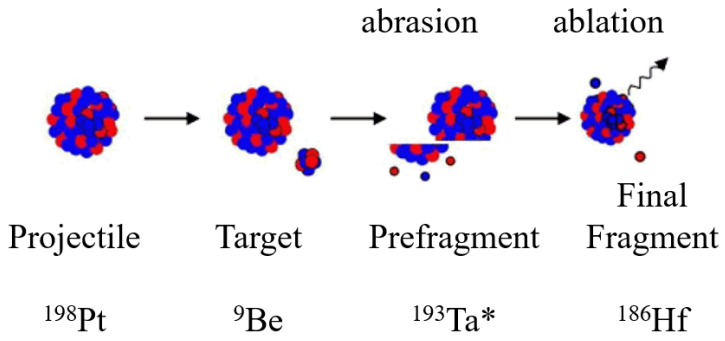

Figure 1.3: A cartoon depiction of projectile fragmentation is illustrated in the two-step abrasion-ablation process. The heavy projectile participates in a grazing collision with the target atom where a number of nucleons are quickly removed (abrasion). The pre-fragment then evaporates neutrons and protons until reaching a bound state (ablation).

The fragmentation of heavy nuclei produces an enormous variety of products that must be separated in order to study a given exotic nuclide. Figure 1.4 demonstrates the wide range of particles that can be produced in the fragmentation of a single nuclide, ^{208}Pb. This reaction will produce fragments that are only a single proton or neutron lighter than lead, as well as the lightest

nuclides. The separation and selection of a given nuclide from the vast sea of fragmentation products is performed with a fragment separator. A fragment separator uses magnetic fields to guide the collection of fragmentation products through a series of separation and selection steps [13, 14]. The detailed setup of each fragment separator used in this work is provided in Chapter 2.

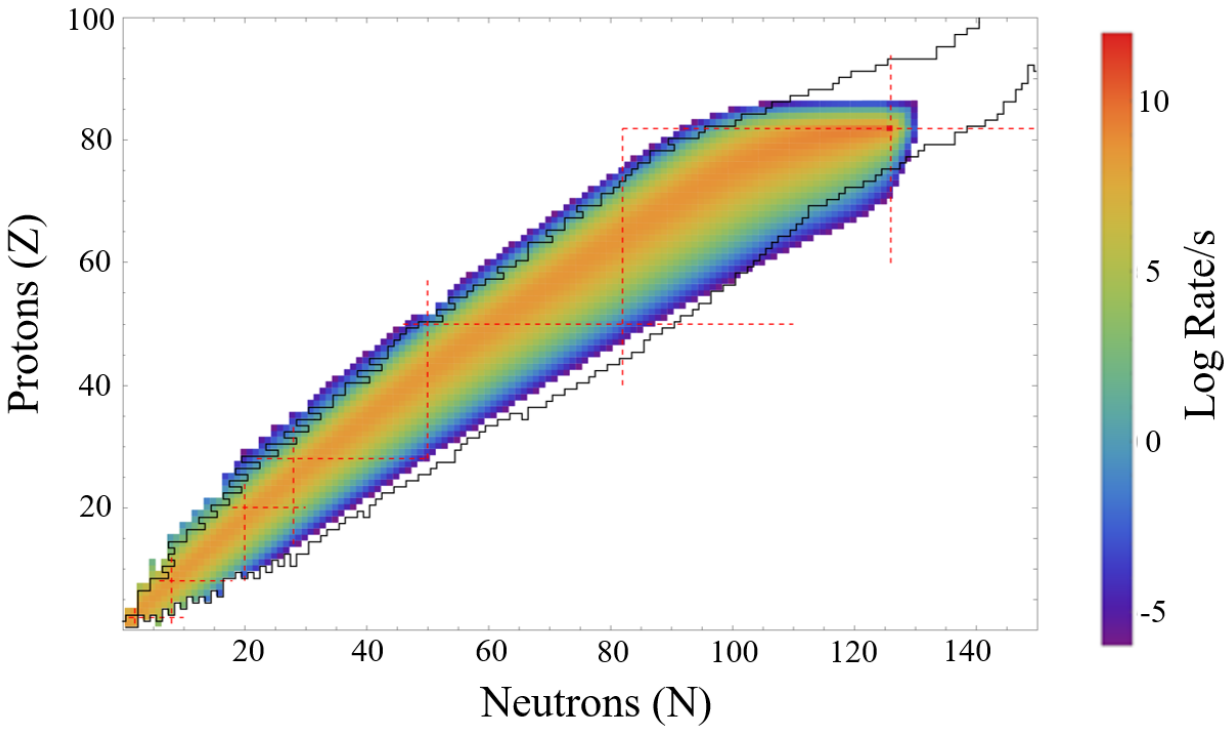

Figure 1.4: The production rate of each fragment for 400 kW of ^{208}Pb at 212 MeV/u on a carbon target is shown. The `EPAX3` parametrization was used for the cross sections [15], and the plot was generated in `LISE`$^{++}$ version 16.0.3 [16]. Projectile fragments span the majority of the chart. The rate is shown in log scale and the highest intensity rates occur down and to the left of the primary beam.

The use of fragment separators to deliver rare isotope (RI) beams from projectile fragmentation is a flexible and widespread method for creating exotic nuclides. This work presents the medium-energy fragmentation of a ^{198}Pt beam, and the separation and identification of its resulting products. Motivation for the production of neutron-rich rare isotopes near $N = 126$ is described in the following section, and a summary of previous work carried out in this region is given in Section 1.3.

1.2 Motivation

Research in the production of neutron-rich rare-isotopes near $N = 126$ is motivated by the importance of these isotopes to nuclear astrophysics and nuclear structure studies. Many nuclear science facilities around the world are focused on this region [17]. Given the importance of nuclei in this region, it becomes equally important to explore how to make these nuclides. This exploration will ultimately lead to filling in uncharted nuclear territory on the Chart of Nuclides and thereby answering important questions about the universe, such as the origin of heavy elements [3]. Despite the interest, producing these isotopes has been difficult. Today, the neutron-rich region near $N = 126$ is relatively unexplored compared to other neutron-rich areas of the Chart of Nuclides, leaving plenty of room for discovery. As the region is uncovered, each new isotope can be used for nuclear physics studies and may also lead to applications outside the field of nuclear physics. An important goal is to reach the isotopes that play a fundamental role in understanding the origin of heavy elements, such as platinum and uranium [3]. New isotope discoveries not only make a wide variety of nuclear experiments possible, but they also hold the potential for new applications in material science, medicine, and industry. For example, precise measurements of isotopic mass and charge radii help refine our models of atomic structure and contribute to the standards used in precision instruments [18, 19]. The half-life of an isotope is also useful, as it informs us about its stability and potential uses in radiometric dating or medical diagnostics [20].

A vast number of unique nuclei are naturally created by nucleosynthesis, the cosmic formation of nuclei more complex than a free proton or neutron, which mostly occurs in stellar environments [22]. However, due to the fact that the half-lives for most nuclei are short on the time scale of the Earth [8], a small subset of nuclei are naturally available for nuclear astrophysics and nuclear structure studies. Therefore, studies involving how to make rare isotopes in laboratory conditions become necessary. The astrophysical phenomenon of nucleosynthesis occurs in a variety of cosmological conditions, such as in the core of the sun, in supernovae explosions, and in neutron star merger processes [22]. While nucleosynthesis processes such as the pp-chain and CNO cycle have explained the origin of

lighter elements in our universe [22], it is still not well understood how heavier elements are formed. Several notable candidates have been proposed such as the rp-process (rapid proton capture), the s-process (slow neutron capture), and the r-process (rapid neutron capture). The general pathways of these three processes through the Chart of Nuclides are shown in Figure 1.5. The rp-process is characterized by a rapid capture of protons and then a β-decay back to stability [22]. This process occurs in supernovae and x-ray bursts, and it is capable of producing nuclei up to the masses of Sn isotopes [21]. The s-process is a relatively slow nucleosynthesis process that climbs along the valley of stability in the Chart of Nuclides (see Figure 1.5), and it is predicted to occur mostly in asymptotic giant branch stars [22]. While the s-process is capable of producing stable nuclei up to ^{208}Pb, it cannot reproduce the peak in natural isotopic abundances near mass number $A \approx 195$ [3]. The r-process is the missing puzzle piece that completes the picture of nucleosynthesis, offering an explanation for the $A \approx 195$ mass peak and the origin of super-heavy elements, such as uranium [22].

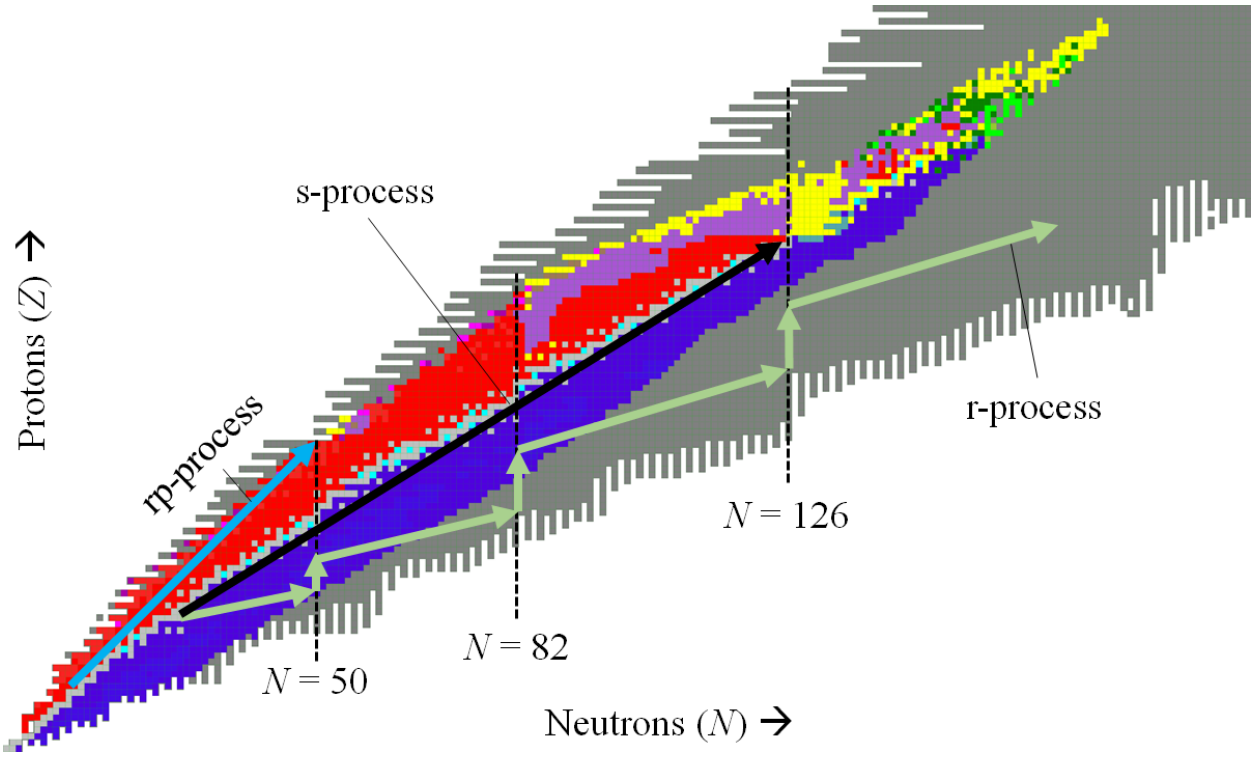

Figure 1.5: The Chart of Nuclides organized by nucleosynthesis processes [21]. The same color scheme for decay is used as in Figure 1.1. The rp-process, s-process, and r-process are represented by the blue, black, and green arrow, respectively.

Neutron-rich nuclei near $N = 126$ contain vital astrophysical information that can help develop our understanding of the r-process. The r-process is theorized to occur at incredibly high neutron densities, conditions which are present in neutron star mergers and supernova explosions [22]. In these conditions, it is possible for a series of rapid neutron captures to out-compete the relatively long beta-decay half-lives near stability [22]. Consequently, the r-process pathway is predicted to lie considerably far away from stability, as shown in Figure 1.5. The pathway also passes directly through the neutron-rich region near $N = 126$ and is theorized to "hit a wall" at the $N = 126$ shell closure. This "wall" in the r-process pathway is directly tied to the isotopic abundance peak at $A \approx 195$, and it can be studied by producing new isotopes in this region. Once produced, the neutron separation energies and beta-decay half-lives of these rare isotopes can be measured and used to develop our understanding of the r-process.

The neutron-rich region south of lead has not been well studied because of the difficulty in making these isotopes. For example, only 10 neutron rich isotopes have been discovered beyond the heaviest stable platinum isotope ($Z = 78$), whereas 25 neutron rich isotopes have been discovered beyond the heaviest stable rhodium isotope ($Z = 45$) [9]. There are many approaches to creating rare isotopes through nuclear reactions, and various reaction models can be categorized into low and high energy mechanisms. Fusion-fission and multi-nucleon transfer (MNT) are low energy reaction models, which occur at energies near the Coulomb barrier of the two participating nuclei [23, 24]. On the other hand, projectile fragmentation and in-flight fission occur at higher energies, such as hundreds of MeV/u [17]. It is necessary to experimentally test these reaction models to develop a more complete understanding of how to produce rare isotopes in this region. The main contributing factors to the relative difficulty of producing isotopes by fragmentation in this region are the presence of multiple charge states in heavy ions and the exponentially decreasing cross sections of successive proton removal from neutron-rich nuclei [25]. However, the 400 kW upgrade at FRIB [26] will allow researchers to explore reactions that occur at very small cross sections and lead to the discovery and production of many rare isotopes.

1.3 Prior Work

The production of neutron-rich rare isotopes has been recently dominated by projectile fragmentation and in-flight fission. In the past four decades, over 80% of new isotope discoveries in the neutron-rich region between $104 \leq N \leq 131$ have been created by fragmentation or fission (see Figure 1.6). However, the discovery of new isotopes with fragmentation has slowed down as exponentially shrinking cross sections have prevented further progress. In an attempt to explore a new pathway, there has been a great deal of focus placed on lower energy reactions just above the Coulomb barrier. Recently, one of the low energy reaction models with the most attention is MNT. Despite the fact that renewed interest in MNT began over a decade ago, there have been no direct measurements of new neutron-rich isotopes produced by MNT since 2010 [27] (limited to the scope of Figure 1.6). Fusion-fission also deserves recognition as a viable production mechanism for new isotopes in this region of interest [23]. Both projectile fragmentation and MNT will be covered in this section, and key work will be highlighted.

Before the widespread use of projectile fragmentation at the turn of the century, the majority of new isotopes were being discovered by fusion-evaporation reactions. These are inherently low energy collisions that aim to fuse the participating nuclei rather than break them apart. These reactions required the use of on-line isotope separator devices to extract the products made in the target. Limiting the scope to neutron-rich isotopes between $104 \leq N \leq 131$, these low energy heavy-ion collisions were responsible for almost every new isotope discovery in the 1980's [9] (see Fig. 1.6). The only exception was the discovery of ^{207}Hg by irradiating lead and bismuth targets with neutrons [9]. Low energy heavy-ion collisions were often carried out at low beam energies near the Coulomb barrier of the two participant nuclei. Several examples include beams of ^{136}Xe, ^{186}W, and ^{238}U, all under 15 MeV/u, irradiated on tungsten-tantalum sandwich targets [28].

Eventually it was realized that the vast collection of fragments created in the collision of relativistic heavy-ions could be utilized with a fragment separator. A couple examples of early fragment separators include the A1200 at NSCL, RIPS at RIKEN, and LISE3 at GANIL [14, 29, 30].

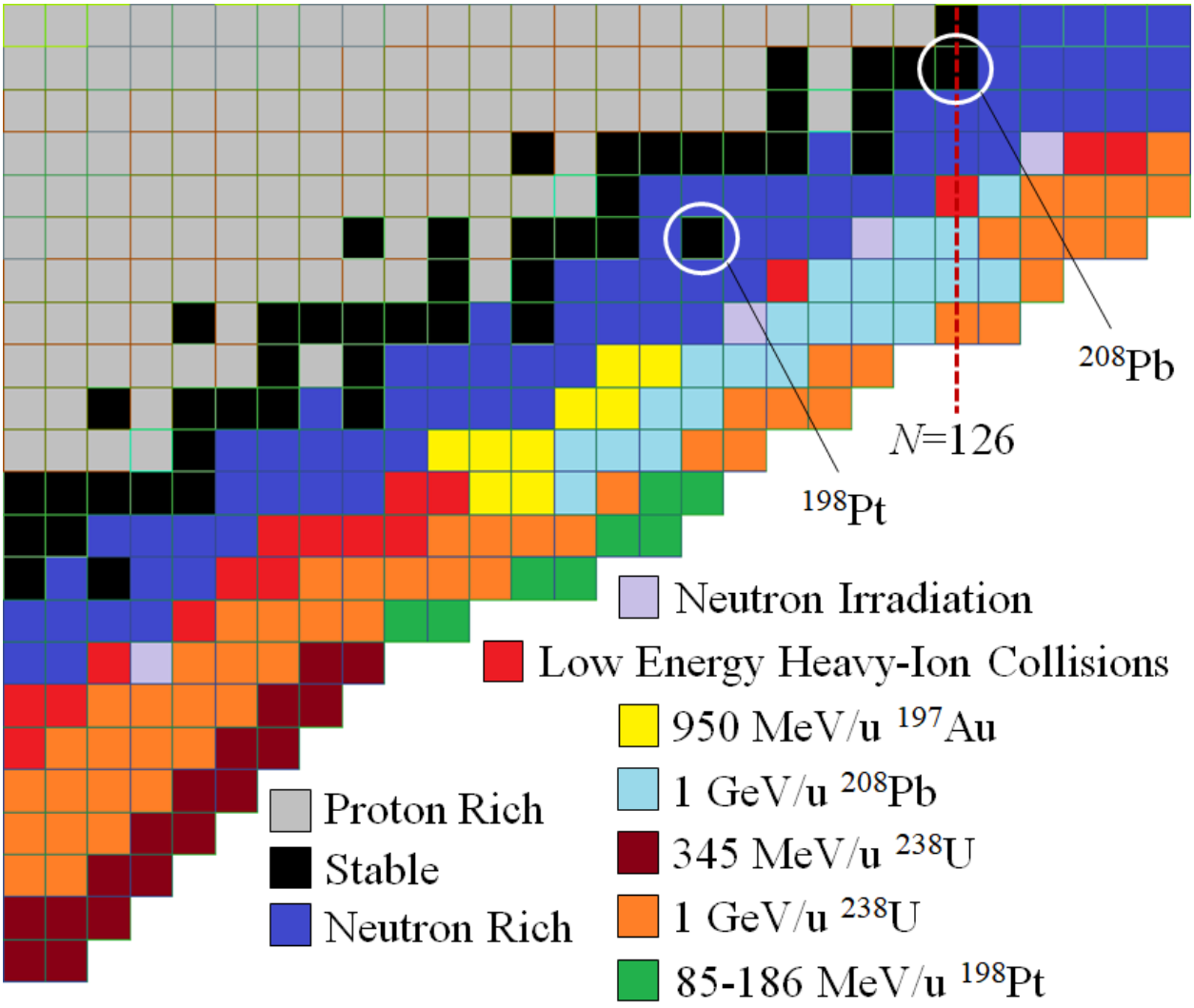

Figure 1.6: The neutron-rich region between $104 \leq N \leq 131$, organized by production methods that led to the first discovery of a given nuclide. Elements between promethium and bismuth are shown ($61 \leq Z \leq 83$). The proton-rich side of the chart has been grayed out, the stable isotopes are shown in black, and neutron-rich isotopes discovered before 1980 are shown in blue. All low energy experiments are shown in red, neutron beam experiments are shown in light purple, and every other listed experiment was carried out using projectile fragmentation or in-flight fission.

These devices were able to capitalize on the relatively small emittance of the fragmentation products, which had similar momentum distributions to the primary beam. Production of new isotopes in the neutron-rich region near $N = 126$ with fragmentation began at GSI with a ^{238}U primary beam at 1 GeV/u [31]. This experiment focused on reactions involving the removal of over 40 nucleons, a relatively energetic process compared to previous low energy heavy-ion experiments. The fragmentation of ^{197}Au was also carried out at GSI [32]. However, this time the focus was

on fragments much closer to the primary beam, and the newly discovered isotopes were the result of removing only a few nucleons from the projectile. Therefore, while the projectile was still at a relatively high energy, the reactions that produced the fragments of interests were hypothesized to come from low excitation energies of the projectile residual. In contrast to the uranium beam, it was observed that the experimental data from the gold beam did not agree with EPAX, an experimental parametrization of cross section data [33]. This led to the development of an analytical code named Cold Fragmentation (COFRA) [32]. COFRA was based on a simplified version of the abrasion-ablation model, only considering the 1n decay channel in the de-excitation step. COFRA was able to reproduce the experimental cross sections for fragments created by the removal of a few nucleons relatively well.

Next generation facilities continued to push the limits of fragmentation, leading to the discovery of many new isotopes. Upgrades such as the coupling of cyclotrons at the NSCL [34], and incremental upgrades to the RIBF accelerator at RIKEN [35] led to the increase of beam intensity by multiple orders of magnitude. With massively increased beam intensity, a landslide of new discoveries were made across the Chart of Nuclides [36, 37, 38, 39, 40]. While the aforementioned ^{238}U fragmentation experiment was carried out in 1998 at GSI, with a primary beam intensity of 5e6 pps [31], the results of an experiment with 8e8 pps of ^{238}U was published in 2012 [5]. For perspective, FRIB recently produced a 177 MeV/u ^{238}U beam with a rate of roughly 1.5e12 pps [41]. The 2012 GSI experiment led to the discovery of 60 isotopes, the majority of which are shown in Figure 1.6. It was reported that fragmentation plays the dominant role in creating elements above $Z = 72$ whereas fission becomes the dominant reaction below $Z = 69$. The fragmentation of 1 GeV/u ^{208}Pb also led to the discovery of over 20 new neutron-rich isotopes near $N = 126$ [42, 43, 44, 45]. Cross sections were measured and compared to an updated experimental parametrization (EPAX3 [15]), COFRA, and a Monte Carlo abrasion-ablation code called ABRABLA07 [46]. Both ^{238}U and ^{208}Pb fragmentation studies concluded that EPAX3 underpredicts cross sections in this region, and that COFRA and ABRABLA07 reproduce experimental data relatively well [5, 47]. In-flight fission experiments performed at RIKEN using a 345 MeV/u ^{238}U beam led to the discovery

of 29 new isotopes, shown in Figure 1.6. Within the scope of neutron-rich isotopes between $104 \leq N \leq 131$, 99 new isotopes were produced from projectile fragmentation or in-flight fission experiments since the turn of the century.

In the same two decades, only one new neutron-rich nuclide between $104 \leq N \leq 131$ was discovered by MNT in 2010 [27]. Several explorations into the viability of MNT were also carried out. The main motivation for the renewal of interest in MNT compared to fragmentation was the difference in cross section. Fragmentation had shown to exhibit exponentially shrinking cross sections upon subsequent proton removal [47], whereas theoretical predictions for the cross sections of MNT reactions remained considerably higher [48]. Initially, mass spectra of fragments produced in the <7.5 MeV/u ^{136}Xe + ^{208}Pb reaction was deduced and found to be even higher than the previous theoretical predictions [49]. Later, the reactions of 5 MeV/u ^{64}Ni + ^{207,208}Pb were also explored and found to have higher production cross sections than fragmentation for the most exotic fragments [50]. However, due to the relatively thin target and lack of a contribution from multi-step reactions, the production rates for MNT were below fragmentation. Another study of ^{136}Xe + ^{208}Pb was performed, this time at 3.3 MeV/u, and the identity of the products were determined from γ-ray spectra of well known isomers [51]. These results were two orders of magnitude lower than the theoretical predictions for cross sections of $N = 126$ isotones. The ^{136}Xe + ^{198}Pt reaction at 8 MeV/u was also executed, and the production cross section for a target-like fragment resembling ^{200}W, a new $N = 126$ isotone, was extracted from the cross sections of projectile-like fragments [52].

Turning to the past five years, the interest in MNT reactions has continued to gain momentum. Several large scale projects have begun to focus on making neutron-rich isotopes near $N = 126$, such as the N=126 Factory at ANL [53] and the NEXT project [54]. The NEXT project will use a large solenoid that encloses the production target so that the wide angular distribution of products can be captured and focused into a beam. Fusion-fission reactions also exhibit large angular distributions and could benefit from the NEXT project [23]. Some of the latest experimental results for MNT include the ^{238}U + ^{198}Pt reaction at 10.75 MeV/u, which led to the discovery of

^{241}U [55]. Additionally the 5.60 MeV/u ^{204}Hg + ^{208}Pb reaction was carried out, and it was reported that experimental cross sections were multiple orders of magnitude greater than leading MNT models [56], such as the di-nunclear system model (DNS), which originally came from JINR [57].

During that time, the fragmentation of a ^{198}Pt beam led to the most recent discovery of new isotopes in this region (see Fig. 1.6) and is the focus of this thesis. Eight new isotopes were discovered using medium energy projectile fragmentation of the neutron-rich ^{198}Pt isotope. First, the experimental configuration for both the fragmentation of 85 MeV/u ^{198}Pt at NSCL and the fragmentation of 186 MeV/u ^{198}Pt at FRIB will be presented. Next, the methodology behind the particle identification of projectile fragments and the measurement of their production cross sections will be described. A systematic procedure for dealing with asymmetric error will also be provided. In addition, a novel charge state analysis will be explained, which was especially developed to correct large systematic errors in cross section measurements due to ion charge states. The results will then be presented in three main sections: (i) the discovery of new isotopes, (ii) cross section measurements, and (iii) the evidence of residual electrons on the projectile fragment. Each section will be discussed in depth in the discussion chapter, where possible uses for the new isotopes are suggested along with a comparison of cross section results to several models. The final section of the discussion will provide a detailed motivation for the development of a new methodology to calculate charge state fractions of heavy ions. Finally, the conclusion will be presented with a summary of this work, an outlook on the next steps that should be taken, and a long term perspective of fragmentation's role in the production of rare isotopes.

Chapter 2

Experimental Configuration

Two separate platinum beam fragmentation experiments were performed, one at the NSCL and one at FRIB. Compared to the NSCL experiment, the FRIB experiment was performed with over double the primary beam energy and an increase in power of over two orders of magnitude. This advancement in acceleration capability allowed for the use of a considerably thicker production target to facilitate an increase in the production rate of rare isotopes. This chapter will first provide details of configuration for the NSCL experiment and then for the FRIB experiment. The experimental setups for the NSCL and FRIB experiments are presented here in a form closely following their descriptions in the 2023 Physical Review C publication [25] and the 2024 Physical Review Letters publication [58], respectively.

2.1 Fragmentation at NSCL

A $^{198}Pt^{61+}$ beam was accelerated by the Coupled Cyclotron Facility (CCF) at the National Superconducting Cyclotron Laboratory (NSCL) at Michigan State University to an energy of 85 MeV/u and an intensity of 0.3 pnA. The corresponding beam power was 5.05 W. A combination of the A1900 fragment separator [59] and the S800 analysis beam-line [60] was used to separate and identify rare isotopes produced from fragmentation of the ^{198}Pt beam. Both nickel and beryllium targets of varying thickness were utilized at the target position of the A1900.

The experimental setup is shown in Figure 2.1. This two-stage separation system was similar to a previous NSCL experiment with a ^{82}Se beam [39], which allowed for a high degree of rejection of unwanted reaction products. However, in this work the S800 beam-line optics were modified to

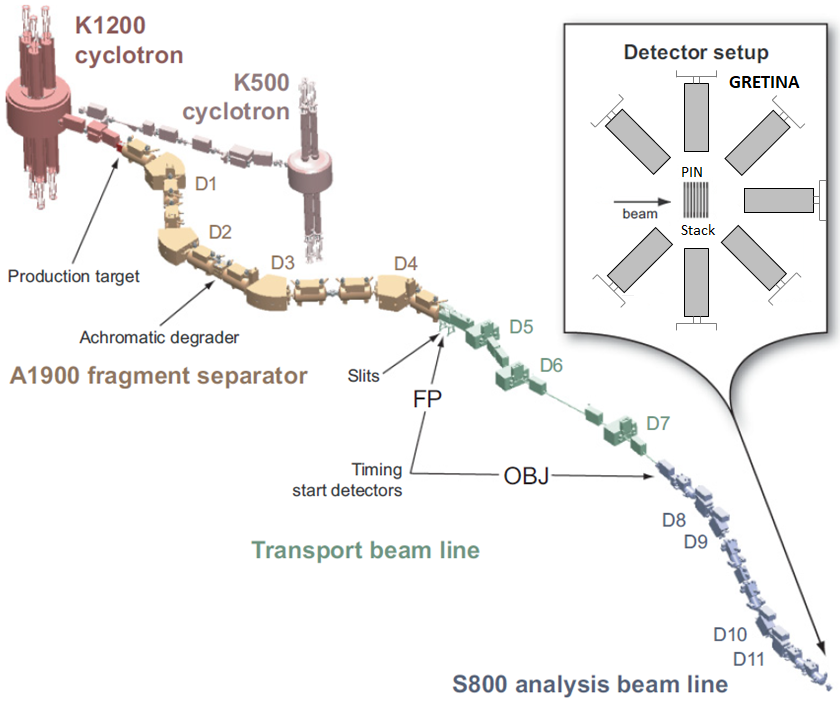

Figure 2.1: Sketch of the experimental setup used in the ^{198}Pt fragmentation experiment performed at NSCL, as presented in Haak et al. [25]. A ^{198}Pt beam was produced by the NSCL coupled cyclotrons and fragmented on a production target at the start of the A1900 fragment separator. Fragments were transported to the target location of the S800 spectrometer and stopped in a silicon telescope surrounded by GRETINA [61]. Image 1 (I1) of the A1900 was located between D2 and D3. I1 contained momentum selection slits and an achromatic degrader (wedge). Image 2 (I2) was located at the focal plane of the A1900, labeled “FP", and it contained another set of slits and a timing scintillator.

produce a 50 mm/% dispersion at the target location of the S800 spectrometer. This modification made it possible to measure momentum without making additional position measurements in the beam-line, thereby better preserving initial charge state distributions of fragments exiting the production target. Depending on the presence of an achromatic energy degrader (wedge), momentum selection slits were present at both Image 1 (I1) and Image 2 (I2) of the A1900 (Figure 2.1). The magnetic rigidity of the system was adjusted depending on the fragment of interest, but varied between a minimum of 3.2063 Tm and a maximum of 3.5420 Tm. A 22.7 mg/cm^2 Kapton wedge was used to increase purity for certain data sets. A summary of experimental runs and further details can be found in Table 2.1.

At the end of the S800 analysis beam-line, the particles of interest were stopped in a PIN

Table 2.1: Experimental Settings.

Data set	Fragment of interest	Magnetic rigidity, $B\rho(Tm)$ D_1D_2	D_3D_4	$D_5D_6D_7$	Target mg/cm^2	Stripper mg/cm^2	Wedge mg/cm^2	$\Delta p/p$ (%)	Time *hours*	Beam particles	Part
D2	^{197}Ir	3.5150	3.5150	3.4390	Be 23	-	-	0.2	5.9	4.93e12	Isomer tagging
D3a	^{186}Hf	3.5127	3.5127	3.4425	Be 23	-	-	0.1	0.4	7.57e11	
D3b	^{186}Hf	3.5127	3.5127	3.4425	Be 23	-	-	0.9	6.3	4.36e11	
D4a	^{186}Hf	3.4928	3.4928	3.4204	Ni 17	Be 9	-	0.2	3.2	7.18e13	Isomer study
D4b	^{186}Hf	3.4928	3.3912	3.3147	Ni 17	Be 9	22.7	0.8	15.4	1.58e14	
D5	^{186}Hf	3.3948	3.2875	3.2063	Be 47	-	22.7	0.7	18.6	2.07e14	
D6a	^{189}Hf	3.4440	3.4440	3.3638	Be 47	-	-	0.5	22.8	1.72e14	Production
D6b	^{189}Hf	3.5420	3.5420	3.3680	Ni 17	Be 9	-	0.9	14.4	2.68e14	of new
D7a	^{192}Hf	3.4910	3.4910	3.4141	Be 47	-	-	0.7	21.9	6.23e14	isotopes
D7b	^{192}Hf	3.4910	3.4910	3.4141	Be 47	-	-	0.9	13.8	3.00e14	

diode telescope consisting of five stacked silicon detectors (50×50 mm^2), with thicknesses of 140 μm, 140 μm, 500 μm, 1000 μm, and 1000 μm, respectively [62]. The third silicon detector in the stack was a segmented silicon strip detector (SSSD). A timing scintillator (150 μm) was placed at the focal plane (FP) of the A1900 fragment separator, as shown in Figure 2.1. The signals produced in the silicon stack were used to measure energy loss (ΔE) and total kinetic energy (*TKE*). The SSSD was also used to measure position in the dispersive plane and therefore reconstruct an event-by-event momentum to be used for particle identification (PID). The HPGe detector array, GRETINA [61], surrounded the telescope at the end of the S800 analysis beam line, and it was used to measure gamma rays for high confidence PID via isomer tagging. The delayed timing signal from the scintillator was used as the stop signal for the time of flight (*ToF*). The timing signal from the first pin in the silicon stack was used as the event trigger and *ToF* start signal.

A concern to be addressed in experiments at intermediate or low energies is the multiple charge states of ions exiting the production target. In inverse-kinematics experiments, various methods are employed to prevent primary beam charge states from reaching the detectors. One approach involves inclining the primary beam on the target, as demonstrated in the case of a ^{238}U beam at 24 MeV/u on light targets at GANIL using the LISE3 fragment separator [23]. Alternatively, thick targets can be utilized to shift the primary beam charge states to a lower magnetic rigidity relative

to the fragments of interest. This method has been demonstrated by the BigRIPS separator group in RIKEN experiments [63, 64] with a ^{238}U beam at 345 MeV/u. However, with a ^{198}Pt beam at 85 MeV/u using the A1900 separator, neither of these methods could be applied, necessitating the use of a thin target to select fragments at rigidities between the primary beam charge states. Each time a target was replaced, the charge state distribution of the primary beam was mapped out by varying the magnetic rigidity ($B\rho$) of the first two dipoles of the fragment separator (D_1, D_2). Therefore, the central $B\rho$ could be set to a value between charge states of the primary beam.

This experiment was comprised of three parts, as listed in Table 2.1. The three objectives were: (i) isomer tagging for PID, (ii) conducting an isomer study, and (iii) the production of new isotopes. For the majority of the data sets, the only material present after the target was a scintillator at I2 of the A1900, with the exception of D4b and D5 (see Table 2.1), which contained a wedge at I1 (Figure 2.1). Three separate target configurations were used: thin beryllium (23 mg/cm^2), thick beryllium (47 mg/cm^2), and a nickel target (17 mg/cm^2) with a beryllium stripper (9 mg/cm^2). For new isotope production, the separator was tuned on more exotic hafnium fragments, namely ^{189}Hf and ^{192}Hf. The wedge was not used at these settings due to the already low rate of exotic fragments. It was a priority to maintain a high momentum acceptance while striking a balance between increasing the statistics of reaction products and minimizing detector damage caused by the edge of the primary beam.

2.2 Fragmentation at FRIB

A beam of ^{198}Pt nuclei was accelerated to 186 MeV/u with the FRIB linear accelerator [26, 65], and then directed onto a 3.54 mm thick carbon target rotating at 500 rpm with a density of 1.89 g/cm^3. All of the data collection in this experiment was performed with the Advanced Rare Isotope Separator (ARIS)[66, 67]. The accelerator delivered three charge states to the ARIS target (^{198}Pt$^{66+,67+,68+}$) enhancing beam intensity by over double compared to using a single charge state [68]. A different beam dump strategy was utilized at FRIB compared to the previous ^{198}Pt fragmentation at NSCL.

A thicker target was used, resulting in a considerable difference in energy loss of the primary beam compared to the fragments. This target thickness accounted for 70% of the primary beam's range, shifting the unreacted primary-beam ions to a low-$B\rho$ region, which could be separated without a significant loss in the fragments of interest.

In this work, the ARIS ion optics, typically set for momentum compression [66], were adapted to a non-compression dispersive mode to facilitate the production of a wider array of neutron-rich isotopes. A 50 μm Al-degrader was placed strategically in the dispersive plane of the preseparator to block lighter particles using acceptance slits at the DB1 position. The setup is detailed in Figure 2.2. The C-Bend section of ARIS, from DB1 to DB5, operated as a high-resolution analysis stage with a horizontal dispersion of 67.4 mm/% at DB3, effectively separating high-Z particles.

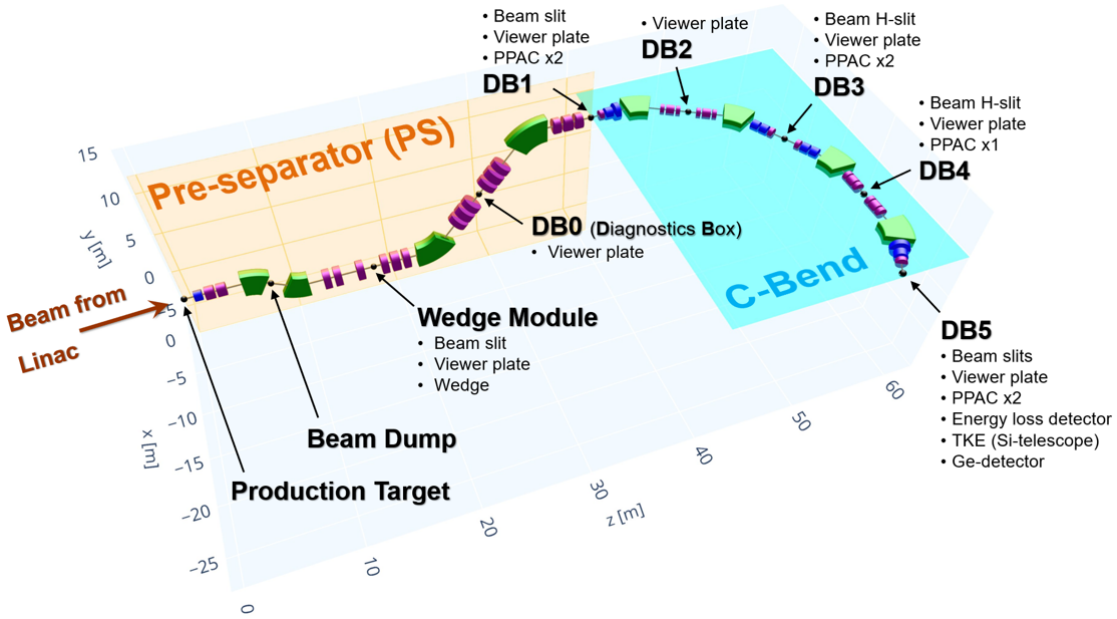

Figure 2.2: Sketch of the experimental setup used in fragmentation experiment performed at FRIB as presented in Tarasov et al. [58]. A ^{198}Pt beam was produced by the FRIB linear accelerator and fragmented on a production target at the start of the pre-separator. Fragments were transported to the fifth diagnostic box (DB5) where they were stopped in silicon to measure *TKE* and *ToF*.

The secondary cocktail beam was stopped at the DB5 station in a silicon PIN diode telescope comprised of six detectors, each measuring 50x50 mm^2, with thicknesses 505, 307, 496, and 998 μm for the final three detectors [69]. These thicknesses were chosen to stop the fragments of interest in the 4th silicon detector, and the remaining detectors were used to veto reactions

that happened in previous detectors. Trajectory details were deduced from measurements taken at the DB1, DB3, and DB5 focal points using delay-line position-sensitive parallel plate avalanche counters (PPACs). The positioning of these instruments is shown schematically in Figure 2.2. A germanium γ-ray detector was placed at DB5, and aided in PID by detecting the isomeric decay of ^{188}Ta [70], described in the following chapter.

Optimization of the separator to enhance the production of the $^{190}_{72}\mathrm{Hf}^{70+}$ ion was based on predictions from the $\texttt{LISE}^{++}_{cute}$ software [6]. The identification of each fragment was performed by analyzing $B\rho$, ToF, ΔE, and TKE. The detailed methodology will be provided in the following chapter.

Chapter 3

Data Analysis

An event-by-event identification of charged particles passing through the separator and the calculation of production cross sections for each species of nuclide was performed in this work. This chapter will begin with a discussion of each method and then continue with a description of the treatment used to propagate asymmetric error. Finally, a novel Monte Carlo analysis of charge state fractions will be explained in detail.

3.1 Particle Identification

Particle Identification (PID) was performed with the ΔE-*TKE*-*ToF*-$B\rho$ method [38] through a series of three steps:

1. Initial detector calibration using primary beam,
2. Final detector calibration using several fragments of interest,
3. Calibration verification with isomer tagging.

In the first step, a very low rate of primary beam was delivered to the experimental setup where every detector was triggered. The program LISE^{++} [16] was used to predict energy loss (ΔE), time of flight *(ToF)*, and dispersive position of the primary beam and calibrate each detector. These calibrated measurements were then utilized in the following expressions to calculate nucleon number (A), proton number (Z), and electric charge (q) of the primary beam.

$$Z \propto \sqrt{\frac{\Delta E}{\beta^2}\left[\ln\frac{5930\beta^2}{1-\beta^2}\right]^{-1}}, \tag{3.1}$$

$$\frac{A}{q} = \frac{B\rho}{\beta\gamma}\frac{e}{uc}, \tag{3.2}$$

$$q = \frac{TKE}{u(\gamma - 1)(A/q)}, \tag{3.3}$$

Equation 3.1 is a simplified version of the Bethe-Bloche formula and the numerical value is calculated from the mean excitation energy of a silicon medium [71]. All other quantities are defined as follows:

ΔE: Energy loss in material,
β: Relativistic velocity,
γ: Lorentz factor,
$B\rho$: Magnetic rigidity,
e: Electron charge,
u: Atomic mass unit.

After the initial application of Equations 3.1, 3.2, and 3.3, the centroids of each particle group on the PID spectra did not line up on the integer axes of Z, A, or q. To fix this discrepancy, the calculated value of each PID variable was linearly calibrated to be equal to the know value of that variable. This linear calibration was particularly useful for Z because the simplified Bethe-Bloche in Eq. 3.1 is only a proportionality. The original Bethe-Bloche formula involves many constants, but, in this PID code, the constants were replaced by a slope and an intercept.

After the initial calibration, the secondary cocktail beam was delivered to the experimental setup and the PID was confirmed via isomeric tagging of the well known ^{188}Ta and ^{190}W isomers (Figure 3.1) [70, 72]. The same isomers were used in both experiments. To perform isomer tagging, the gamma rays were first detected with either GRETINA at the target position of the S800 spectrograph, in the case of the NSCL experiment, or a smaller HPGe detector located at DB5, in the case of the FRIB experiment. The gamma ray spectra recorded with these devices were then gated on peaks whose energy corresponded to a known isomeric decay. These gates were placed on PID plots to confirm the location of the known isomer (Figure 3.2). In this way, the PID was able to be confirmed with high confidence.

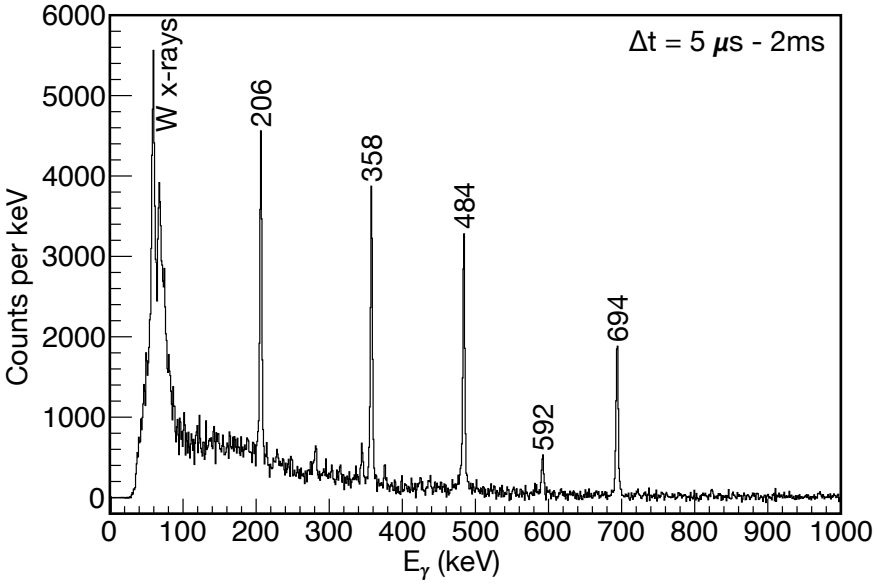

Figure 3.1: A γ-ray spectrum of events in GRETINA recorded up to 800 μs after events identified as ^{190}W, modified from Haak et al. [25]. This data was recorded during the Be target settings of the NSCL experiment (see Table 2.1). The energies of the observed peaks correspond to gamma transitions from the 166 μs isomeric state of ^{190}W [72], confirming particle identification.

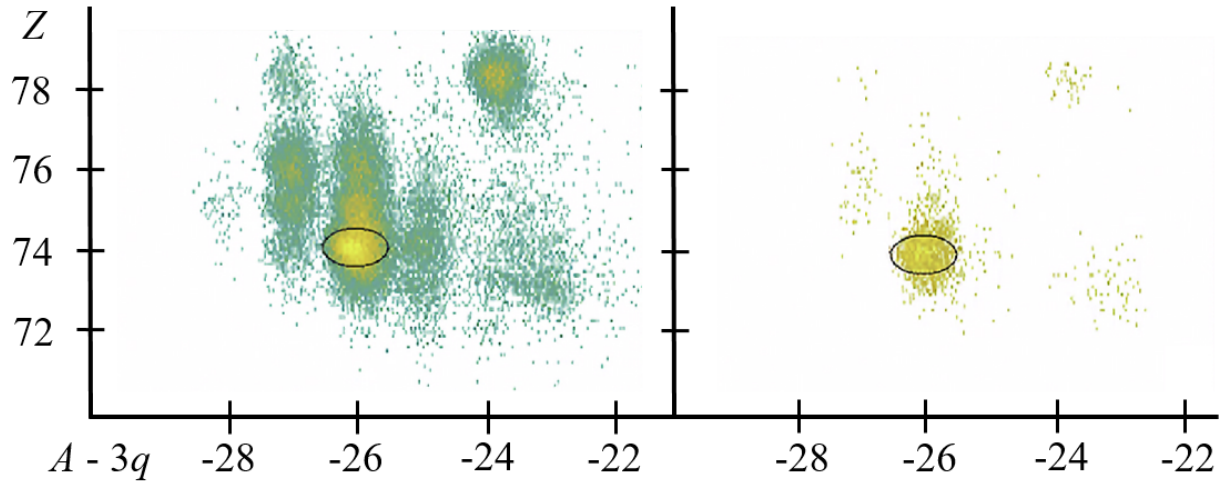

Figure 3.2: PID spectra of charge state $Z - q = 2$ gated on specific gamma ray energies from Figure 3.1. The plot on the left hand side shows the PID after placing a single gamma gate from the 484 keV peak. The plot on the right hand side shows the PID after placing an AND-gate of both the 484 keV and 694 keV peak. The remaining counts are located at position $Z = 74$ and $A - 3q = -26$, or $A = 190$, confirming the identity of $^{190}W^{72+}$.

The final detector calibration was performed by collecting raw channel data of each detector for several particle groups in the confirmed PID and incorporating those measurements into a

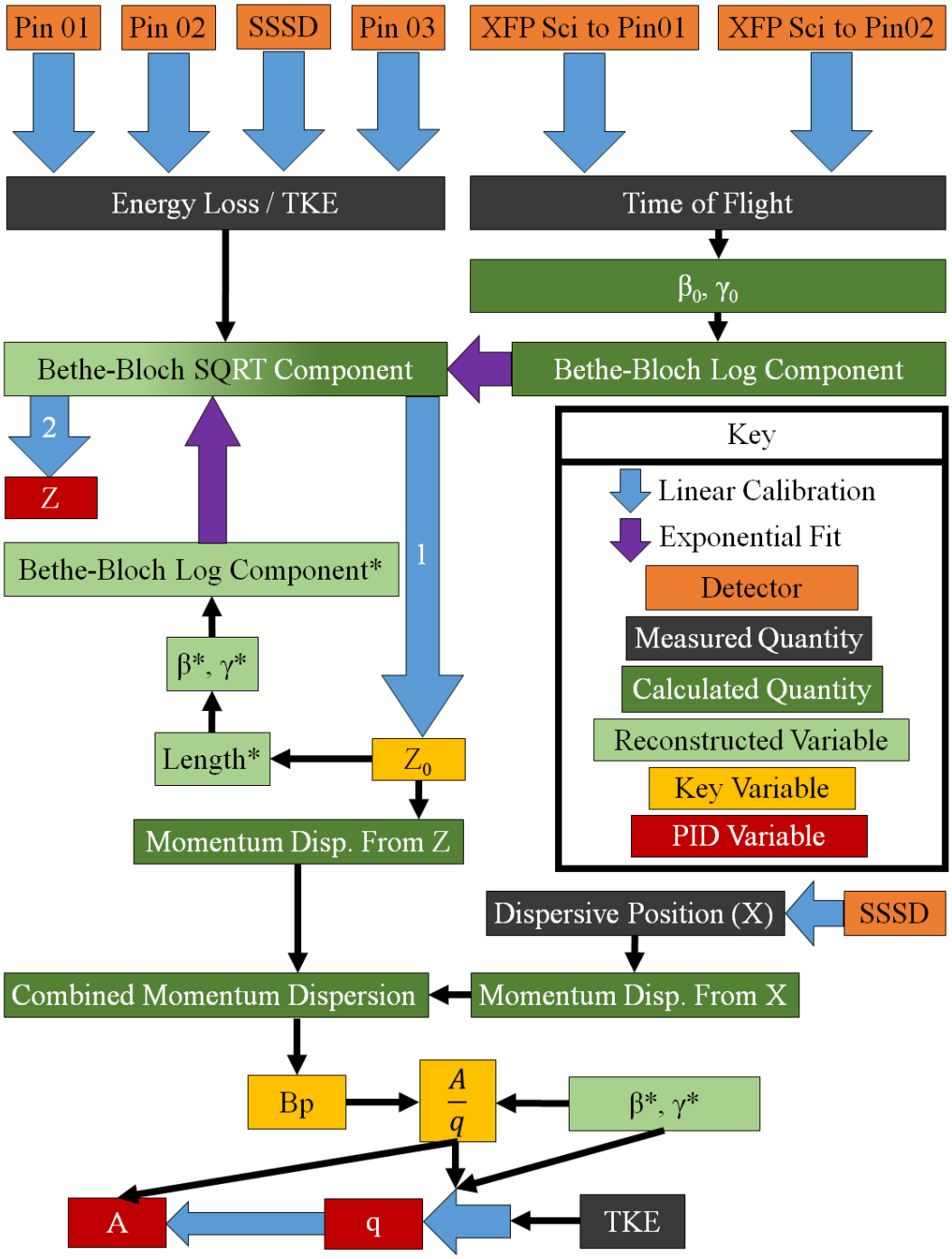

Figure 3.3: Calculation procedure for PID calibration. Detectors are as defined from Section 2.1. A key is included to explain the color scheme. The *Bethe-Bloch Log Component* is the natural log term from Eq. 3.1 and the *Bethe-Bloch SQRT Component* is the entire square root term from Eq. 3.1. Z_0 is the initial calculation of the proton number (Z) before momentum dispersion corrections. "Momentum Dispersion From Z" is related to the dispersive position dependence on Z, and it was only present in data sets with a wedge setting.

large scale optimization process. This process was essentially a multi-dimensional linear fit that minimized global error [O. Tarasov, Private Communications]. The global error was defined as the difference in the calibrated value of each measurement and the predicted value in LISE^{++} [73, 16]. The optimization for the NSCL data included a linear fit for each ΔE measurement (four total), each ToF measurement (two total), and a final linear fit for each PID variable, A, Z, and q. The ΔE measurement used to calculate Z was not entirely in the linear region of the Bragg curve, and, therefore an exponential fit was also applied to Z, specifically to the logarithmic component of the Bethe-Bloche formula. A detailed flow chart of this procedure can be seen in Figure 3.3.

The FRIB PID followed a similar procedure as the NSCL PID. The main difference was the use of multiple PPACs, rather than a single SSSD, to reconstruct the trajectories of particles passing through the fragment separator. This resulted in more accurate calculations of momentum dispersion and $B\rho$. The resulting PID spectra from each experiment, demonstrating charge separation, can be found in Section 4.1.

3.2 Cross Section Calculation

The cross section for production of a given rare isotope is determined from the number of observed ions of that isotope compared to the expected number for a given reaction. Cross sections were only calculated for data collected in the NSCL experiment. During the FRIB experiment, the transmission through the pre-separator was determined to be considerably lower than what was planned, and it was concluded that the error on those calculations would be too large to provide meaningful results. The production cross section for individual fragments was calculated using the following expressions:

$$\sigma = \frac{N_f}{N_b\, N_t\, T} \times 10^{27}\ [mb], \tag{3.4}$$

$$N_t = \frac{t A_v}{\rho_t}. \tag{3.5}$$

Where N_f is the number of a given fragment detected at the end of the fragment separator (or yield), N_b is the number of total incoming beam particles, T is the fraction of all ions produced at the target and transmitted through the separator, and N_t is the number of target atoms per unit area. The number of beam particles, N_b, is the integrated beam current divided by the charge state and the charge of a proton. The value of N_b was determined from integrating beam current over the course of the run. The current was determined from scaler values that are linearly correlated to the beam current. N_t was derived via Equation 3.5, where t is target thickness, A_v is Avogadro's number, and ρ_t is the density of the target material. The fraction of transmitted fragments, T, depends on several factors including the momentum and angular distribution of fragments produced in the reaction, the momentum and angular acceptance of the beams lines, and the charge states populated in the reaction. At the time of this analyis, T was calculated using versions 16 and 17 of $\texttt{LISE}^{++}_{cute}$ [16, 6].

The yield of each fragmentation product was obtained by the integration of all counts present in a given particle group. To avoid undercounting, PID spectra were fit with integer-spaced fixed-width Gaussian functions. The integer spacing was due to the integer nature of charge and nucleon

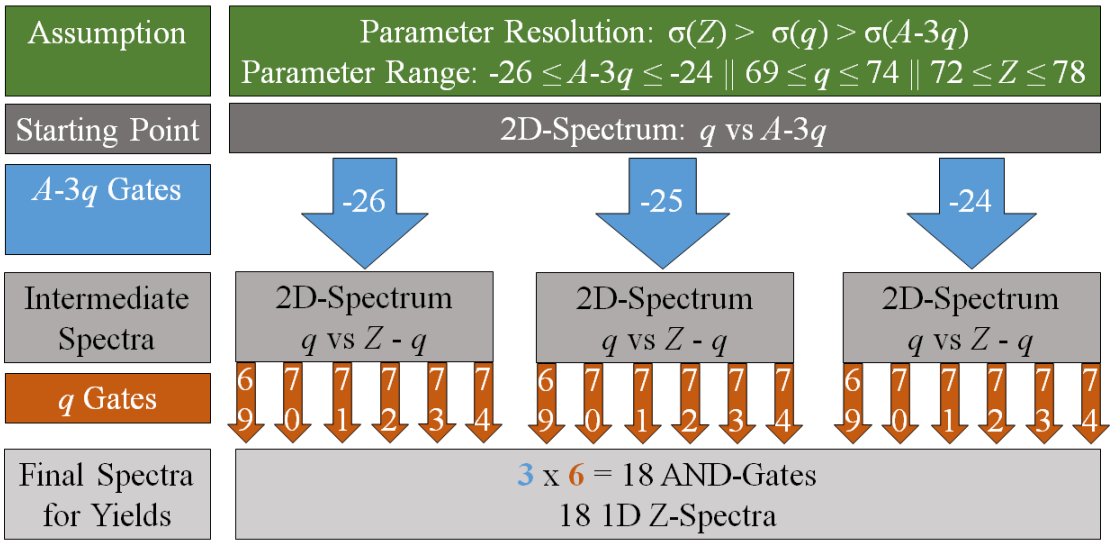

Figure 3.4: Procedure for counting isotopes in one-dimensional spectra while minimizing losses in event gates. The assumptions for parameter resolution and range are given in green. Spectra are shown in varying shades of grey, primary gates are shown in blue, and secondary gates are shown in orange. The convolution of three primary gates with six secondary gates leads to a total of 18 AND-gates. This example is visualized in Figure 3.5.

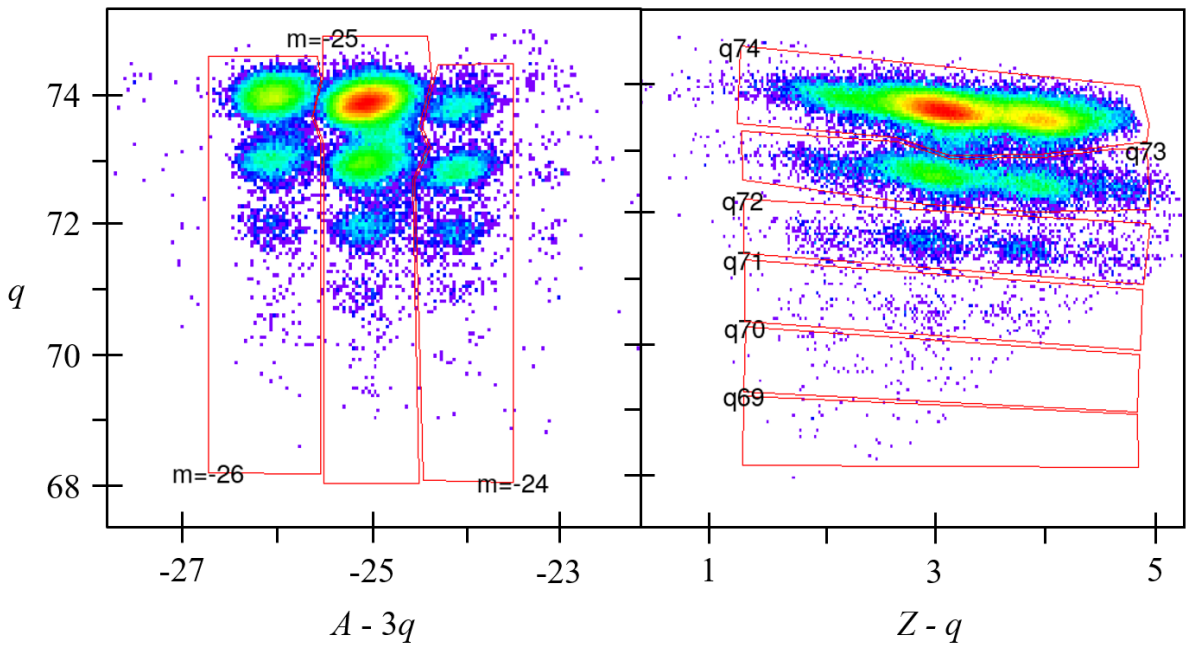

Figure 3.5: A visual example of the gating procedure from Figure 3.4. The data shown is from the D4a data set (see Table 2.1). The q vs mass ($A - 3q$) spectrum is shown with three mass gates on the left, and q vs charge state ($Z - q$) spectrum is shown with six charge gates on the right.

number. The fixed width was assigned due to the assumption that experimental resolution was consistent across all isotopes.

The integration of integer-spaced fixed-width Gaussian functions was performed on one-dimensional spectra (Figure 3.6). Due to the fact that three parameters are required to uniquely identify ions (Z, q, and A or $A - 3q$), the reduction of PID spectra to a single dimension required two series of gates. The first series of gates were drawn about integer values of the best resolution parameter, which varied between data sets. This series of gates was then applied to two-dimensional spectra of the remaining two parameters. The second series of gates was drawn within these two-dimensional spectra around integer values of the second best resolution parameter. The first two series of gates were then combined into a third series of AND-gates and applied to one dimensional spectra of the lowest resolution parameter. This process is depicted in Figure 3.4 and 3.5, and guarantees the lowest resolution parameter was “saved for last". Therefore, the integration of the fixed-width integer-spaced Gaussian peaks accounted for the most possible overlap of particle group distributions. A visualization of overlapping edges of Gaussian peaks can be seen in Figure 3.6.

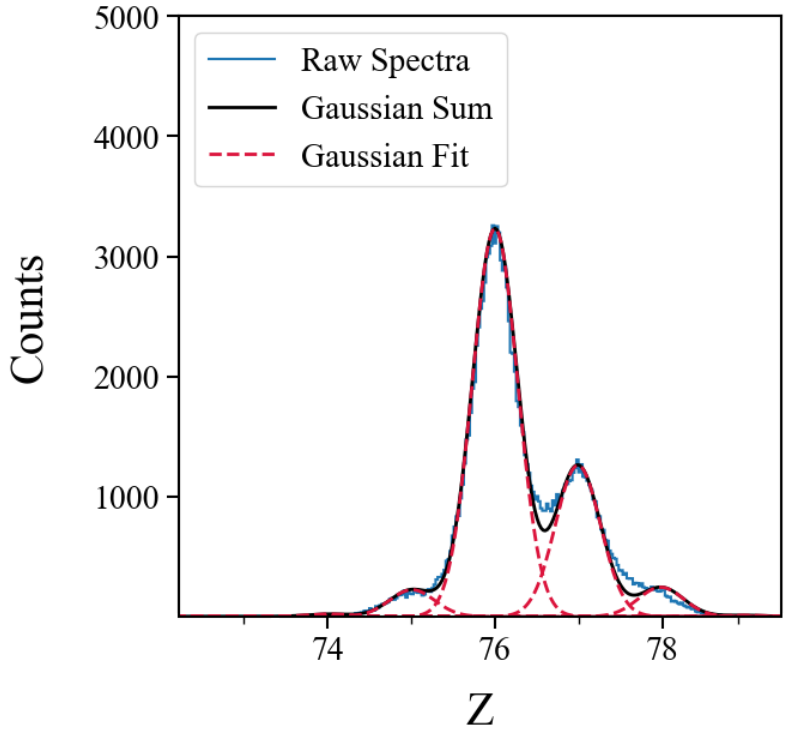

Figure 3.6: One dimensional fixed-width integer-spaced Gaussian peaks fitted to experimental data from Figure 3.5. Raw Spectra (blue) is the one dimensional Z histogram of data from the $q = 73$ AND $A - 3q = 25$ gate. Gaussian Fit (red) shows each individual Gaussian function fitted to their corresponding particle group. Gaussian Sum shows the summed profile of all individual peaks added together.

The experimental yield was modified for settings that included a Ni target plus a Be stripper foil (see Table 2.1). First, cross sections were calculated for the ^{198}Pt + ^{9}Be reaction by using the target-only ^{9}Be runs. Next, the yield of fragments produced in the ^{9}Be foil was estimated using those cross sections. Finally, the predicted yields of the stripper foil were subtracted from the total experimental yields to produce a value that corresponded to production in the Ni target.

The next term calculated from Equation 3.4 was the total number of beam particles which hit the target, N_b. During this experiment we did not have a direct measurement of the beam current on target at all times. Therefore another quantity, which scales linearly with the beam current, was chosen as the live measurement which can be recorded at all times. It was necessary to perform a measurement of both the beam current on target, for example using a Faraday cup at the target position, and the beam scalar for each given configuration of experimental settings. This ensures

a proper linear calibration of beam scaler to beam current can be performed. In this experiment, the scaler counts on the scintillator at the extended focal plane of the A1900 separator was used for beam integration. Primary beam current was measured before the attenuator with a Faraday cup and after the attenuator with a non-intercepting probe. A charge to scaler ratio was calculated for

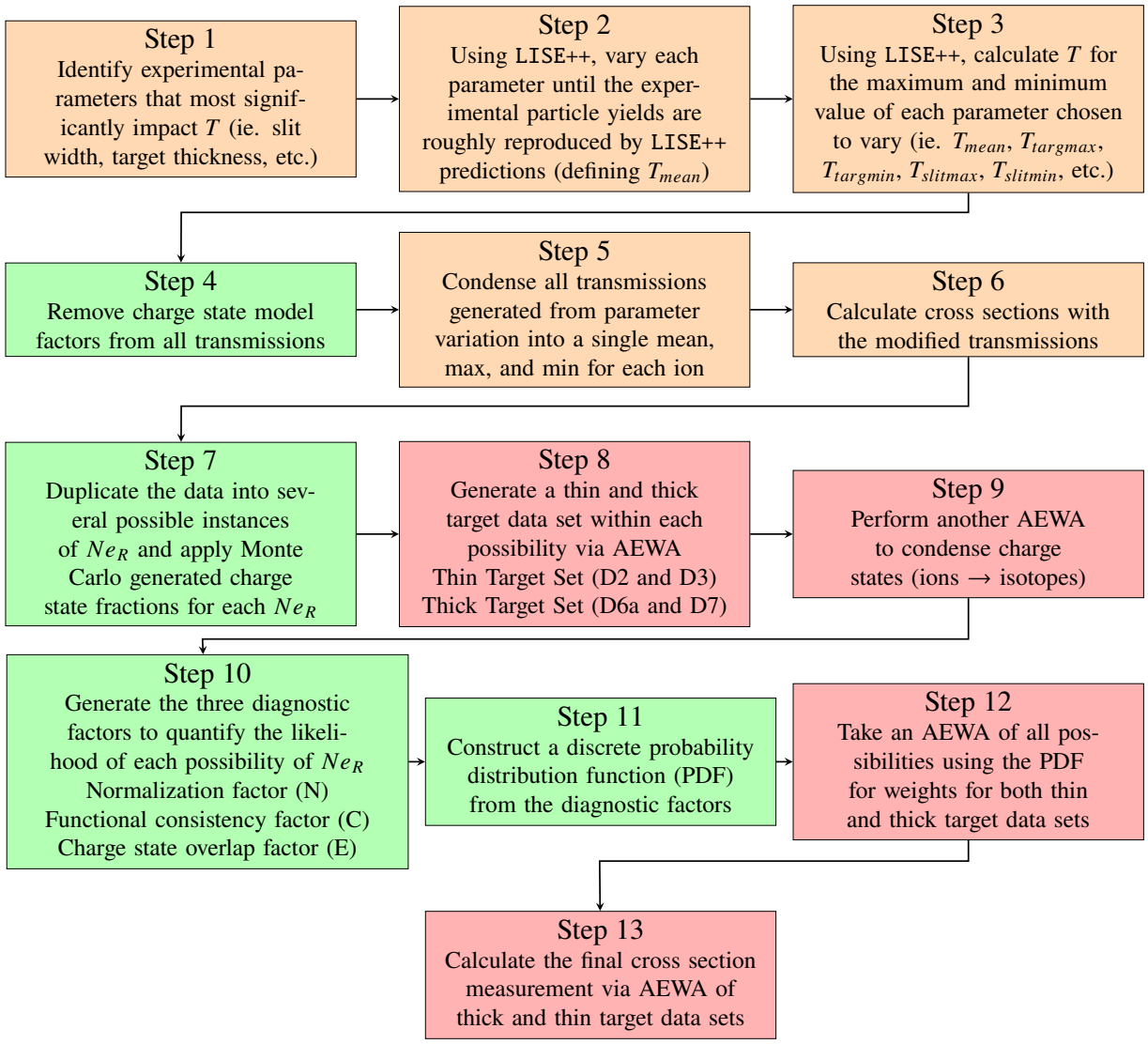

Figure 3.7: A flow chart of the cross section calculation procedure. T is the fraction of a given nuclide that transmits from the target to the end of the fragment separator. The different subscripts of T, such as targmax, is the value of T for a given experimental parameter shift. AEWA (Asymmetric Error Weighted Average) is an error weighted average that accounts for asymmetric error bars and is defined by Equation 3.8. Steps 8, 9, 12, 13 utilize the AEWA and are shown in red. Steps 4, 7, 10, 11 constitute the novel charge state analysis developed in this work and are shown in green. The remaining steps, shown in orange, describe how T was calculated and condensed from LISE^{++}.

every measurement of beam current and beam scaler rate taken during the experiment. An average of this ratio was taken for multiple measurements within a given experimental configuration and used to calculate a total integrated beam current for a given data set. This total charge was then simply divided by the individual charge of the primary beam, $^{198}Pt^{61+}$, to result in the total number of beam particles incident on the target.

The transmission value, T, is defined as the fraction of a given nuclide that transmits from the point of creation in the target to the point of detection at the end of the fragment separator. This value represents all of the particles lost at each slit, in each material, around the bend of each dipole, and through each quadrupole. It is a value that depends not only on the momentum and angular distribution of the fragments themselves, but also the momentum and angular acceptance of the beam lines. A final, yet crucial, consideration is the charge states of each nuclide. These charge state distributions are populated in the production target and change in each subsequent material down the beam line.

An accurate estimate of T, along with quantification of its error, is arguably the most complex aspect of cross section determination due to the multitude of factors which can significantly impact T. A list of cross section calculations steps involving T are depicted in Figure 3.7. These steps will be referred to by their number for the rest of the chapter. Systematic errors in the cross section are captured by the estimation of errors in T. This is a complex process that will be described in detail in the following section.

3.3 Asymmetric Error

The errors associated with exponential distributions are inherently asymmetric. If an ion distribution sits on the edge of a slit, closing the slit by a small amount could cause complete loss of transmission. Opening the slit by a small amount will increase the transmission by several orders of magnitude. Therefore, it was necessary to formulate a methodology to perform calculations with asymmetric error and accurately propagate this error to the final calculation. The procedure of the cross section

calculations performed in this work are listed in 13 steps in Figure 3.7. The majority of this procedure will be described here with the exception of steps 4, 7, 10, and 11, which are related to a novel method of charge state analysis that is described in the final section of this chapter.

Starting with step 1 (Fig. 3.7), the major sources of systematic error were identified as the energy loss model, the momentum distribution model, the charge state model, and the ion optics setting of the fragment separator. The ATIMA energy loss model [74] (Option 2 in LISE^{++}) and the Universal Parameterization momentum distribution model [75] (Option 4 in LISE^{++}) were chosen for this analysis. The uncertainty in the energy loss model was probed by variation in material thicknesses, specifically materials that come before momentum selection slits, such as the production target and wedge. The uncertainty of the momentum distribution model was explored by variation of underlying σ and *coeff* parameters [75]. The uncertainty of the charge state model was investigated by questioning certain underlying physical assumptions of the fragmentation process, and it will be discussed in detail in the next section. The uncertainty of the ion optics setting was examined by a left-right variation of the I1 slits (see Fig. 2.1). Other quantities that required adjustment from nominally quoted values during experiment, but were not varied for error estimation, were the thickness of the focal plane scintillator and the initial energy of the primary beam.

In the next step, the mean value of each target thickness was determined via a global optimization process involving energy loss of the primary beam. The energy of each primary beam charge state which reached the I2 thick scintillator (see Fig. 2.1) was experimentally calculated using its dispersive position at Image 2 and the magnetic rigidity of the separator. This experimental energy was compared to the difference of the primary beam initial energy and the predicted energy loss in each target or stripper material using LISE^{++}. The He-parameterization [76] and ATIMA, options 0 and 2 in LISE^{++}, were explored in this experiment. The parameters varied during this optimization included a position calibration at Image 2, the I2 dispersion, all material thicknesses, and primary beam energy. The most optimal global fit was achieved using the ATIMA energy loss model.

The mean value of slits and momentum distribution assumptions were selected via a manual optimization process where the yield patterns of experiment were compared to predicted yield

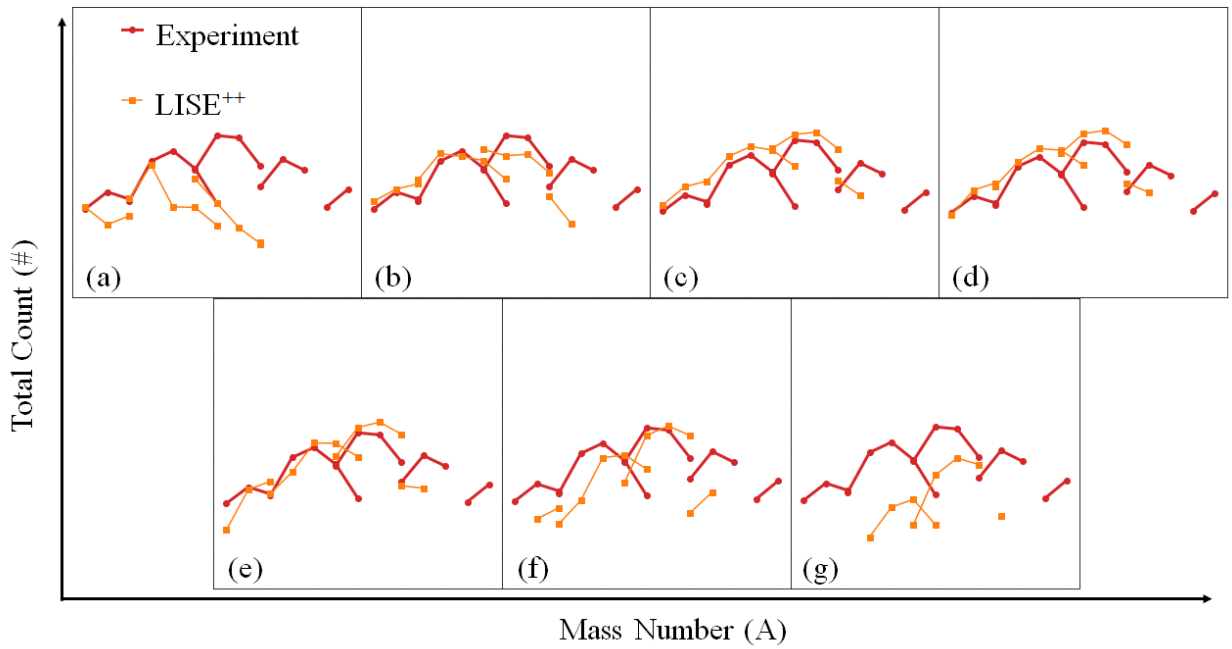

Figure 3.8: Plots of experimental yields vs LISE^{++} predictions. The comparison of these plots was used to deduce the optimal wedge thickness for data set D4b (see Table 2.1). The isotopic chain for tungsten ($Z = 74$ and $184 \leq A \leq 196$) is shown for varying wedge thicknesses. A total of five different charge states ($0 \leq Z - q \leq 4$) are shown from left to right in decreasing order of $Z - q$. Thicknesses 20.32, 21.06, 21.81, 22.55, 23.3, 24.05, and 24.8 mg/cm^2 are shown in (a) through (g), respectively. Based on this comparison an optimal wedge thickness of 22.55 mg/cm^2 was deduced.

patterns in the LISE^{++} program. An adequate comparison can be performed by normalizing the LISE^{++} beam rate in particles per second to the total number of beam particles detected for a given data set. An example of this manual optimization process is depicted in Figure 3.8. A final configuration is shown in Figure 3.9. The goal was to get the overall shape of each ion curve to match. Once that configuration is reached, the mean value for each parameter has been set. This procedure was also applied to the thicknesses of the Ni target and the Kapton wedge when analyzing the Ni target data in order to further improve upon the aforementioned global energy loss calibration.

It is important to note that exact agreement is not expected in these comparisons. This is due to the fact that the yield patterns predicted by LISE^{++} are produced with cross sections calculated from a model. Therefore, instead of looking for an exact match, we aimed to match global trends.

Once the mean value of each parameter is set, they must be systematically varied to capture

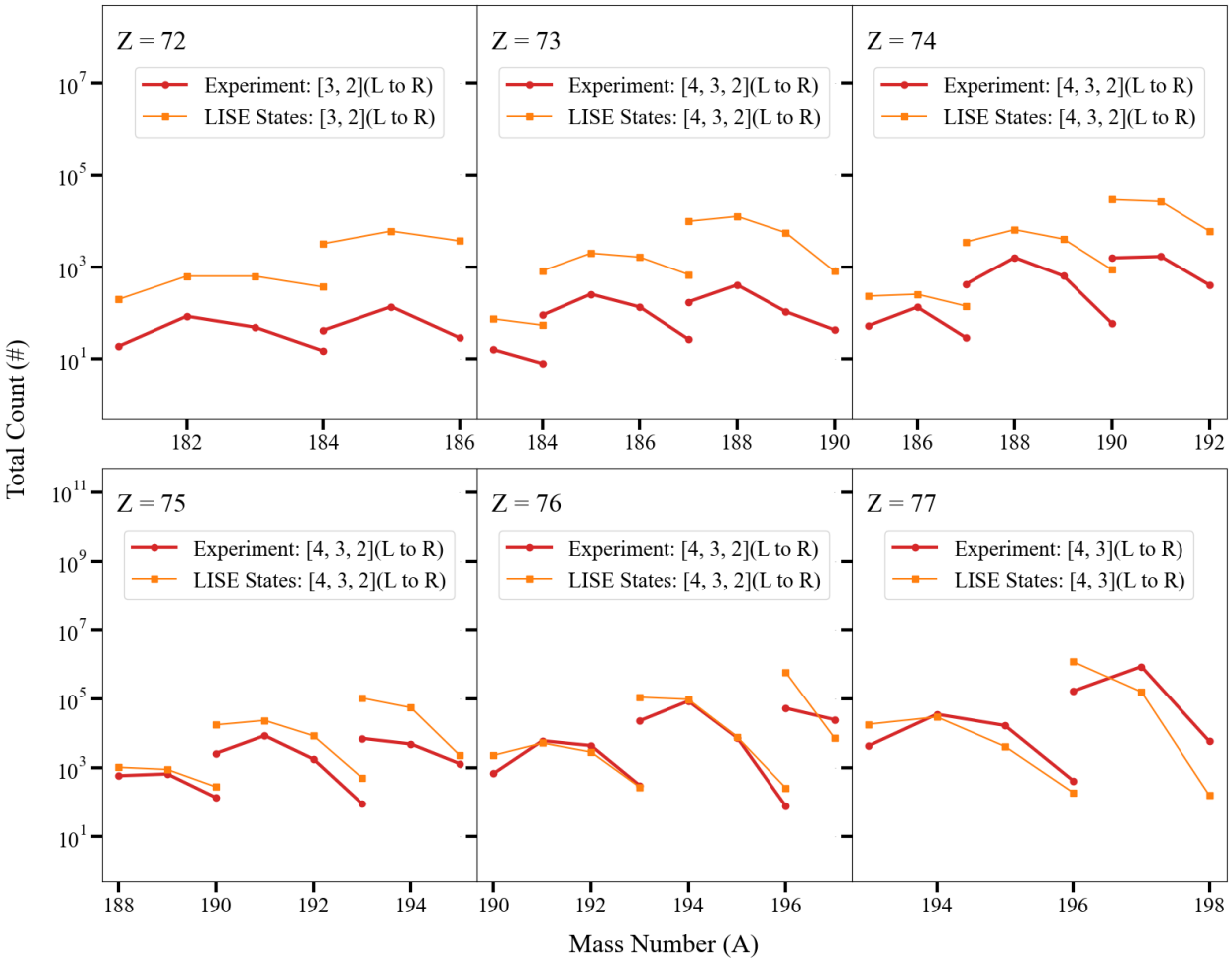

Figure 3.9: Optimized LISE^{++} parameters matching experimental results from data set D4a (see Table 2.1). Counts of each ion are on the y-axis and mass number is on the x-axis. A total of six elements, with between two and three charge states per element, are shown. The charge states present in each plot are indicated by the legend and are listed in order from left to right (L to R). The experimental data is shown in red and the LISE^{++} predictions are shown in orange.

the error in the transmission (step 3 in Figure 3.7). There is no predefined range to this variation and therefore an understanding of the underlying models is necessary to stay within physically reasonable bounds. For example, when comparing the LISE^{++} yields to the experimental yields and varying the wedge thickness parameter, one can observe a breakdown of the yield pattern as shown in Figure 3.8. It is clear that the optimal wedge thickness is somewhere in the investigated range and that the extremes on either end (±10%) are not physically possible. The acceptable range of variation was selected to be between sub figure (c) and (e), a variation of ±3%. The range of variation for each parameter selected is shown in Tables 3.1 and 3.2 for the beryllium and nickel

target data, respectively.

The pattern change due to varying the slit width parameter is slightly different than the one for material thickness. The transmission of ion distributions that sit past the edge of the slit, and only have an exponential tail within the range of acceptance, will vary wildly with a change in slit width. This contributes to our estimation of the total error. The variation of momentum distribution model parameters also results in a similar behavior of transmission values. Ion groups that sit outside the momentum acceptance of the separator in narrow momentum distribution settings may have small but significant transmissions when the momentum distributions are widened. This is a result of the exponential tails of momentum distributions.

Table 3.1: Experimental parameters that were varied to asses the uncertainty in the transmission of fragments produced during runs using a beryllium target. The most probable value for each parameter in each data set is listed. The amount varied is consistent for each data set and is shown in the final column. The target thicknesses listed here are not the physically measured values, which were reported in Table 2.1. This adjustment was made to ensure the best match between experimental transmissions and the given setup in the LISE^{++} code.

Parameter		D2	D3	D6a	D7	Variation
Beryllium Target (mg/cm^2)		21.80	21.80	50.15	50.15	±2%
Image-1 Momentum Slits (mm)		-2.2 : +2.5	-15.7 : +11.0	-7.7 : +8.0	-10.6 : +10.0	±20%
Momentum Distribution [75]	Width	125	125	125	125	+25
(Separation Energy Model 2)	Coef	0.8	0.8	0.8	0.8	+0.2, -0.3

Table 3.2: Experimental parameters that were varied to assess the uncertainty in the transmission of fragments produced during runs using a nickel target. The most probable value for each parameter in each data set is listed. The amount varied is consistent for each data set and is shown in the final column.

Parameter	D4a	D4b	Variation
Nickel Target (mg/cm^2)	17.75	17.75	±4%
Kapton Wedge (mg/cm^2)		22.5	±3%
Image-1 Momentum Slits (mm)	-2.1 : +2.1	-12.4 : +12.4	±20%
Momentum Distribution [75] Coef	1.0	1.0	±0.2

By step 5 (see Figure 3.7), each ion had roughly seven to nine possible transmission values

predicted by the parameter variation listed in Tables 3.1 and 3.2. The transmission from the optimized LISE^{++} configuration file, T_{mean}, was used for T in Equation 3.4. The positive and negative error of the transmission were defined as $\delta T_+ = T_{max} - T_{mean}$ and $\delta T_- = T_{mean} - T_{min}$, respectively. T_{max} and T_{min} are the maximum and minimum transmission values of the seven to nine possibilities predicted in parameter variation. This method ensured the most conservative approach to preserving the estimated error from the previous steps.

The propagation of the transmission error, $\delta T_\pm$, to the cross section error, $\sigma_\pm$, was performed via direct calculation as shown in Equation 3.6. Next, $\sigma_\pm$ was adjusted, using Equation 3.7, to include the uncertainty of the fragment yield, δN_f. The propagation of error from T and N_f was performed in two steps, instead of a single step with the error propagation formula, because δN_f was symmetric and $\delta T_\pm$ was asymmetric.

$$\sigma_\pm = \mp\sigma \pm \frac{N_f}{N_b N_t (T \mp \delta T_\mp)} \tag{3.6}$$

$$\sigma_\pm^* = \sigma_\pm \sqrt{\left(\frac{\delta N_f}{N_f}\frac{T}{\delta T_\mp}\right)^2 + 1} \tag{3.7}$$

To conclude that exactly 68% or 95% of the probability is encapsulated in the cross section error bars would be incorrect. However, it is acceptable to say the true value does lie within the limits selected and that the error bars are a reasonable estimation of systematic errors. In fact, this method can be considered more conservative than the standard partial derivative method of error propagation, which is not suitable for use here because there is asymmetric error. Additionally, the cross section function has a strictly positive domain which requires corrections to error analysis methods that result in negative error bars greater than the mean value. The limited sampling of the parameter space also led to an issue where T_{mean} could equal the minimum or maximum of the sample. These issues led to two corrections for the lower error bar:

(i) *if* $\sigma_-^* > \sigma$ *then* $\sigma_-^* = 0.9\sigma + 0.1\sigma_-$ [correction of non-physical case],

(ii) *if* $\sigma_-^* = 0$ *then* $\sigma_-^* = (\delta N_f / N_f)\sigma$ [correction when $T_{mean} = T_{max}$],

and one correction for the upper error bar:

(i) if $\sigma_+^* = 0$ *then* $\delta T_- = 0.1 T_{mean}$ [correction when $T_{mean} = T_{min}$].

The Asymmetric Error Weighted Average (AEWA) mentioned in steps 8, 9, 12, 13 of Figure 3.7 was performed next. Due to the exponential nature of the data, both the cross section values and their error bars were transformed to log scale before the AEWA operation. Then the mean result of the AEWA ($\bar{c}$) was calculated via a simple weighted average. The weight of each cross section (w_i) was chosen to be inversely proportional to its underlying transmission (absolute inverse log). The error bars were calculated via the following analytic function:

$$S_\pm = \sqrt{\frac{\bar{A}}{\sum_{i=1}^{n} \sigma_i^\pm} + \frac{V_\pm}{\sum_{i=1}^{n} w_i}}, \tag{3.8}$$

where $S_\pm$ is the negative and positive error of the final result, $\sigma^\pm$ is the negative and positive error for each input data point, $\bar{A}$ is a weighted error amplitude shown in Equation 3.9, and $V_\pm$ is a conditional weighted sum of variances (Eq. 3.10 and 3.11).

$$\bar{A} = \frac{1}{n\sqrt{2\pi}} \sum_{i=1}^{n} \frac{\sigma_i^\pm w_i}{(\sigma_i^- + \sigma_i^+)^2} \tag{3.9}$$

$$V_+ = 2 \sum_{i=1}^{n} \begin{cases} (\bar{c} - c_i)^2 w_i & \text{if } \bar{c} < c_i, \\ 0 & \text{otherwise} \end{cases} \tag{3.10}$$

$$V_- = 2 \sum_{i=1}^{n} \begin{cases} (\bar{c} - c_i)^2 w_i & \text{if } \bar{c} > c_i, \\ 0 & \text{otherwise} \end{cases} \tag{3.11}$$

A graphical representation in the difference between this method and the standard method when dealing with symmetric errors can be seen in Figure 3.10. The mean value of the symmetric error propagation is miscalculated and is greater than both mean values of the input data points. In comparison, the mean value of the asymmetric case lies between the two input data points which

is expected for the average of two values.

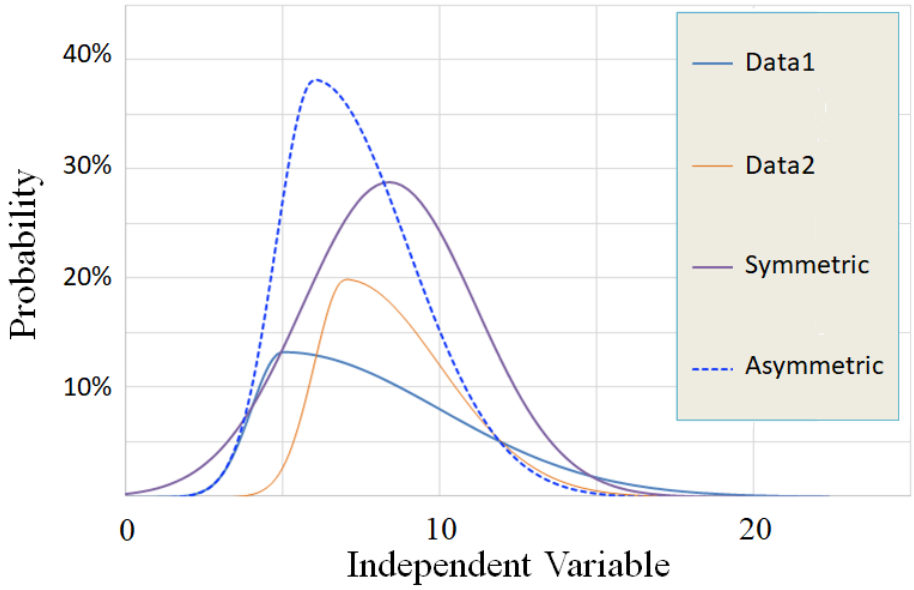

Figure 3.10: Probability distributions of two arbitrary data points with asymmetric error, Data1 and Data2. The standard symmetric average of these measurements and the specialized asymmetric average used in this work (AEWA) are shown. Data1 and Data2 are equally weighted in both averages shown here. The y-axis is probability as a fraction of unity, and the x axis is arbitrary units of the independent variable. The symmetric and asymmetric distributions have yet to be normalized.

3.4 Charge States

Ions passing through material can pickup or lose electrons. In this analysis, the final charge state was modeled by `GLOBAL` [77]. The systematic error associated with `GLOBAL` was large and motivated the creation of a novel method of analysis. The implementation is described here, while the motivation is explored in Section 5.3. The number of electrons on the projectile fragment residue, Ne_R , was selected as a physically significant quantity to consider when calculating charge state fractions from a Monte Carlo approach. This method of analysis included the removal of charge fractions from `LISE`$^{++}$ output files (step 4 of Figure 3.7), the calculation of new charge state fractions for several possibilities of the Ne_R parameter (step 7), the formulation of three optimization parameters to quantify the probabilistic likelihood of each Ne_R (step 10), and the construction of a discrete PDF

using those three parameters (step 11).

Starting with step 4, the underlying charge state fractions calculated by GLOBAL were removed from LISE^{++} transmission values. This was performed by using the result file provided by the "*Transmission A,Z,q-last*" option in LISE^{++} (extension res4). Inside this result file are two columns of interest: the "Trans, %" column and the "q_All-trans%" column. To remove the underlying charge state fractions, the former was simply divided by the latter. The transmission values were then considered 'raw', or without reduction due to charge state factors.

In step 7 of Figure 3.7, the charge-related transmission fractions were calculated for several possibilities of the Ne_R parameter. A charge state fraction was calculated for every material in the beam path using a Monte Carlo simulation in LISE^{++}. The total charge-related transmission factor for a given element was simply the product of each material's individual charge state fraction for that element. Only one nuclide of the isotopic chain was considered for each element, as the charge state fractions did not vary significantly with changing neutron number. Also, due to the small momentum acceptance of the beam lines, only ions which remained in the same charge state throughout the entire separator, from production target to implant, were considered in this analysis.

The actual execution of Monte Carlo simulations in LISE^{++} was performed as follows:

1. The LISE^{++} calculation assumed no slits for each data set (thick and thin target) so that a measure of solely charge state effects on transmission could be performed.
2. Ne_R was set via: Physics Models →Production Mechanism →Charge States →Charge state after reaction.
3. Navigated to: Calculations →Monte carlo calculation of transmission →Target.
4. Selected "One FRAGMENT of interest" and set the fragment to be an isotope of the desired element.
5. Material was selected from drop down menu of "X-coordinate."
6. The "q (ion charge)" option was selected in the "Ion parameter (M, Z, q...) box.

Two separate charge state distributions were calculated for each element: (i) ions exiting the target and (ii) ions exiting the scintillator. Figure 3.11 shows a two-dimensional Monte Carlo plot from LISE^{++} comparing these two distributions for a given isotope. It was assumed that the only ions reaching the end of the separator were those that did not undergo electron pickup or ionization

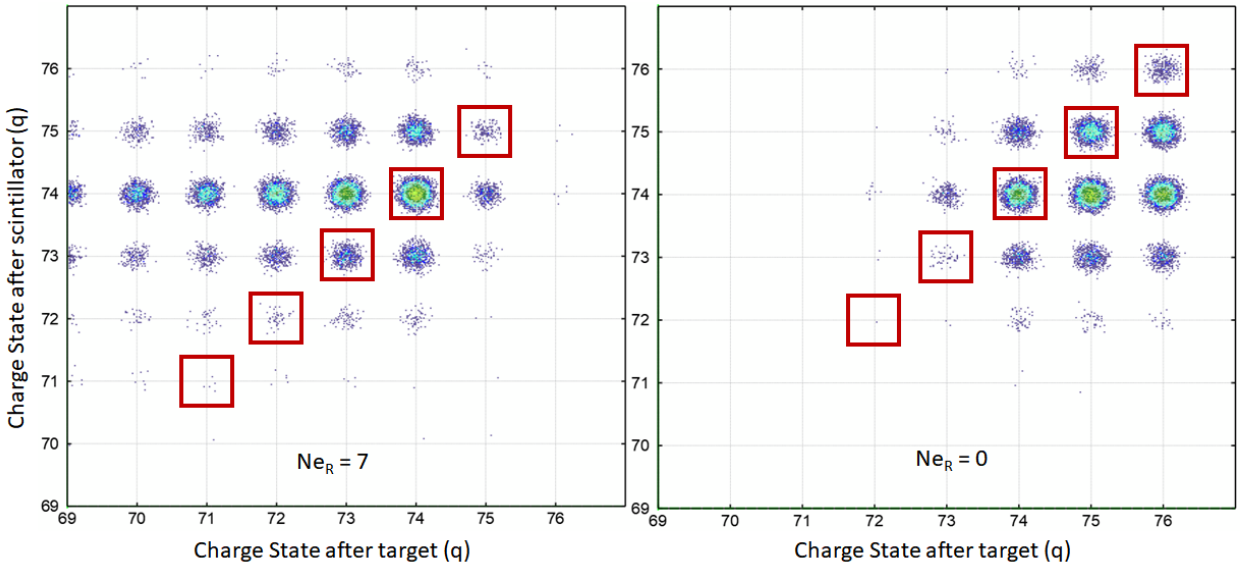

Figure 3.11: The dependence of the final charge state distribution on Ne_R is illustrated. Two-dimensional charge state distributions of ^{196}Os for $Ne_R = 7$ and $Ne_R = 0$ are on the left and right, respectively. Generated via a Monte Carlo simulation in LISE^{++}, each figure shows the charge state distribution of the isotope exiting the target on the x-axis and the charge state distribution exiting the scintillator on the y-axis. The particle groups enclosed in red boxes represent the ions which did not change charge state in the scintillator and were consequently transmitted through the S800 analysis line to the detector setup.

in the scintillator. These events are represented by the ion groups on the X=Y line of Figure 3.11 (each group is denoted by a red square contour). To calculate the charge-related transmission factor for a given ion of a given element, the number of events of for that X=Y ion group was divided by the total number of events created in the simulation. Table A.3, in the appendix, lists the charge-related transmission factors for all ions detected in the thin Be target settings (see Table 2.1).

In some cases with small transmissions, such as $T < 10^{-6}$, the Monte Carlo calculation did not produce events, even after extensive run time. This often occurred when $Z - q$ values were high and Ne_R values were low, such as $Z - q = 5$ and $Ne_R = 0$ (see Figure 3.12, on the left). To address this issue, the program ETACHA4.v3 [78, 6] was used to calculate the charge state distribution of ions exiting the scintillator. These calculations provided a relatively accurate estimate of the charge state fraction for very low transmission ions (see Figure 3.12, on the right). This charge state fraction was then used to extrapolate the Monte Carlo results, which had too few statistics, by multiplying the ETACHA fraction calculated for the scintillator by the Monte Carlo fraction calculated for the

target.

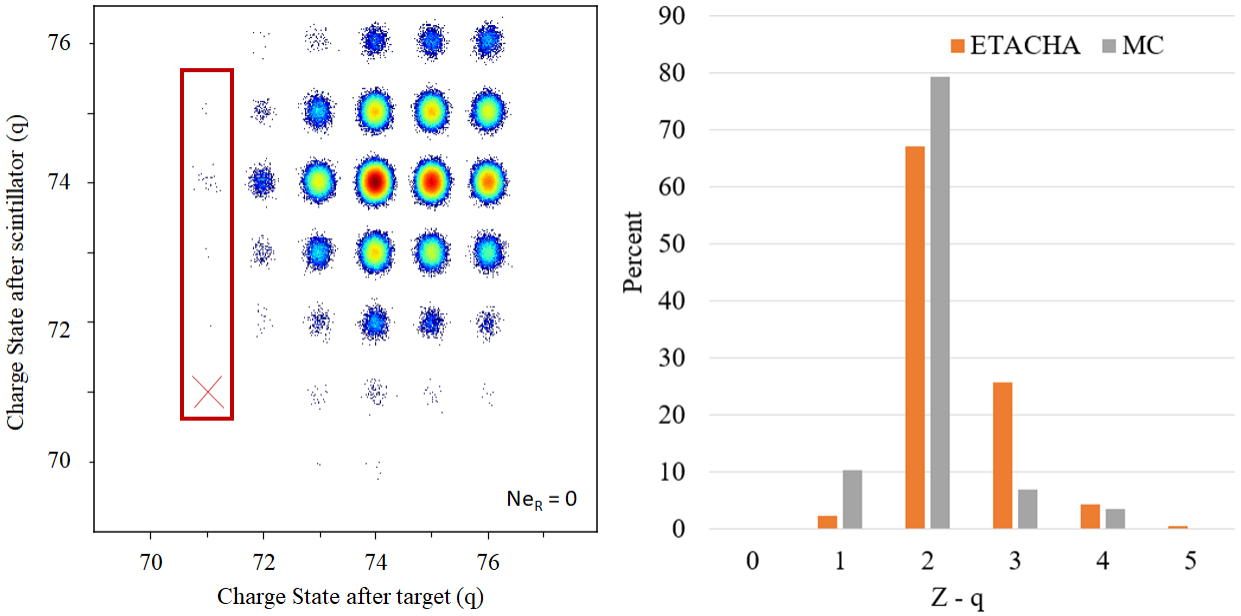

Figure 3.12: A LISE^{++} Monte Carlo calculation of ^{196}Os charge states using GLOBAL is compared with an ETACHA4.v3 calculation for a low statistic charge state. A two-dimensional Monte Carlo calculation of charge state distributions is shown on the left. The red rectangle highlights a low statistics charge state exiting the target at $Z - q = 5$. The red X indicates the absence of any events where the ion remains at $Z - q = 5$ after exiting the scintillator. The plot on the right compares the results of the Monte Carlo calculation (MC in grey) and an ETACHA calculation (in orange) of the charge state distribution of $^{196}Os^{71+}$ exiting the scintillator. The MC data shown in grey is the y-projection of the data in the red rectangle.

The bounds of Ne_R exploration were set using the following considerations. Although Ne_R values from 0 to 17 are physically possible because the primary beam was in charge state $Z-q = 17^+$, the physically probable range is much smaller due to the rapid ionization of high energy particles passing through material. Therefore, the charge-related transmission factors were sampled for three different elements within a limited range of $Ne_R = 0$ to $Ne_R = 7$. These factors changed slowly at first and then a large jump was noticed from $Ne_R = 4$ to $Ne_R = 5$, and then remained constant afterward, as depicted in Figure 3.13. This led to a focused analysis of only Ne_R values less than five.

It was then necessary to quantify the probabilistic likelihood of each Ne_R shown in Figure 3.13, as described in step 10 of Figure 3.7. During quantification, the following three factors were

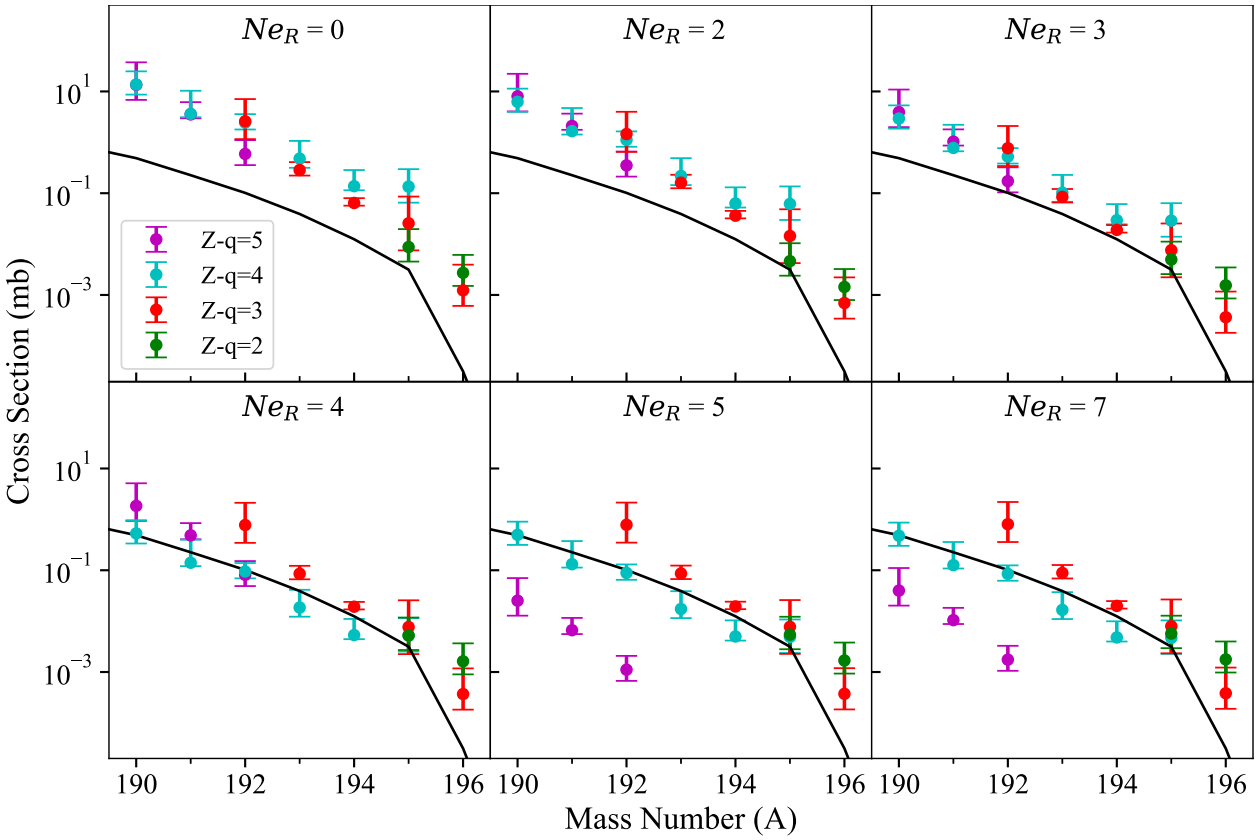

Figure 3.13: The cross sections measurement of rhenium isotopes ($Z = 75$) were calculated for $Ne_R = 0$ to $Ne_R = 7$, six of which are shown here (Be target data). Four charge states are present, $Z - q = 5$, 4, 3, and 2, and are shown in purple, cyan, red, and green, respectively. `EPAX3` is plotted as a reference (solid black line). In the instance of $Ne_R = 3$, the cross sections are consistent between ions of the same isotope and the overall magnitude is physically reasonable.

considered: (i) agreement of cross section measurements between ions of the same nuclei (E), (ii) physically possible cross section measurements (N), and (iii) the consistency of production cross sections for a given isotopic chain as a function of mass (C).

The first consideration was quantified by the average log error of each measurement and will be denoted as E. It can be seen by comparison of Figure 3.13 and 3.14 that when the underlying individual cross section measurements of different charge states do not overlap, the resulting error (E) is large (for example $Ne_R = 5$). The second consideration, denoted as N, was quantified by a normalization factor which would shift the cross section lines to a physically reasonable range. N was simply a multiplicative factor that shifted the data up or down on the cross section plot. A value of $N = 1$ corresponded to no shift and indicated the data was within a physically acceptable

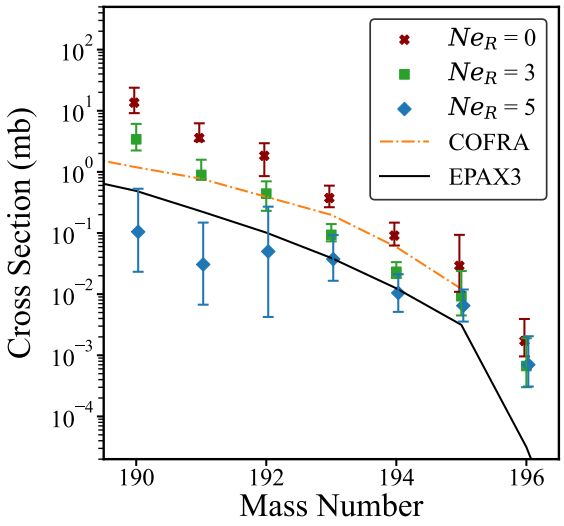

Figure 3.14: The cross sections of rhenium isotopes ($Z = 75$) for three separate possibilities of Ne_R (0, 3, and 5), as presented in Haak et al. [25]. Each possibility shown here was calculated by an AEWA of charge states from its corresponding plot shown in Figure 3.13. The `COFRA` model has also been added in for reference (dashed orange line).

range. The third consideration, denoted as C, was quantified by the average log difference of the experimental data and the cross section model `COFRA` [32]. C was interpreted as a simple residual in log space, where a value of $C = 1$ would indicate the experimental data is, on average, an order of magnitude away from the model for a given data point. This consideration ensures that the functional form of the cross section data is roughly a decaying exponential.

With a collection of optimization factors defined, a final optimization was performed. The numerical results of the normalization factor, N, were adjusted so that a value of $N = 1$ corresponded to the global minimum in that parameter space. Then the numerical results of each consideration was summed together with equal weight. This produced a quantifiable numerical value that represented the physical likelihood of each instance of Ne_R . The functional form of this value was such that a smaller value represented a more likely scenario. A three-dimensional figure of this discrete function is presented in Figure 4.8 of the following chapter.

Each point in the discrete function was then exponentially inverted using Equation 3.12 and smoothed out following the constraint in Equation 3.13. This ensured that the most likely Ne_R value occupied roughly 68% of the total probability for a given Z. These discrete probabilities

were used as the weights for the AEWA that condensed all possibilities of Ne_R into a single cross section measurement. One final AEWA was performed with the thick and thin target data sets to produce the final result of the cross section measurements.

$$f_{NeR}(x) = x^{1-P_{NeR}} \tag{3.12}$$

$$1/\sum_{i=1}^{Ne_R=5} f_i(x) \stackrel{!}{=} 68\% \tag{3.13}$$

In order to consider the bias of using `COFRA` as a reference, this final optimization process was performed using both `COFRA` and `EPAX3` as the reference for the N and C optimization parameters.

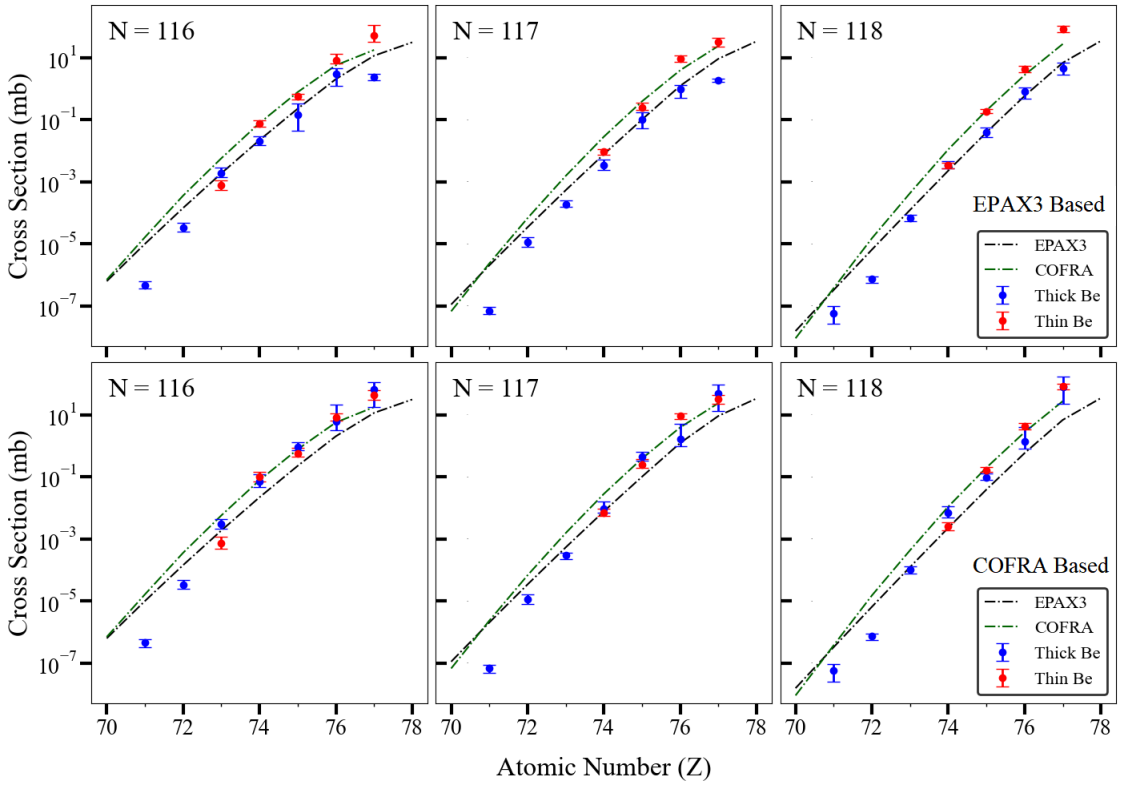

Figure 3.15: A comparison between the final cross section measurements produced from a `COFRA` based optimization (lower row) and `EPAX3` based optimization (upper row). The result of both thin and thick target data sets are shown in red and blue respectively. As a reference, the cross sections predicted from `EPAX3` and `COFRA` are shown by the the dashed black line and dashed green line, respectively. When using `EPAX3` as a basis for optimization, the thin and thick target results disagree. The `COFRA` based optimization shows overlap within error for most data points.

The cross section data from the thin and thick target data sets are shown in Figure 3.15. In the case of using COFRA as the reference in optimization, the cross section data from both thin and thick target data sets agreed well with one another. However, when using EPAX3 as the reference for optimization, there was noteable disagreement for higher Z elements. The results of both the cross section calculation and evidence of a new observation in this method of analysis will be presented in Section 4.3, and the motivation for this novel method will be discussed in Section 5.3.

The Ni target runs did not use this charge state analysis because the Ni target was relatively thick. Instead the charge state fractions were modified by a normalization constant determined in Figure 3.16. The yield patterns of each charge state predicted in LISE^{++} were normalized to match

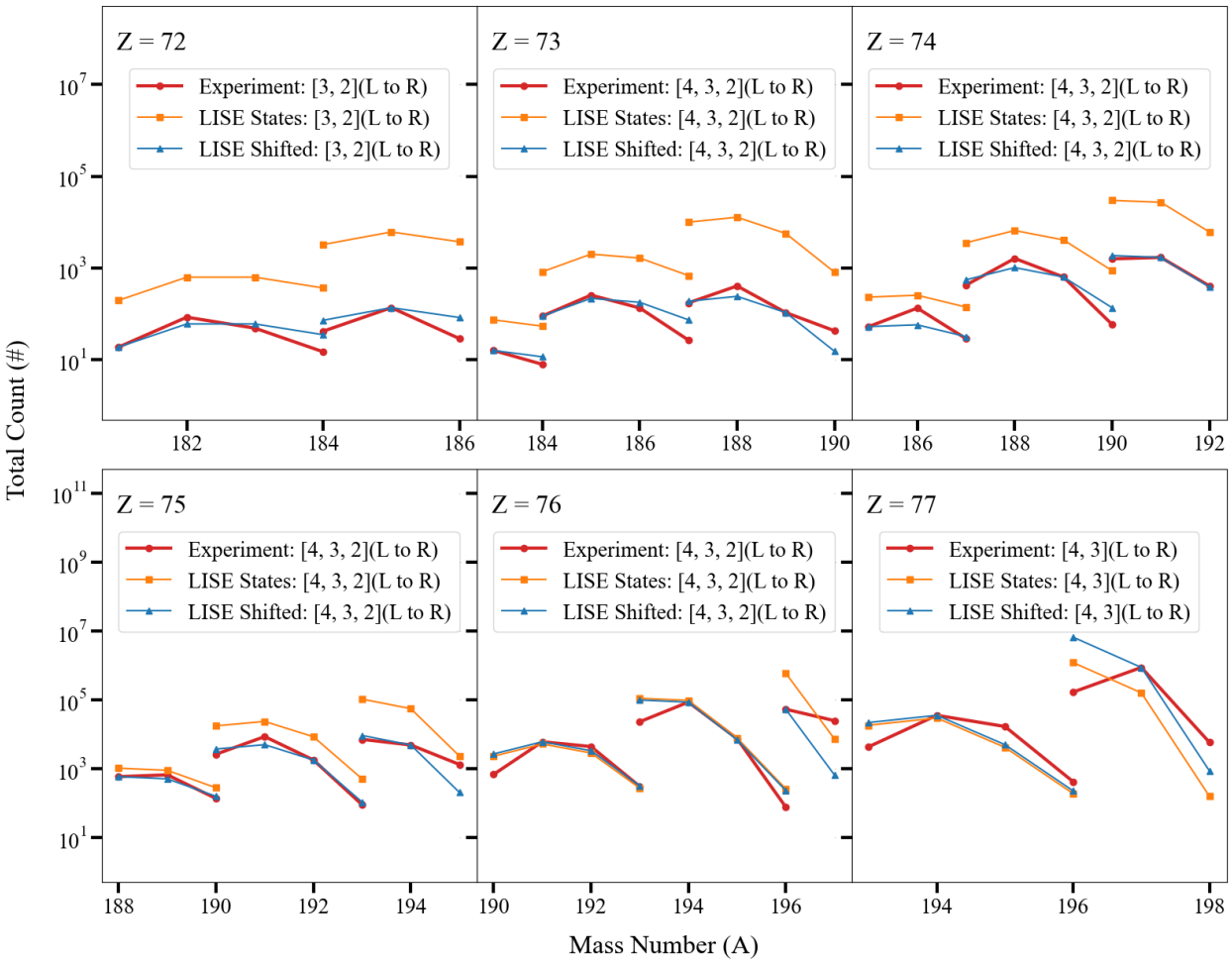

Figure 3.16: Yield curves for ions detected in data set D4a (see Table 2.1) are compared to LISE^{++} predictions. The LISE^{++} curves are shifted (blue) to match the yield curves observed in experiment. A total of six elements are shown, hafnium through iridium.

experimental data. The normalization constant was calculated by minimizing a weighted average of differences in log space between LISE^{++} predictions and experimentally recorded values. Each weight was proportional to the log of the transmission. The normalization constant was then applied to each respective charge state fraction in the Ni target analysis.

Chapter 4

Results

In both NSCL and FRIB experiments, new isotopes were identified and hence discovered. Additionally, the cross sections of rare isotopes produced in the NSCL experiment were extracted. Finally, a novel Monte Carlo based approach to charge state fraction calculations led to evidence of a new observation regarding the charge state of a projectile fragment immediately after reaction. These three results will be presented in the aforementioned order. The experimental results for the NSCL and FRIB experiments are presented here in a form closely following their descriptions in the 2023 Physical Review C publication [25] and the 2024 Physical Review Letters publication [58], respectively.

4.1 Particle Identification and New Isotope Discovery

Particle identification (PID) was performed using the magnetic rigidity ($B\rho$), time of flight (ToF), and total kinetic energy (TKE) method as described in Section 3.1. ToF was used to calculate the velocity and then extract the mass to charge ratio from Bp. The proton number (Z) was determined from energy loss (ΔE) in silicon detectors, and charge (q) was determined from the velocity and TKE. The visualization of PID spectra with multiple charge states was performed with a gate on a single charge state ($Z - q$), as shown in Figure 4.2. The quantity $A - 3q$ was selected to represent the mass of each particle group due to a cancellation of underlying systematic error in ToF [79].

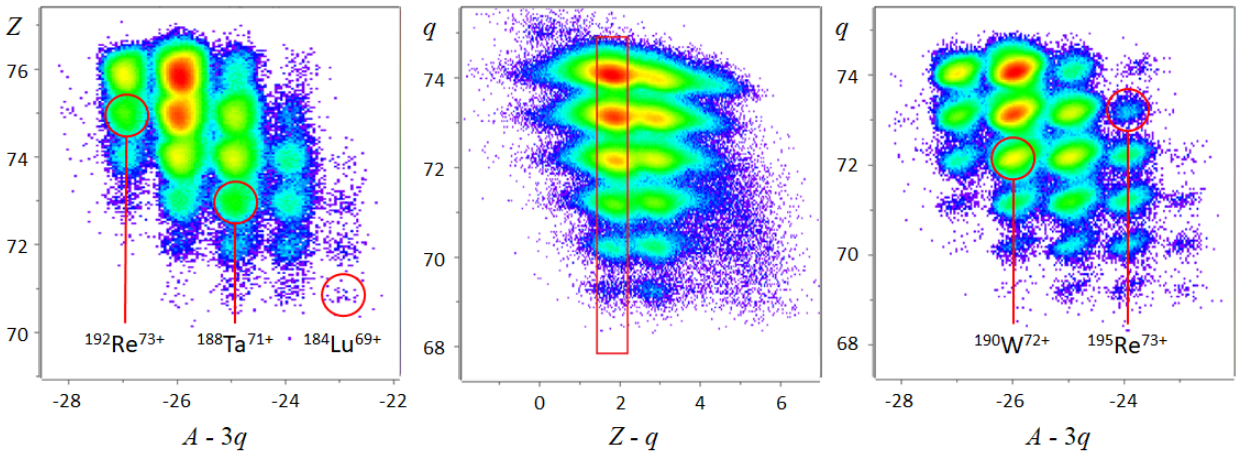

Figure 4.1: Particle identification spectra obtained from D4b settings (see Table 2.1), as presented in Haak et al. [25]. The separation of charge states is demonstrated in the $Z - q$ spectra (center) where helium-like and lithium-like charge states were observed. The charge state selection gate at $Z - q = 2$ (red rectangle) is applied to both left and right plots. The Z vs. $A - 3q$ (left) and q vs. $A - 3q$ (right) spectra demonstrate mass, ion charge, and elemental separation quality. A γ-ray spectrum observed in coincidence with $^{190}W^{72+}$ ions labeled here was used to confirm the identification (Figure 3.1).

Multiple charge states were successfully separated in particle identification (PID) spectra of both fragmentation experiments. The quality of mass, charge, and elemental separation can be seen in Figures 4.1 and 4.2. The resolution of the mass to charge ratio was $\sigma(A/q) = 0.005$ and $\sigma(A/q) = 0.001$ for the NSCL and FRIB experiments, respectively. This improvement in resolution was possible due to the use of multiple PPACs to reconstruct the $B\rho$ of charged particles, as opposed to using a single SSSD.

During the course of the NSCL experiment, three new isotopes, namely ^{189}Lu and ^{191,192}Hf, were discovered. The measured cross sections of these nuclides were found to be 0.037(24), 0.13(5), and 0.061(44) nb, respectively. The evidence for these new isotopes is shown in Figure 4.3. These one-dimensional mass spectra were generated by applying a series of PID gates as was outlined in Section 3.2. In this case, a Z and $Z - q$ gate were used. Counts to the right of the blue dashed line indicate previously undiscovered nuclides. These discoveries push the limit of Hf isotopes up to the point where the production of heavier isotopes would involve the pick-up of neutrons from the target. Although the experimental settings allowed for the potential observation of new isotopes

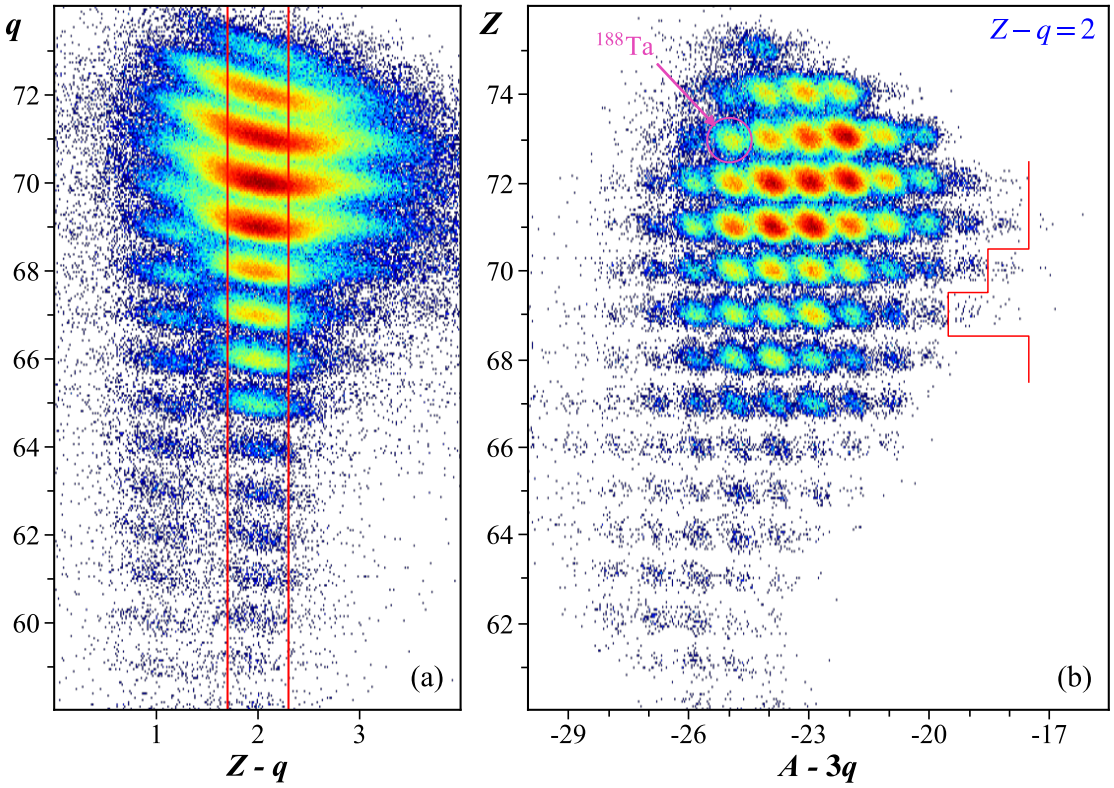

Figure 4.2: Two dimensional PID spectra of the fragments detected in the FRIB experiment, as presented in Tarasov et al. [58]. Spectrum (a) shows charge (q) vs charge state ($Z-q$), and spectrum (b) shows proton number (Z) vs mass ($A-3q$). The separation of charge states is visible in (a) and a gate is drawn on the He-like charge state ($Z-q=2$). This gate is applied to the spectrum shown in (b). The red line in the right spectrum indicates the limit of previously observed nuclides. ^{188}Ta is designated with a pink arrow for reference.

down to ^{181}Er, they were not detected.

The FRIB ^{198}Pt fragmentation experiment also produced new isotopes in this region. The five new isotopes were ^{182}Tm (29 events), ^{183}Tm (7), ^{186}Yb (27), ^{187}Yb (3), and ^{190}Lu (5). Evidence of these nuclides are presented in Figure 4.4. 52 counts of ^{189}Lu are also present, which is slightly over an order of magnitude higher than the NSCL results. One count of both ^{191}Lu and ^{184}Tm were observed. Assuming that the momentum distributions of each isotope are well within the acceptance of the separator and extrapolating the exponentially decreasing peaks along each isotopic chain, three counts are expected for ^{191}Lu and two counts are expected for ^{184}Tm. It is plausible these are the first observed events of ^{191}Lu and ^{184}Tm, however using Poisson statistics, the uncertainty is equal to the number of counts and cannot be claimed.

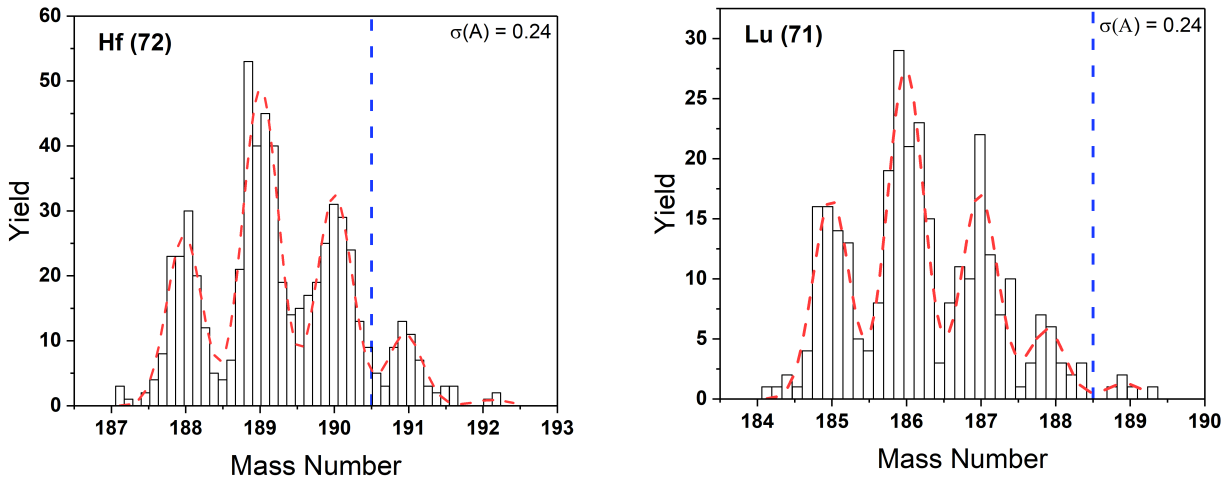

(a) Hafnium isotopes

(b) Lutetium isotopes

Figure 4.3: Mass spectra of hafnium and lutetium isotopes produced in the D7 settings of this experiment (see Table 2.1). This figure is presented as shown in Haak et al. [25]. Standard deviations produced with Gaussian functions at constant width (dashed red line) are given for each element. The dashed vertical blue line shows the limit of previously discovered isotopes for each element. The counts at $A = 189$ for $Z = 71$ and $A = 191$,192 for $Z = 72$ are evidence for the discovery of new isotopes.

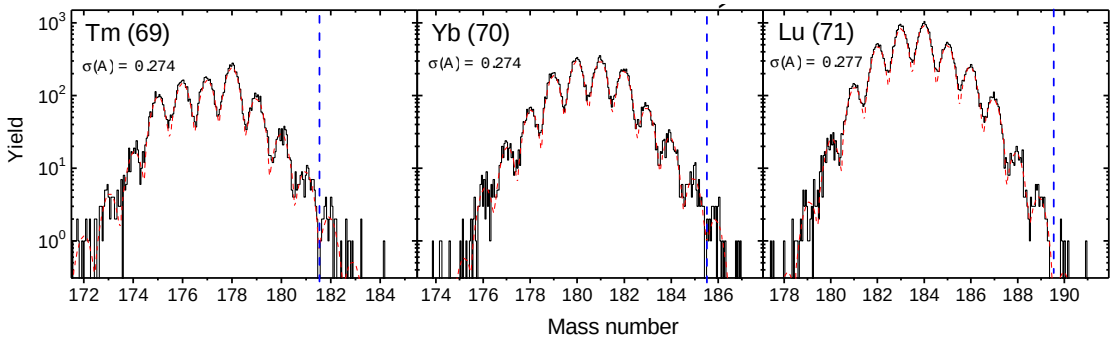

Figure 4.4: One dimensional mass spectra of fragments detected in the FRIB experiment, as presented in Tarasov et al. [58]. The black line is a histogram of the experimental data, the dashed red line is the series of Gaussian peaks fitted to the experimental data, and the blue dashed line is the previous boundary of discovery.

All together, eight new isotopes were discovered between these two experiments. Figure 4.5 summarizes these discoveries. Additionally, pick-up reactions of one to two neutrons were observed in both experiments. pick-up reactions closer to the primary beam were observed in the NSCL experiment, whereas pick-up reactions further out were observed in the FRIB experiment. This difference is most likely due to the fact that the FRIB experiment was tuned to more exotic $B\rho$

settings than the NSCL experiment.

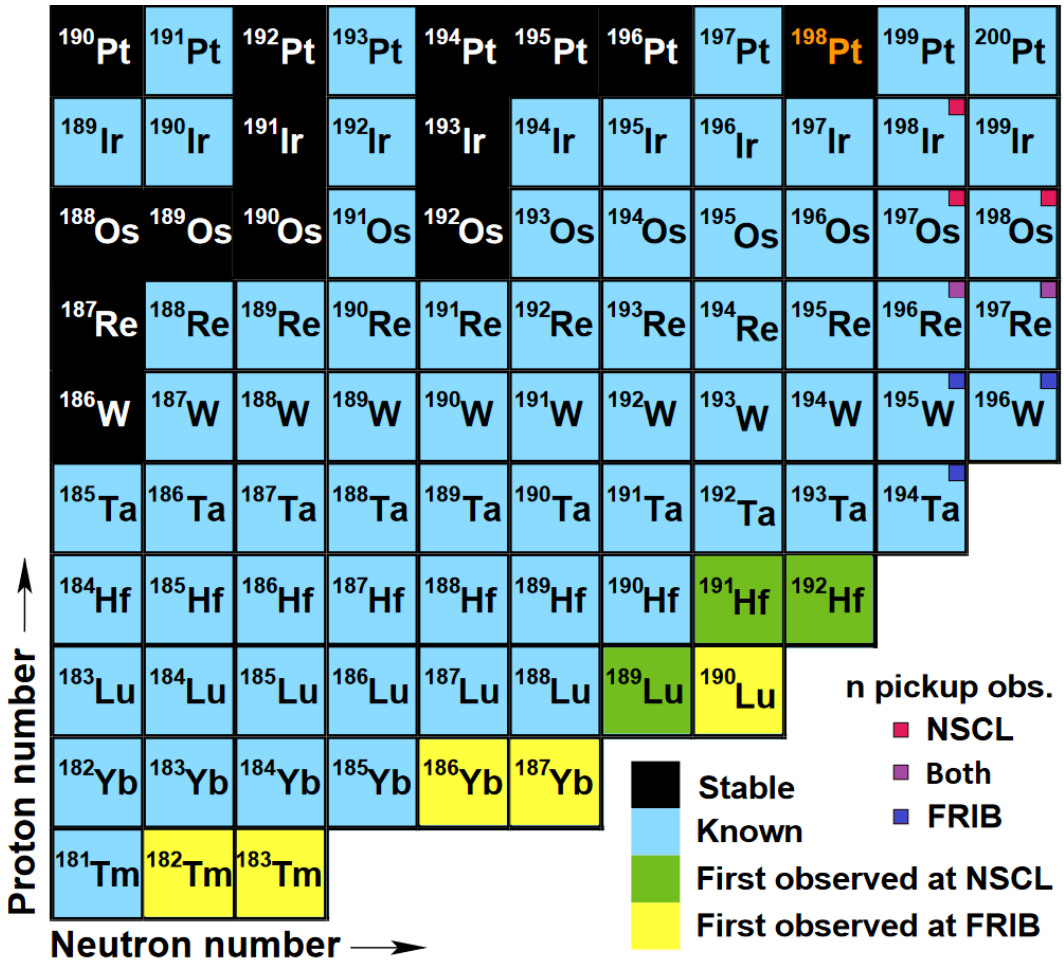

Figure 4.5: Chart of nuclides in the neutron-rich region "south" of ^{198}Pt, modified from Tarasov et al. [58]. New isotopes discovered at NSCL are shown in green, and new isotopes discovered at FRIB are shown in yellow. The small blue, red, and purple marks indicate pick-up reactions observed in the FRIB experiment, the NSCL experiment, and both, respectively.

4.2 Cross Sections

Using PDFs derived from discrete functionals, such as the one shown in Figure 4.8, the production cross sections were obtained for a total of 60 nuclides in the NSCL experiment. A selection of nine isotones are shown in Figure 4.6. Numerical details are available in Table A.1 of the appendix. Experimental cross sections follow trends predicted by `EPAX3` and `COFRA` models. However, there is a slight deviation away from the models for lower Z, where the measured cross section is lower

than predicted. This effect possibly appears in an odd-even pattern, where the cross sections of isotones with an even number of neutrons are often much lower than their odd counterparts.

No fragments with atomic number $Z < 70$ were produced in significant quantities at the rigidity settings employed in the NSCL experiment. Initially, the contribution of the "break-up" channel in terms of the abrasion-ablation model can explain this phenomenon, where the temperature of the excited pre-fragment exceeds the limiting temperature [80, 81]. However, a more detailed explanation involving the mean excitation energy of the prefragment can be provided

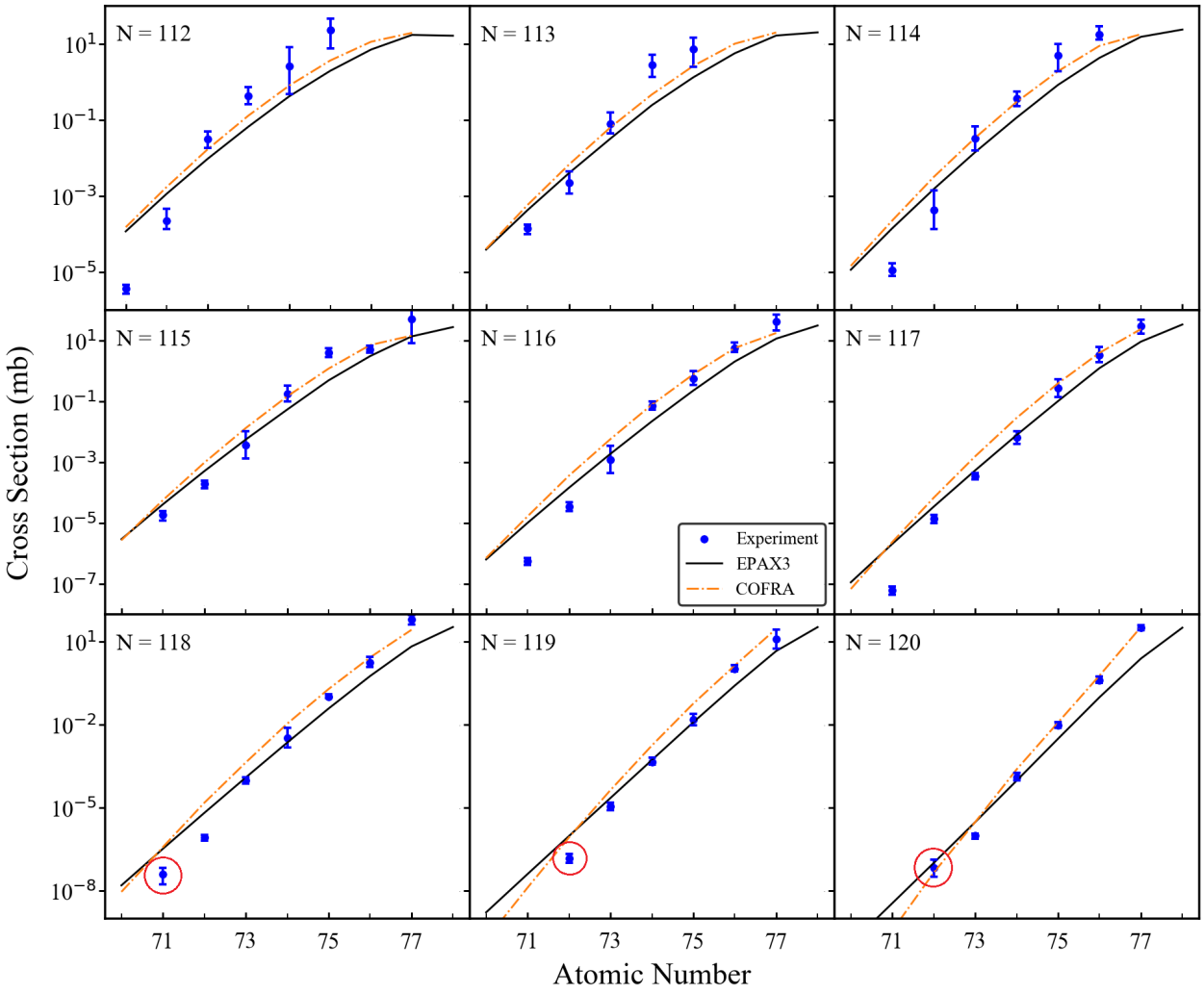

Figure 4.6: Cross section measurements of isotones ($112 \leq N \leq 120$) as a function of atomic number, as presented in Haak et al. [25]. These isotones were produced in the fragmentation reaction of ^{198}Pt (85 MeV/u) with ^{9}Be and are compared to `EPAX3` and `COFRA`. New isotopes are denoted with red circles.

with intranuclear cascade codes such as BeAGLE [82]. The average excitation energy for fragments of a ^{198}Pt projectile is several MeV per abraded nucleon higher than fragments of a ^{208}Pb or ^{238}U projectile. This finding was acquired through private communications with Dr. Oleg Tarasov (2024).

The measurement of ^{198}Pt (85 MeV/u) + Ni production cross sections was also performed with data set D4 (see Table 2.1). The estimated yield due to the Be stripper was calculated using the cross sections obtained from the Be only target runs. The Ni target was well above equilibrium thickness, resulting in the same outcome regardless of Ne_R . Therefore, instead of the Monte Carlo method described in Section 3.4, the transmission values provided by LISE^{++} were normalized to roughly match the experimental yield patterns. The results are shown in Figure 4.7. Assuming the cross section should scale geometrically with increasing size of the target nucleus, the Ni cross sections should be roughly 24% larger than the Be cross sections. However, for data with physical results, the Ni target cross sections were on average 20 times larger than the Be target cross sections. The cross sections of these 50 fragmentation products are listed in Table A.2 of the appendix.

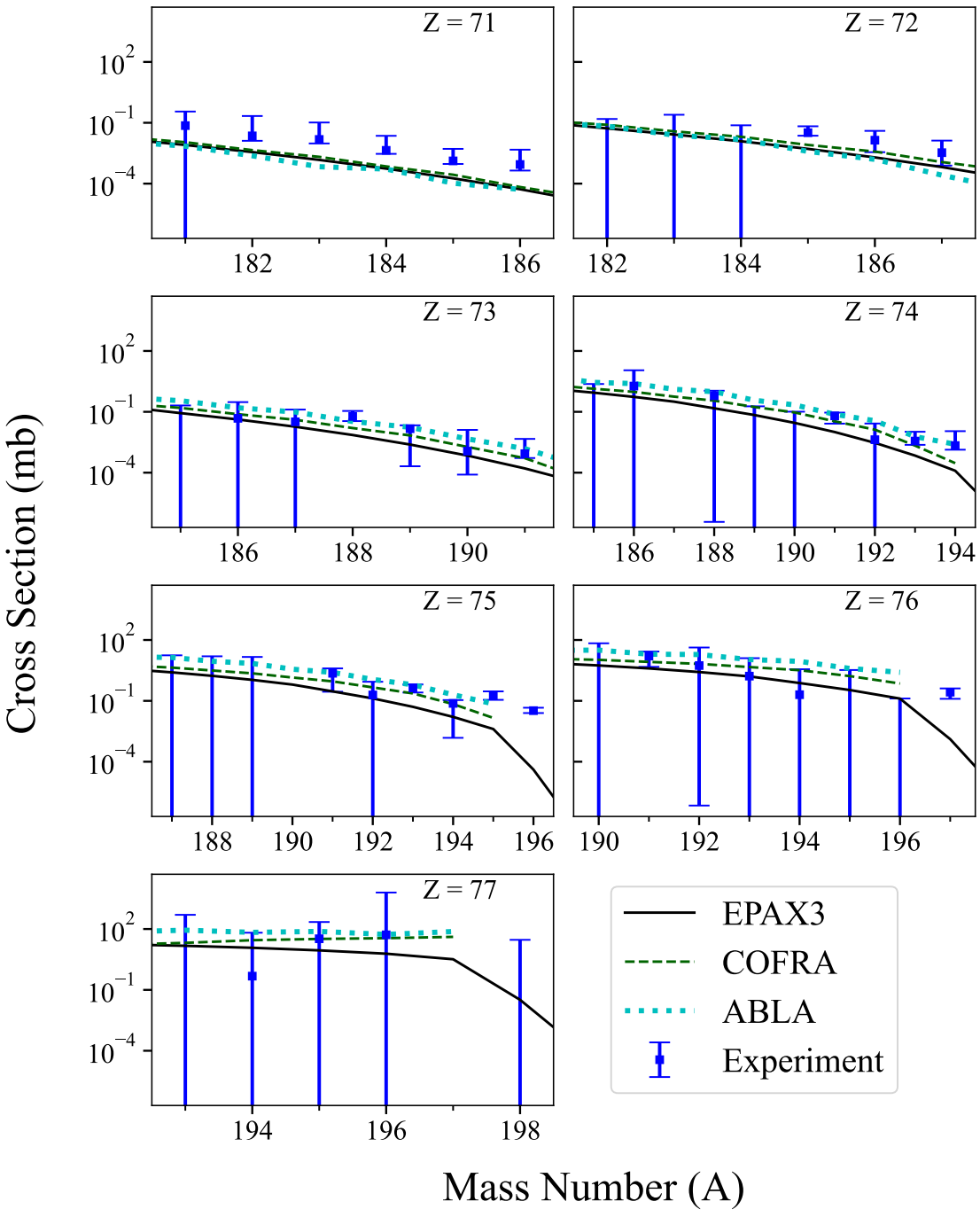

Figure 4.7: Experimentally measured cross sections of ^{198}Pt + Ni plotted with model estimates for reference. The subtraction of events due to the Be stripper resulted in negative values for the mean and lower error bar for many measurements. These cases were set to values off the chart.

4.3 Evidence of Residual Electrons

Following the novel charge state analysis outlined in Section 3.4, two separate probability distribution functions (PDF) of Ne_R were created from experimental data. The results are presented in Figure 4.8. Ne_R , or the number of electrons on the projectile residual immediately after fragmentation, was explored for the range of zero to five electrons. The PDFs in Figure 4.8 represent the likelihood that a given Ne_R is valid for a given number of protons removed (ΔZ). Each ΔZ represents an entire isotopic chain, from iridium to lutetium. The PDF for the thinner 23 mg/cm^2 beryllium target exhibits a relationship between ΔZ and Ne_R . The PDF for the thicker 47 mg/cm^2 target contains a less discernible trend.

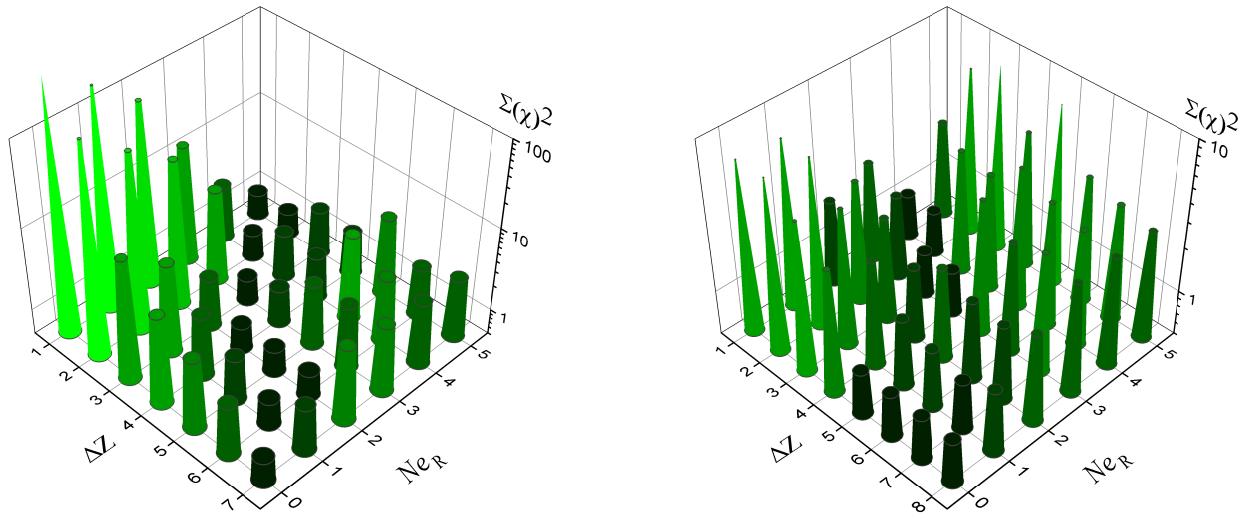

(a) 23 mg/cm^2 target thickness

(b) 47 mg/cm^2 target thickness

Figure 4.8: A summary of the most probable Ne_R values are presented for several values of abraded proton number (ΔZ), derived from the analysis of experimental data, modified from Haak et al. [25]. Two different target thicknesses are shown, the thinner 23 mg/cm^2 target and the thicker 47 mg/cm^2 target. The vertical color axis represents a combination of three optimization considerations: agreement of cross section measurements between ions of the same nuclei, physically possible cross sections measurements, and the consistency of the production cross section for a specific element as a function of nucleon number.

The presence of this trend in one data set and the absence in another can be explained by an equilibrium thickness argument. After a certain depth in a material, the electron pickup and

stripping effect becomes balanced in an equilibrium, and this depth can be calculated from properties of the material and the beam [32, 25]. The approximate equilibrium thickness of beryllium for ions between $71 \leq Z \leq 77$ at roughly 85 MeV/u is somewhere between 60 and 235 mg/cm^2 depending on the charge state model used [25]. This calculation demonstrates that the thinner target is considerably below equilibrium, but the thicker target is approaching equilibrium.

A relationship between the number of protons abraded in fragmentation (ΔZ) and the residual number of electrons on the fragmentation product immediately after reaction (Ne_R) was observed for the first time. As ΔZ increased Ne_R decreased. This could be related to the fact that as the difference between initial and final atomic ionization energies increases, fewer electrons will remain bound to the fragmenting nucleus. An additional factor could also be electron shake-off from the sudden change of velocity during the abrasion step, where more velocity is lost with more abraded nucleons. While such effects are challenging to detect due to continuous ionization and electron pickup of ions passing through a medium, this observation was possible due to the following three factors: (i) the relative excess of electrons on the primary beam ($^{198}Pt^{61+}$ has 17 electrons), (ii) the use of a thin production target well under equilibrium thickness, and (iii) the limited use of materials in the beam path.

Chapter 5

Discussion

The primary goal of this work was to study the production of neutron-rich rare isotopes near $N = 126$ via medium energy fragmentation reactions. This previously unexplored fragmentation of 50 - 200 MeV/u ^{198}Pt led to the discovery of eight new isotopes, and provided insight into the reaction mechanism that produced them. The implications of these isotopes and their production cross sections for nuclear structure and reaction studies will be discussed in this chapter. The cross section data were used to test the validity of several fragmentation models in the neutron-rich region near $N = 126$. Finally, the significant issue of charge states associated with high Z isotopes at intermediate energies will be discussed. While this issue impacts PID to a significant degree, its impact on cross section calculations arguably adds a much greater challenge to understanding the production of rare isotopes in the $N = 126$ region. Therefore the novel charge state analysis developed in this work will be discussed in detail in this chapter.

5.1 Uses for New Isotopes

As presented in Section 4.1, eight new isotopes were discovered in this work. In principle, these isotopes could now be prepared and delivered to nuclear experiments. On the basis of beam intensity and time extrapolation, the new isotopes could be delivered anywhere between 373 particles of ^{187}Yb to 23,271 particles of ^{191}Hf in the span of a week-long experiment. Operation of ARIS in the standard $k = 3$ optics setting [66] would likely yield a gain of 20 times these numbers. It is also important to note that with successive accelerator upgrades, the increase of primary beam intensity is likely to continue to push the boundary of discovery in this region. This experiment was run at

1.5 kW, and eventually 400 kW should be possible. With the FRIB400 upgrade [26], additional gains of 10x are likely. Delivering new isotopes to scientific users of FRIB, or producing these isotopes in other facilities, can make an impact in a wide variety of nuclear physics experiments, such as isomer studies, shape evolution, and reaction mechanism studies. A selection of useful isotopes for nuclear reactions and structure studies are visualized in Figure 5.1.

The NSCL ^{198}Pt fragmentation experiment was a collaboration with the University of Massachusetts Lowell to explore nuclear structure in the neutron-rich Hf region. These experimental

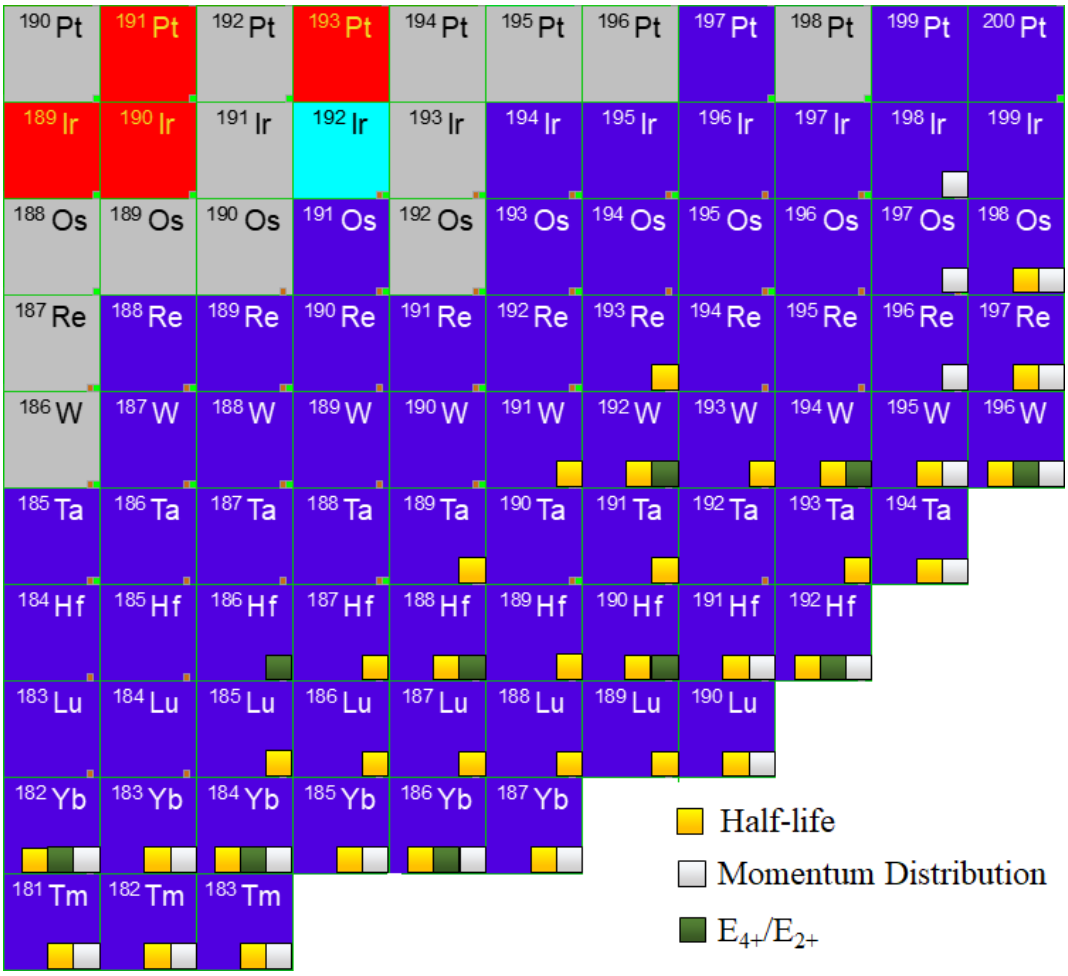

Figure 5.1: The chart of nuclides near $N = 126$, generated with LISE^{++}. Isotopes that can extend the reach of previous nuclear structure studies through the E_{4+}/E_{2+} ratio are denoted by a green square. Isotopes that can aid in the development of existing nuclear reaction models through the measurement of momentum distributions are denoted with a white square. All nuclei which have not had their ground state beta-decay half-life directly measured are denoted with the gold square. The color of each isotope tile represents a decay mode, with grey indicating stable isotopes.

settings produced not only new isotopes but significant rates of other exotic isotopes, such as ^{186}Hf. The main goal of the nuclear structure study was to explore K isomers in neutron-rich Hf isotopes, and a manuscript is currently in preparation [P. Chowdhury, Private Communciations]. The isomeric decays of these heavy nuclides provide useful insight to the collective motion of nuclear matter. Neutron-rich nuclides near $N = 126$ provide a parallel to the super-heavy element region, where deformations are the key to observing longer lived isomers than the ground state [83].

The low-lying excited states of neutron-rich tungsten isotopes are also of interest to nuclear structure, specifically nuclear shape evolution studies [84, 43]. The ratio of the first 4^+ excited state and 2^+ excited state for even-even nuclei, such as certain isotopes of tungsten, can provide information about the shape of the ground state of the nucleus [84]. Previous studies have explored this ratio up to $N = 116$ for W isotopes and $N = 112$ for Hf isotopes [43], but these can now be expanded all the way out to $N = 120$ for both elements (see Fig. 5.1). Even-even Yb isotopes are also relatively unexplored and may also be considered for nuclear shape evolution studies.

Reaction mechanism studies can also benefit from these new isotopes by extending our experimental knowledge of momentum distributions populated in fragmentation reactions. One such example of using momentum distributions to formulate a better understanding of fragmentation is the design of `LISEAA` [85]. Experimental measurements of momentum distributions are sparse for projectile fragments in the neutron-rich region near $N = 126$. The momentum distributions of ions produced in the fragmentation of 950 MeV/u ^{197}Au were measured, however this data only reached the five proton removal channel. The discovery of ^{192}Hf from the fragmentation of ^{198}Pt extends this reach to 6 proton removal ($\Delta Z = 6$). Additionally, elements below $\Delta Z = 7$ were not considered in the cross sections measurements, whereas the FRIB experiment was capable of producing $\Delta Z = 8$ and 9. Another significant contribution to the understanding of heavy-ion collisions at intermediate energy is the pick-up of nucleons from the target. A total of eight nuclides created from pick-up reactions were observed between the two fragmentation experiments in this work. All 21 nuclides mentioned here are highlighted in Figure 5.1. The `COFRA` reaction model, along with others, is considered in the next section for the interpretation of cross section results.

5.2 Interpretation of Cross Section Results

The cross section results from Section 4.2 were compared to four separate models: `EPAX3` [15], `COFRA` [32], `ABRABLA07` [46], `LISEAA` [85]. The strengths and weaknesses of each model will be discussed, along with the available user options. Finally, a comparison of the ^{198}Pt + Ni cross sections to the ^{198}Pt + Be cross sections will be briefly discussed.

`EPAX3` is a parametrization of experimental production cross sections measured from various fragmentation reactions [15]. The EPAX formula is a product of two main components: the mass yield and the charge dispersion. The mass yield is a sum of all isobars of a given fragment mass A, and the charge dispersion is a Gaussian-like function that describes the distribution of elements within a given isobaric chain. There is no underlying physics in the EPAX formula, and it simply aims to reproduce the functional shape of experimental data. Despite this disadvantage, EPAX3 still provides reasonable estimates for a wide variety of cases. However, EPAX3 was unable to produce consistent agreement with the experimentally measured cross sections in this work. Most notably, EPAX3 underestimates cross sections for the high-Z fragments in this work, and overestimates cross sections for low-Z fragments (see Fig. 5.2).

`COFRA` (cold-fragmentation) is an analytical abrasion-ablation code which only considers neutron evaporation in the ablation step. The publicly available code [86] only allows four parameters to be varied: mass number and atomic number for both the projectile and the target. All other physical parameters, including beam energy, are contained within the source code and cannot be modified directly. This prohibits testing the impact and validity of given assumptions in the model. However, `COFRA` was designed to provide accurate estimates for cross sections of cold-fragmentation, a process where relatively small excitation energies are populated in the projectile during peripheral collisions. This is the case when comparing `COFRA` to experimental data in this work. `COFRA` estimates cross sections of higher mass elements closer to the projectile reasonably well, only significantly deviating beyond the removal of four protons (see Fig 5.2).

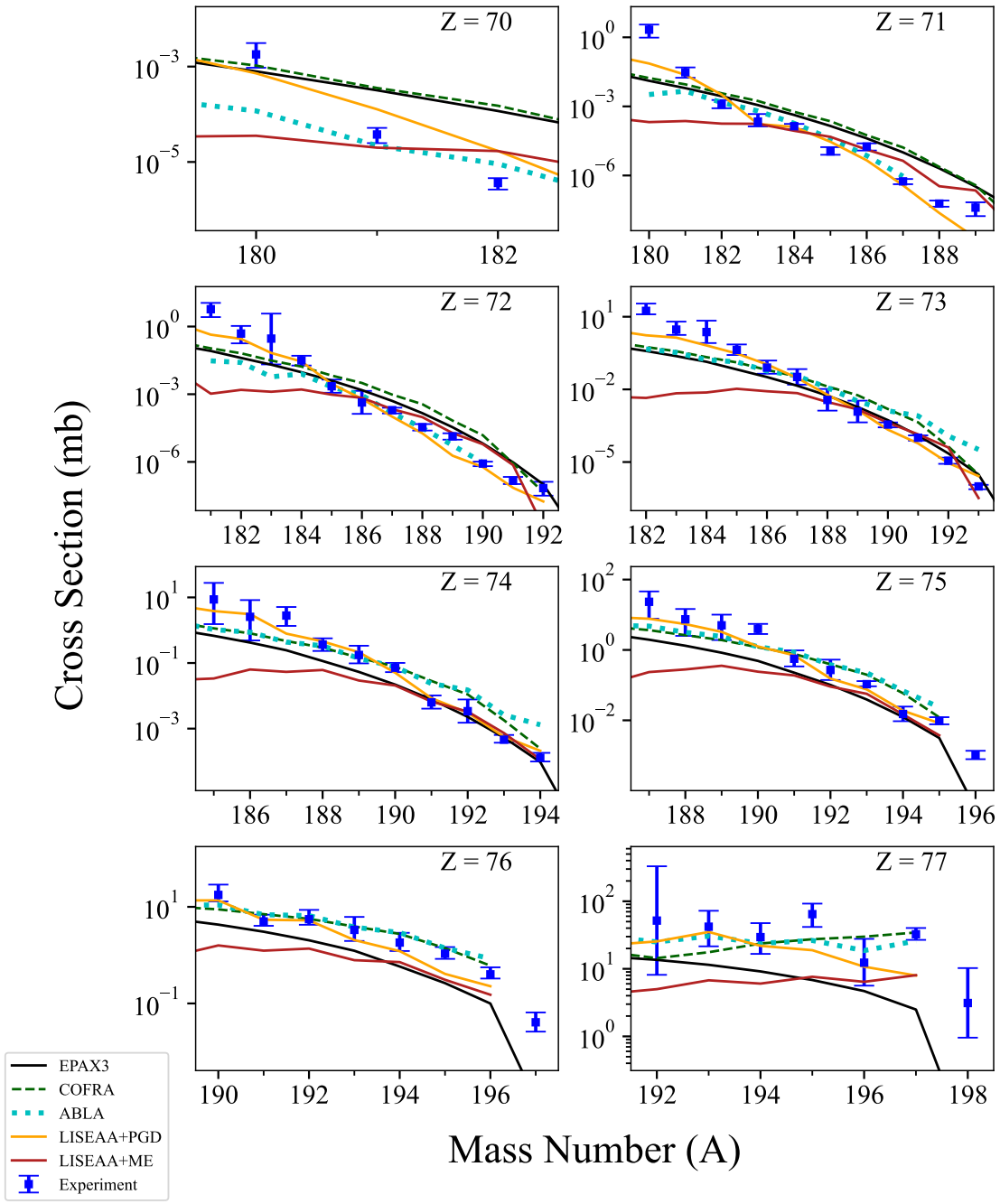

Figure 5.2: Experimental cross section measurements of 85 MeV/u ^{198}Pt + ^{9}Be are compared to five different models: `EPAX3`, `COFRA`, `ABLA`, `LISEAA+PGD`, and `LISEAA+ME`. The closest agreement occurs with `LISEAA+PGD` and `ABLA` models. A quantitative measure, calculated from an error-weighted average of residuals in log space is given in Table 5.1.

`ABRABLA07` (`ABLA`) is a Monte Carlo abrasion-ablation code which considers a wide range of decay channels including fission and emission of intermediate mass fragments (IMF). `ABLA` has

a couple more adjustable parameters than COFRA, allowing the user to set the projectile energy and toggle thermal expansion of the projectile residual on and off [46]. The impact of thermal expansion on cross section estimates for 85 MeV/u ^{198}Pt + Be was tested, but no significant difference was noted. When compared to experimental results in this work, ABLA estimated cross sections reasonably well for both high-Z and low-Z isotopes (see Fig 5.2). This is most notably true for the heaviest neutron-rich isotopes of lutetium and hafnium, which were measured to be over an order of magnitude lower than both COFRA and EPAX3. However, ABLA struggled providing an isotopic slope that could match experimental data for every element. For intermediate elements ($73 \leq Z \leq 75$) ABLA estimated a cross section slope steeper than experimental values. It is important to note that this feature in the experimental data could be influenced by charge states as can be seen in the cross sections of individual ions in Figure 5.6.

The statistical nature of Monte Carlo codes makes estimating small cross sections challenging. In order to extend the reach of ABLA, the source code was modified to consider a restricted range of values for impact parameter and excitation energy of the prefragment. These changes led to a decrease in runtime by roughly two orders of magnitude. A qualitative depiction of this impact is shown in Figure 5.3, demonstrating the difference between default ABLA and modified ABLA. The

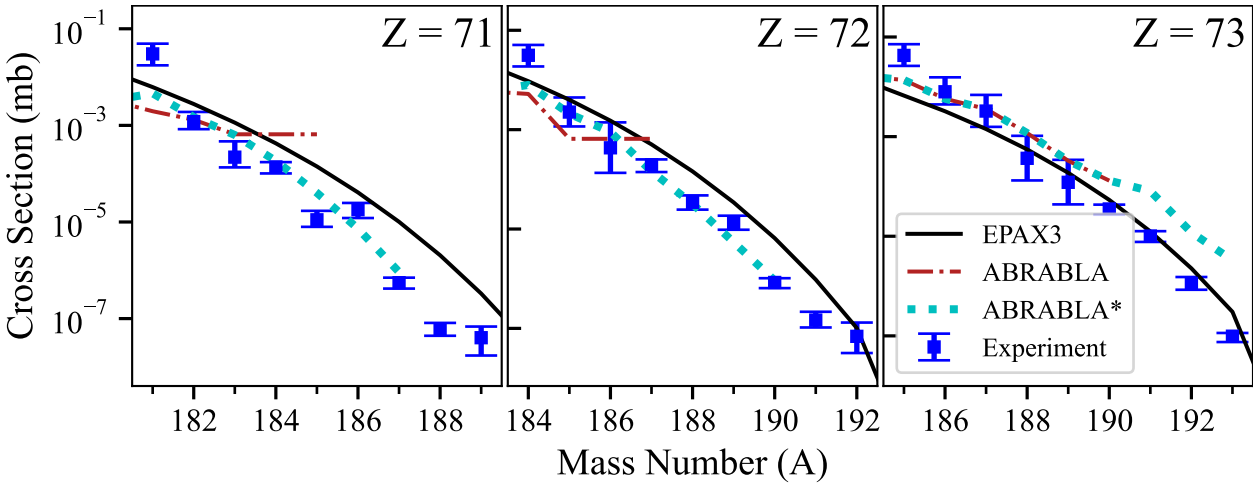

Figure 5.3: Experimental cross section measurements of 85 MeV/u ^{198}Pt + ^{9}Be are shown in blue for three representative isotopic chains: Z = 71 lutetium, Z = 72 hafnium, and Z = 73 tantalum. EPAX3, ABRABLA07, and modified ABRABLA predictions for this reaction are indicated by the solid black line, dotted-dashed red line, and dotted cyan line, respectively.

most significant impact to runtime was the restriction of the impact parameter. This is one of the first calculations performed, and runtime can be saved by not considering small impact parameters that lead to large excitation energies or breakup of the projectile. Other minor changes that contributed to these improvements included disabling evaporation channels known to play little to no role in the creation of fragments of interest. Both IMF and fission channels were disabled during the use of `ABLA` in this work.

Individual events can be inspected in Monte Carlo codes, allowing for the step-by-step description of low statistics processes. `ABLA` allows the user to generate an event file that contains detailed information about every product generated during runtime. This includes impact parameter, excitation energy of the prefragment, velocity distributions of the prefragment, and both the initial and final values of mass and charge of the projectile fragment. This functionality allowed for the precise definition of impact parameter and excitation energy limits that were used to reduce runtime. A

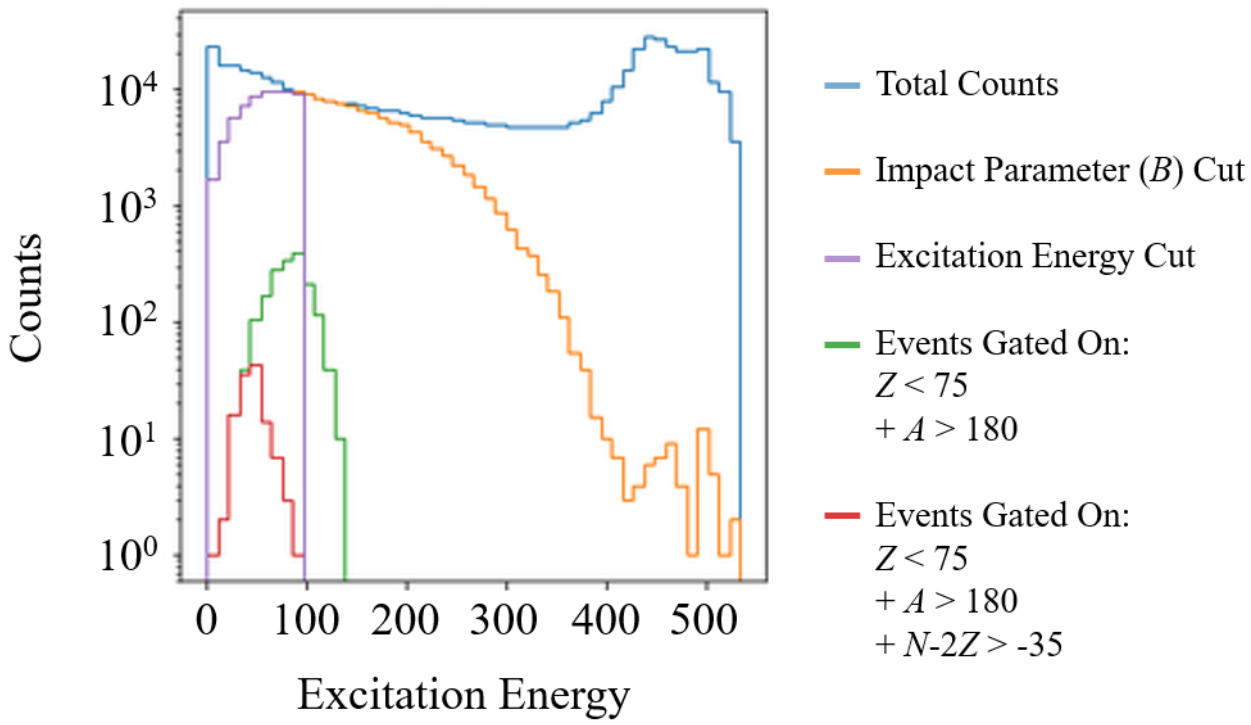

Figure 5.4: A histogram of pre-fragment excitation energies for events generated in the `ABLA` code. The impact of several gates are shown in the excitation energy spectrum. An impact parameter (B) gate is shown in orange. Within the B gate, another excitation energy gate is shown in purple. The excitation energy of specific isotope regions are shown in red and green, as indicated in the key.

representative example of this functionality is shown in Figure 5.4. The total events generated are shown in blue and every subsequent color is a subset of the total. The first cut applied was to impact parameter, reducing the data to only peripheral collisions. The second cut was simply drawn on low excitation energy events of the impact parameter subset. To demonstrate the location of exotic fragments within this excitation energy spectrum, two specific regions were selected, shown in green and red. These are the most neutron-rich fragments just below the primary beam. Their excitation energies are small.

LISEAA is an analytical abrasion-ablation code with multiple adjustable parameters for both the abrasion and the ablation step. In the abrasion step, several excitation energy models are provided as options in the LISE^{++} code. The two models selected to be presented in this work are the Parametrized Gaussian Distribution (PGD) [87] and the Mean Exponential (ME) model [88]. The PGD model assumes the excitation energy follows the functional form of a Gaussian distribution. Both the mean excitation energy and the width of the Gaussian distribution is calculated from a second order polynomial that is a function of the number of abraded nucleons. The ME model assumes the functional form of the excitation energy is exponential with a mean value T that is

Table 5.1: The error weighted average of residuals in log-space for each model compared to experiment was tabulated. A value of 1.00 indicates the model deviated on average one order of magnitude from experimental data. Values are given for each element, as well as a sum for each model. The minimum for each isotopic chain is bolded. For the complete list of parameter values used in the LISEAA+PGD model, see Table A.4 of the appendix.

Z	EPAX3	COFRA	ABLA	LISEAA+PGD	LISEAA+ME
70	1.071	1.111	**0.509**	0.566	0.754
71	0.940	1.043	0.534	**0.421**	0.887
72	0.677	0.839	0.430	**0.368**	0.898
73	0.507	0.631	0.897	**0.297**	0.906
74	0.379	0.388	0.532	**0.165**	0.562
75	0.544	0.331	0.390	**0.197**	0.641
76	0.484	**0.145**	0.170	0.178	0.595
77	0.829	0.212	**0.179**	0.385	0.694
Sum	5.431	4.700	3.641	2.577	5.937

used to normalize the function. In the ablation step, the user can choose to enable or disable any number of decay modes, including 1n, 2n, 1p, 2p, α, and several others. This work only considered the 1n, 1p, α, fission, and breakup modes. Both LISEAA+PGD and LISEAA+ME were optimized to best fit the experimental data. LISEAA+PGD was able to provide reasonable estimates for most nuclei observed in this work (see Fig. 5.2). Specifically, the agreement between LISAA+PGD and experimental data for light isotopes of lighter elements was unrivaled among all models tested. On the other hand, LISEAA+ME had the polar opposite result consistently deviating from experimental cross sections of lighter isotopes for every element by several orders of magnitude.

Experimentally measured cross sections for 85 MeV/u 198Pt + Be were most accurately reproduced by LISEAA+PGD and ABLA . A quantitative measure of each model's accuracy is presented in Table 5.1. It is important to keep in mind the differences between each model to understand the implications for future experiments. LISEAA+PGD was numerically optimized to fit the experimental data, and is therefore a tightly trained model on a specific data set. The results of this optimization should be used for future experiments under similar settings. The complete list of optimized parameter values for this data are listed in Table A.4 of the appendix. In order for LISEAA+PGD to play a role in planning experimental rates of secondary RI beams, previous experimental results are needed to lay the groundwork. As for ABLA , estimates were generated without prior knowledge of the experimental data. Therefore, while not as accurate as LISEAA , ABLA can be referenced for a wider range of scenarios, even in the absence of pre-existing experimental data.

The production cross sections of 85 MeV/u ^{198}Pt + Ni was extracted from a Ni target + Be stripper setup using the experimental Be cross sections presented in this work. The experimental ^{198}Pt + Be cross sections were used to estimate the number of fragments produced in the stripper, and the observed counts were adjusted by this estimate. This introduced significant error into the calculation in two ways. Firstly, the experimental measurements of production cross sections for ^{198}Pt + Be contained their own significant errors from the previous analysis. Second, the two step process of first estimating the counts due to the stripper and then calculating the ^{198}Pt + Ni cross sections from the remaining counts, doubled the contribution of the transmission error in the Ni

target settings. The consequence of these significant errors are demonstrated in Figure 5.5. While the upper limit of most fragments was successfully calculated, the lower limit was non-physical when the estimated counts due to the Be stripper was greater than the experimentally observed counts.

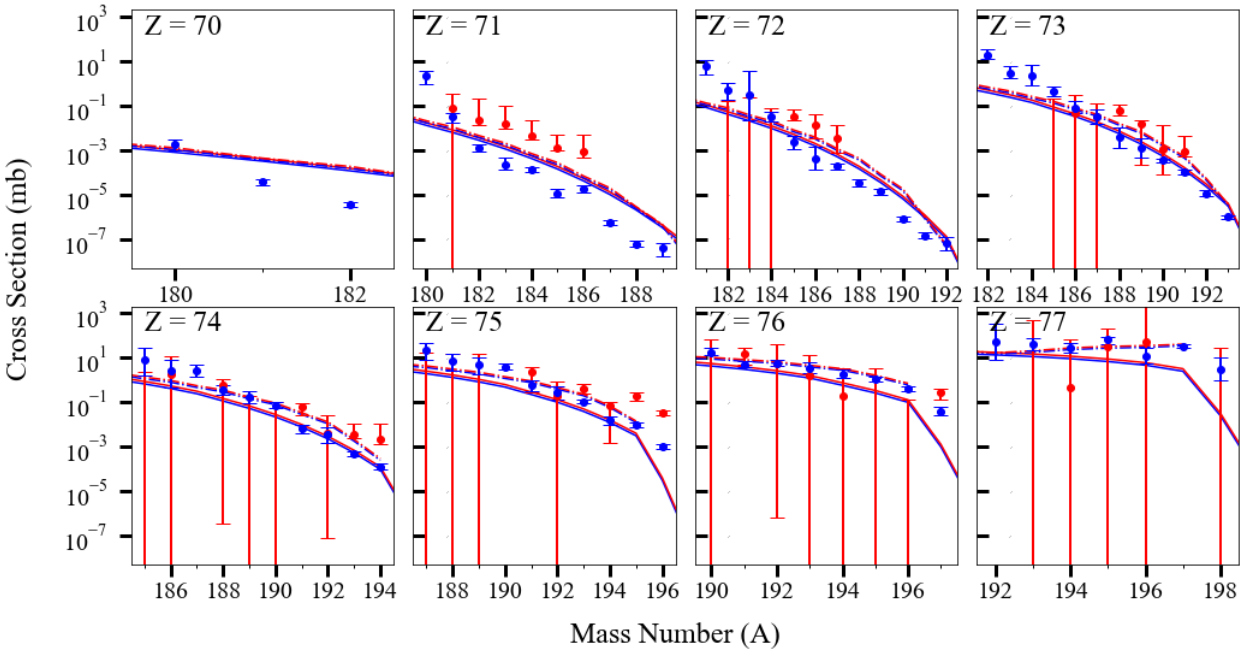

Figure 5.5: A comparison of cross section measurements for isotopes produced from ^{198}Pt + ^{9}Be fragmentation (shown in blue) and ^{198}Pt + ^{59}Ni fragmentation (shown in red). Both `EPAX3` and `COFRA` are plotted in solid lines and dash-dotted lines, respectively for reference. The color for the references match the data sets.

It is difficult to draw a meaningful conclusion with the large uncertainties presented in the data. However, it can be noted that Ni cross sections are systematically higher. This indicates that, within error, the nickel target cross sections are larger than the beryllium target cross sections. On average, the Ni cross sections were approximately 20 times larger than the Be cross sections for data with physical results. This is considerably larger than the increase in cross section that would be expected due to the difference in size between the Be and the Ni nucleus. This result suggests that, for projectile fragmentation, heavy neutron-rich targets could be preferable over beryllium and carbon targets if the multiple charge states could be handled effectively.

5.3 Motivations and Limits of the Novel Charge Analysis

As presented in Section 4.3, the charge state of the projectile residual immediately after reaction (Ne_R) can significantly impact charge state distributions of fragments produced in thin targets. The effects of Ne_R are great enough that a rough value can be extracted from experimental data. A novel charge state analysis, involving the enumeration of all possible Ne_R values via Monte Carlo simulation, was designed and applied. The motivation, strengths, and weaknesses of this method will be discussed in this section. Finally, alternative methods will be briefly discussed.

There was a charge-related inconsistency in cross section measurements when using the default charge state model in LISE^{++} (see Figure 5.6). The production cross section of a given nuclide is independent of its charge, however there was a considerable discrepancy between two ions of the same nuclide in the experimental data. The measurements did not overlap, even within error. In order to correct this, the fractions for each charge state were manually adjusted until the cross section measurements overlapped. For example, the $Z - q = 3$ charge state for $Z = 76$ in Figure 5.6 was shifted down until both the $^{195}Os^{73+}$ and $^{196}Os^{73+}$ measurements overlapped with the $^{195}Os^{74+}$ and $^{196}Os^{74+}$ measurements of the $Z - q = 2$ charge state. Next, the $Z - q = 4$ charge state was

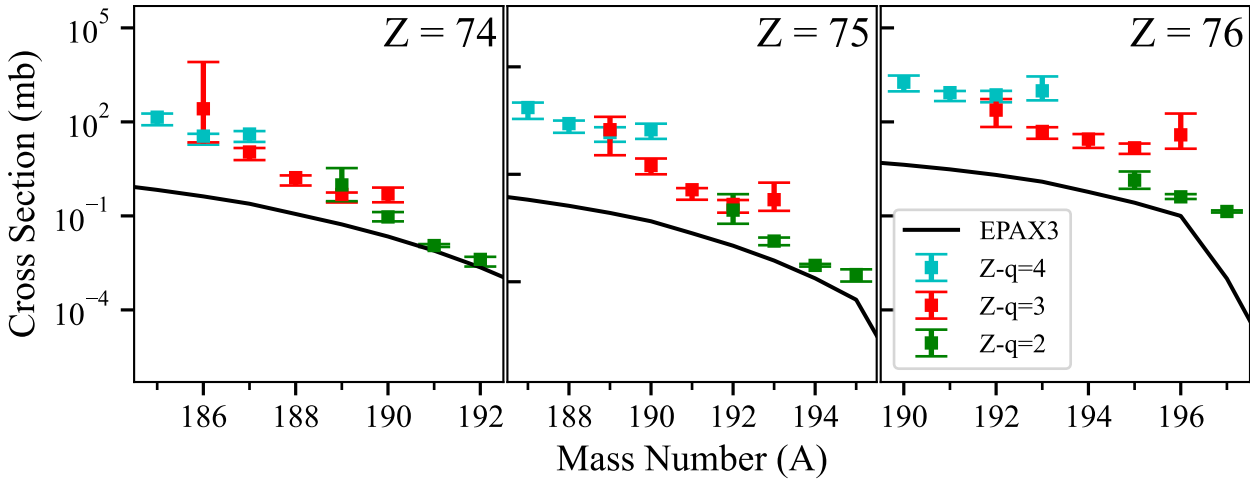

Figure 5.6: Preliminary cross section calculations using the default settings in LISE^{++}. Default settings include $Ne_R = 0$, the GLOBAL charge state model, and the distribution method of calculating charge states (as opposed to the Monte Carlo method). The data set presented here is D3b from Table 2.1.

shifted down to overlap with the already shifted $Z - q = 3$ charge state. However, this procedure did not apply a shift to the final charge state, $Z - q = 2$. In other words, there was no global normalization. Despite the fact that the charge state fraction of $Z - q = 2$ contained uncertainty, there was no statistically defined range for the uncertainty. Therefore, the ambiguity of this final normalization step led to reconsidering the methodology of the charge state analysis.

In order to solve the charge-related inconsistency, the underlying physical processes of the charge state model were systematically explored and questioned. Initially, the 85 MeV/u $^{198}Pt^{61+}$ beam enters the production target with 17 electrons and experiences both electron pickup and ionization, simultaneously. At the given beam energy and initial charge state, the ionization cross sections dominate, rapidly stripping the projectile of its electrons (see Figure 5.7). At a certain depth, the electron pickup and ionization effects begin to balance each other out, and the variance of the mean charge state, $< q >$, approaches a minimum. This behavior is illustrated in Figure 5.7, where $< q >$ can be seen rapidly increasing upon entering the target, and eventually leveling off at around $< q >= 75.5+$. The thickness at which this balance of electron pickup and ionization occurs is defined as the equilibrium thickness. Increasing the thickness past this point leads to only minor changes in the charge state distribution, provided the beam does not deposit a significant portion of its kinetic energy in the target. According to Scheidenberger [77], the equilibrium thickness can be estimated via the following expression:

$$x_{eq} \simeq \frac{4.6}{\sigma_K^1 + \sigma(0,1)/2} \tag{5.1}$$

where σ_K^1 is the ionization cross section for an electron on the K-shell, and $\sigma(0,1)$ is the one-electron attachment cross section into the bare projectile from all filled target shells. Ionization cross sections can be approximated by first order perturbation theory methods such as the plane-wave born approximation (PWBA). The electron attachment cross section is a combination of two processes, radiative electron capture (REC) and non-radiative electron capture (NRC). REC dominates for small Z of the target nucleus. NRC becomes significant at larger Z of the target nucleus, granted the beam energy is sufficiently low (less than 300 MeV/u) [77]. Using Equation 5.1, the equilibrium

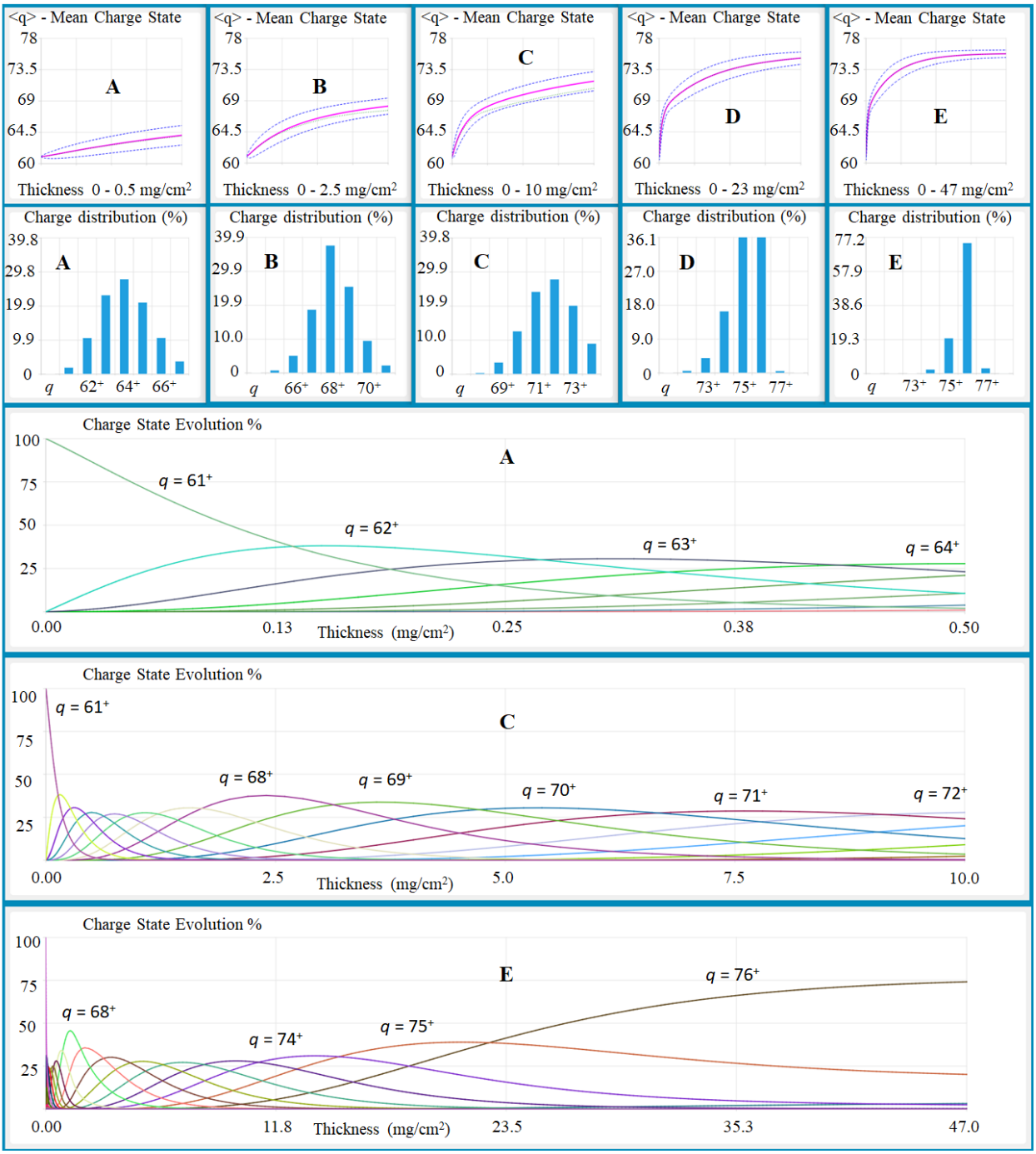

Figure 5.7: ETACHA4v3 was used to calculate the mean charge state (first row), charge state distributions (second row), and charge state evolution (bottom three) of $^{198}Pt^{61+}$ passing through ^{9}Be. A total of five increasingly thick samples of ^{9}Be are shown (A,B,C,D,E = 0.5,2.5,10,23,47 mg/cm^2). In the first row, the mean charge state is indicated by the pink solid line, the standard deviation is indicated by the dashed blue line. Samples A, C, and E are chosen for the charge state evolution plots.

thickness for a 85 MeV/u ^{198}Pt beam passing through beryllium is x_{eq} = 121.60 mg/cm^2. The same beam passing through nickel results in an equilibrium thickness of x_{eq} = 52.09 mg/cm^2. For a higher energy 186 MeV/u ^{198}Pt beam passing through carbon, the equilibrium thickness is x_{eq} = 195.40 mg/cm^2.

The fragmentation of the primary beam may occur at any depth in the production target. The probability of the fragmentation reaction occurring in a given charge state of the primary beam is proportional to the integral of the charge state evolution curves in Figure 5.7, and several examples are provided in Figure 5.8. These curves indicate that a considerable number of primary beam electrons are present during most reactions in the target.

The projectile fragmentation reaction mechanism can be described by the two step Abrasion-Ablation model. In the abrasion step, the smaller target nucleus punches a hole through the larger projectile nucleus, removing several nucleons in a near instantaneous time step. The removal of nucleons imparts an excitation energy to the residual nucleus. In the ablation step the projectile residual will evaporate nucleons and emit gamma radiation until it reaches a particle bound state.

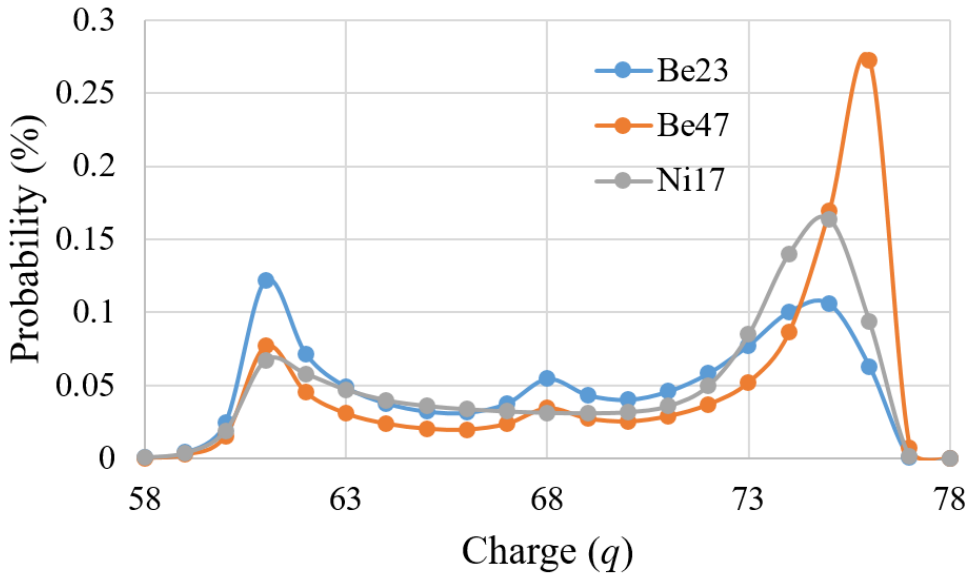

Figure 5.8: ETACHA4v3 was used to calculate the probability of the fragmentation reaction occurring in every possible primary beam charge state while in the production target. Values are calculated for the three targets used in the NSCL experiment: 47 mg/cm^2 Be, 23 mg/cm^2 Be, and 17.8 mg/cm^2 Ni.

The ablation step is relatively short lived, and the prefragment will evaporate to the final fragment before the projectile residual exits the target. This model does not consider or predict the behavior of the electrons bound to the projectile.

The default settings in LISE^{++} produce projectile fragments that are fully stripped of all primary beam electrons immediately after reaction ($Ne_R = 0$). This standard assumption was questioned, and an investigation into the probability of electron shake-off in a nuclear reaction was explored. A recent publication [89] generalizes the electron shake-off probability for any number of proton removal by calculating the overlap of electron orbital wave functions for the initial nucleus bound state and the final nucleus continuum state. This calculation was parameterized by the ratio $\gamma = Z'/Z$, where Z and Z' are the proton numbers for the initial and final nucleus, respectively. In the NSCL experiment, γ ranged between 1 and 0.91. This corresponds to a probability of less than 1% to lose electrons in the 1s, 2s, and 3s electron shells. The wave function overlap methodology also predicted that for a fixed principal quantum number, the electron shake-off probability decreases with increasing angular momentum quantum numbers. These predictions indicate that the electrons from the primary beam will play a significant role in the charge state distributions of fragments exiting a thin target.

The impact of primary beam electrons on the charge state distributions of fragments exiting the target was probed by exploring a newly defined parameter: the number of electrons bound to the projectile residual immediately after interaction, or Ne_R . The implementation of this methodology was described in Section 3.4, the dependence of Ne_R on ΔZ was presented in Section 4.3, and an argument for the value of this method will be made here in two main points: (i) the enumeration of all physical possibilities via Monte Carlo simulations contains less assumptions than analytical codes, and (ii) Ne_R provides an insight into the reaction mechanism.

The calculation of modified charge state fractions by way of Monte Carlo simulation removes the standard assumption that a projectile fragment is formed fully stripped after a reaction. Additionally, due to the probabilistic nature of enumerating all possible scenarios, there is a justified normalization of charge state fractions. This is an improvement compared to the standard analysis briefly discussed

at the beginning of this section. After aligning all charge states in Figure 5.6, there was no accurate method for a final normalization step nor a quantification of error. This is the fundamental ambiguity of standard charge state analysis that was addressed with the Monte Carlo method.

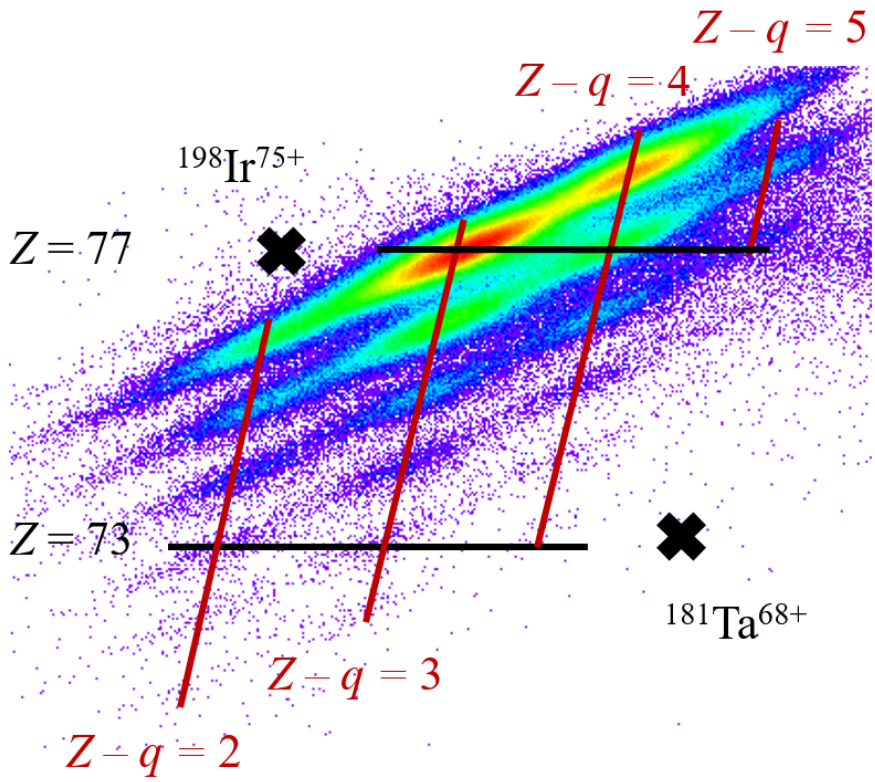

Figure 5.9: A PID spectra from data set D3b (see Table 2.1) with no calibration and no cleaning. Proton number, Z, is on the y-axis and charge state is $Z - q$ on the x-axis. A trend between Z and $Z - q$ is indicated with the red and black lines. Lower lying Z has lower lying charge states. Charge state $Z - q = 5$ only extends down to $Z = 77$, and iridium isotopes only extend to the $Z - q = 4$ charge state. Two ions predicted to be well within the acceptance of the separator, $^{198}Ir^{75+}$ and $^{181}Ta^{69+}$, are not present in the PID spectra. The missing ion group positions are indicated by a black X. Figure 5.10 shows the predicted particle distribution of each ion on the detector.

The physical relationship between Ne_R and ΔZ presented in Section 4.3 potentially provides a new experimental observable for the fragmentation reaction. This relationship was strong enough that it was observed in the PID patterns of experimental data before calibration and before cleaning (see Figure 5.9). The PID spectra exhibited a clear relationship between Ne_R and ΔZ, even to the naked eye. This pattern was further confirmed by inspecting spatial distributions of ^{181}Ta ions with the LISE^{++} program. The $Z - q = 5$ charge state was clearly within the acceptance of the fragment

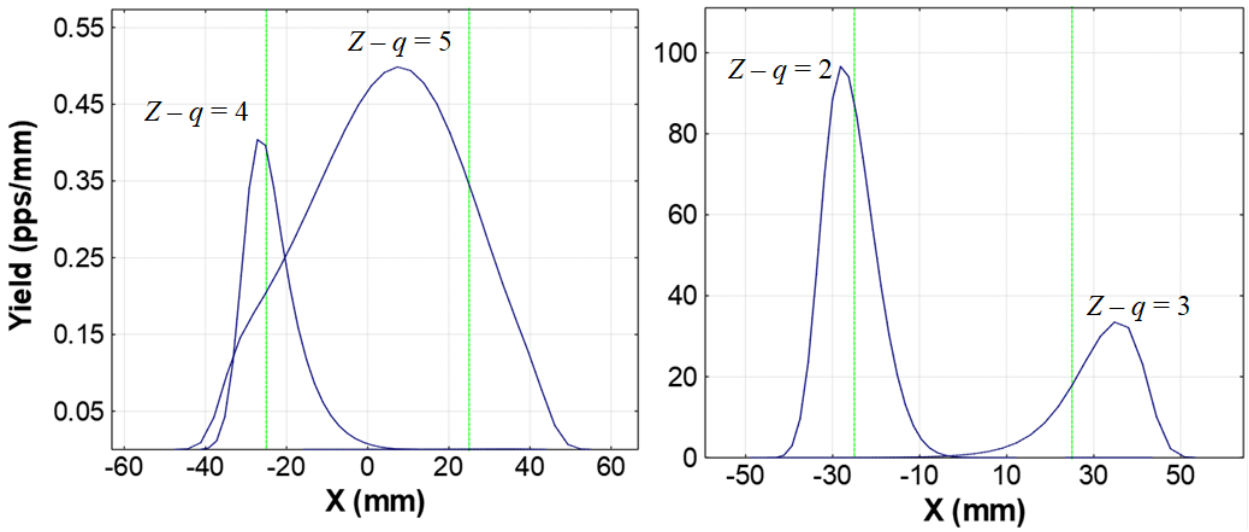

Figure 5.10: LISE^{++} was use to calculate particle distributions of Ta and Ir ions at the detector position (see Fig. 2.1) for the D3b settings (see Table 2.1). Two ^{181}Ta ions, are shown on the left, $Z-q=5$ and $Z-q=4$. Two ^{198}Ir ions are shown on the right, $Z-q=2$ and $Z-q=3$. The green vertical line represent the extent of the slit width. He-like ^{198}Ir and B-like ^{181}Ta are well within the acceptance of the separator, but are absent in the PID of Figure 5.9

separator at both momentum selection slits (see Figure 5.10). However, no instances of this charge state were observed in experiment. This indicates the pattern in Figure 5.9 is not an illusion created from the ion optics settings of the fragment separator. It is interesting to note that such a pattern may be even more noticeable in proton rich nuclei. The cross section of proton removal would be considerably higher than for neutron-rich nuclei, and the Ne_R vs ΔZ trend may even be more visible.

The Monte Carlo enumeration of Ne_R also has its limitations, as the method relies on very little change to the charge of an ion after it is created. Therefore, if the production target is thick, or if there is a significant amount of material in the beam path after the target, the charge state information related to the reaction will be erased upon repeated ionization and electron pickup. This effect was highlighted in Figure 4.8, where the Ne_R vs ΔZ trend was washed out for the 47 mg/cm^2 target.

While not a critique on the method itself, it is important to remember that an underlying charge state model was used to calculate the Monte Carlo charge state distributions. Specifically, GLOBAL in Non-Equilibrium mode was used, which was shown to perform less accurately than ETACHA4v3

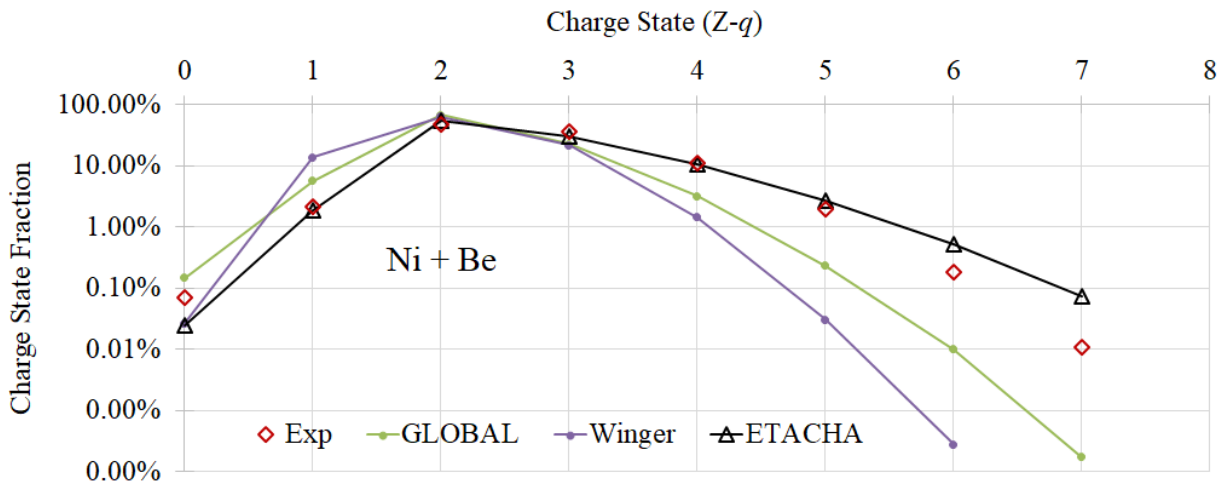

Figure 5.11: Charge state distribution of the primary beam, $^{198}Pt^{61+}$, exiting the Ni target + Be stripper setup. Experimental data is shown with red diamonds, ETACHA4.v3 [78] is shown in black triangles, `GLOBAL` [77] is shown in green, and Winger [90] is shown in purple.

in the charge state study of the primary beam (see Fig. 5.11). However, scripting `ETACHA` for extended calculation was avoided due to the time cost of development. A possible upgrade for this method could be utilizing the closest matching charge state model for the underlying calculations rather than using what is fast.

Despite improvements to the accuracy of charge state fraction predictions, the error of the charge state model was uncertain. The probability weighted average of all possible outcomes of Ne_R helped reduce reliance on the charge state model. Each weight was defined by the optimization of physical parameters, which were defined by the experimental data. This resulted in a correct estimate of the most likely mean value for the charge state fraction and supplied an error estimate based on the available data. However, each Monte Carlo calculation still utilized the `GLOBAL` charge state model to define its underlying probability distributions. These model based predictions, which do not contain clearly defined uncertainties, were reduced in the novel charge state analysis but were not completely eliminated. Examples of this behavior can be seen in Figure 5.2 for rhenium, $Z = 75$, where a charge-related inconsistency can still be observed in the final data.

Further improvements to this charge state analysis method should be considered, and one such improvement is discussed here. Rather than defining each possible scenario by Ne_R, a new

parameter equal to the number of electrons removed during reaction, ΔN_e, would be a more suitable parameter for Monte Carlo calculations. As seen in Figure 5.8, the fragmentation reaction may occur in several different charge states of the primary beam. The most probable charge state for the thin Be target was $Z - q = 3$. If $N\mathrm{e}_R$ is set to a value of five, it is implied that the projectile fragment is picking up two electrons during fragmentation. The pickup of two electrons from beryllium is technically possible. However, when this situation is extrapolated to $Z - q = 0$ and $N\mathrm{e}_R = 5$, a five-electron pick-up is implied, which is greater than the number of electrons bound to a Be atom. Exploring the newly proposed ΔN_e parameter would eliminate such issues as long as a simple conditional was included to prevent $\Delta N_e > Z - q$, another non-physical scenario. To go a step further, the probabilities of electron shake-off due to the sudden removal of protons could be calculated and then included in the Monte Carlo code to further increase the accuracy of such calculations.

Chapter 6

Conclusion

Fragmentation of a ^{198}Pt beam was explored at 85 MeV/u and 186 MeV/u, and both instances resulted in the discovery of new isotopes. This is the first progress toward reaching the neutron dripline in this region in over a decade. The cross sections of fragmentation products for both beryllium and nickel targets were measured, and noticeably larger cross sections were observed for the nickel target. The experimental data was most accurately reproduced by the `ABRABLA07` and `LISEAA` models. A novel charge state analysis was developed and applied to the charge state distributions of materials below equilibrium thickness. Probability distributions for the newly considered Ne_R parameter were generated from Monte Carlo calculations, and a relationship between the number of protons removed and Ne_R was observed. Greater proton removal corresponded to less electrons remaining on the projectile residual, and this relationship has the potential to provide additional insight into the fragmentation reaction upon further study.

Future studies of heavy isotope production will be necessary. This can be accomplished by focusing on increasing primary beam intensity, studying the details of all reaction mechanisms at play, and accurately modeling the charge state and trajectory of ions as they pass through materials in a fragment separator. An improved, or entirely new, model for the fragmentation reaction is one of the most urgent issues needed to keep up with the increasing reach of next generation facilities and their ability to produce exotic nuclei at exceedingly small cross sections. Each one of these points will be briefly discussed in this chapter, and the final section will offer a few perspectives regarding the future of rare isotope production.

6.1 Summary

Two medium energy fragmentation experiments of ^{198}Pt were performed at two distinct energies, 85 MeV/u and 186 MeV/u. The fragmentation of 85 MeV/u ^{198}Pt on Be and Ni targets was executed at the NSCL with the coupled cyclotron accelerators and the A1900 fragment separator [59]. The PID was performed using the ΔE-*TKE*-*ToF*-$B\rho$ method, where the majority of detectors were located at the end of the S800 analysis beam line [60]. The fragmentation of 186 MeV/u ^{198}Pt on a carbon target was executed at FRIB using a linear accelerator and ARIS [26, 67]. The fragment separator was utilized as the analysis line, and all PID detectors were contained in the C-Bend.

The products from both experiments were identified using the same ΔE-*TKE*-*ToF*-$B\rho$ method, and cross sections were measured for the NSCL data. The cross section for each ion detected in the NSCL experiment was calculated using the yield of the ion, the total number of beam particles, the particle density of the target, and the transmission fraction of ions that made it from the target to the PID detectors. The asymmetric errors of transmission values were preserved in most conservative manner: by direct calculation of upper and lower limits of the cross section. Multiple cross section measurements of the same isotope across multiple charge states and experimental runs were averaged together by the analytic AEWA method describe in Section 3.3. The fractions of charge state distributions were modified for the Be target data using a novel Monte Carlo calculation method. The cross sections for Ni target data were calculated without any modifications to the charge state fractions. Calculations for both the Be and Ni target data used the charge state model `GLOBAL`.

Successful event-by-event particle identification and the discovery of new isotopes was carried out in both experiments. The separation of charge states was achieved in both experiments with an increase in A/q resolution by a factor of five from the NSCL experiment to the FRIB experiment. ^{191,192}Hf and ^{189}Lu were discovered in the NSCL experiment, and ^{190}Lu, ^{186,187}Yb, and ^{182,183}Tm were discovered in the FRIB experiment. Pick-up reactions were observed in both experiments.

The cross sections for 72 nuclides produced in the ^{198}Pt + Be reaction and 50 nuclides produced

in the ^{198}Pt + Ni reaction were measured in the NSCL experiment. In addition, the first known evidence of electrons on the projectile residual immediately after reaction (Ne_R) was observed. The PDFs generated during the novel Monte Carlo charge state analysis exhibited evidence of a trend between the number of protons removed (ΔZ) and Ne_R. For the first time, it was observed that as ΔZ increased, Ne_R decreased. This trend was more evident for the thinner of the two beryllium targets. The Ni target cross sections were, on average, an order of magnitude larger than the Be cross sections. However, these results have large uncertainty due to multiple contributions of transmission errors (see Section 5.2).

The new territory claimed by these experiments can be used for future studies on nuclear structure and reactions. Several nuclear structure studies exploring the shape evolution of even-even nuclei can be expanded with the isotopes produced by ^{198}Pt fragmentation [84, 43]. The experimental basis for fragmentation reaction models can also be expanded upon with momentum distribution measurements of these rare isotopes.

A comparison of `EPAX3` , `COFRA` , `ABRABLA07` , and `LISEAA` was performed within the region explored in this study [15, 32, 46, 85]. `COFRA` performs well for the removal of relatively few protons, whereas `EPAX3` underestimates for high-Z elements and overestimates for low-Z elements. `ABRABLA07` reproduced experimental data relatively well across the entire range of the experiment, highlighting the importance of the de-excitation step in the abrasion-ablation model. However, there was a noticeable difference in the cross section slope for a given element as a function of isotopic mass. The `LISEAA` model, when used with a parametrized Gaussian distribution for the excitation energy, was optimized to best fit the experimental data. This was quantitatively demonstrated with an error-weighted log-residual calculation.

The novel Monte Carlo method for charge state analysis was motivated by the need to reduce uncertainties on the charge state model. The consideration of Ne_R as an experimentally relevant parameter is justified based on the low probability of shaking off electrons during a sudden removal of protons. An enumeration of all the possible values for Ne_R led to the least possible reliance on the charge state model. Additionally, the PDFs associated with Ne_R provide an insight into

the intensity of the reaction mechanism, exhibiting a relationship between ΔZ and Ne_R . This relationship is strong enough to be visible in PID spectra. On the other hand, the novel method of charge state analysis presented in this work crucially depends on the Ne_R parameter. Information of Ne_R is only experimentally detectable with thin production targets and few materials in the beam path.

6.2 Outlook

The results presented in this work should be expanded upon by pursuing three separate directions of exploration: (i) increased beam intensity, (ii) reaction mechanism focused experiments, and (iii) charge states evolution of ions in materials. Increased beam intensity experiments should focus on pushing the boundary of discovery further while collecting fundamental information about these new isotopes, such as beta-decay half-lives. Reaction mechanism focused studies should reconsider the role of excitation energy in leading models and make efforts to include more physical observables in the models. The charge state evolution of ions passing through multiple materials in a fragment separator should be more precisely described by optimizing existing models to large scale data sets of secondary beam yields with multiple charge states.

Increased beam intensity will help establish a foothold of understanding in the neutron-rich region near $N = 126$. This understanding begins with the identification of new isotopes. Limiting our consideration to the neutron-rich region between $104 \leq N \leq 131$, the production of over 109 new isotopes are predicted to be possible at 400 kW of beam power and optimal optics using the $k = 3$ setting of ARIS [26]. All 109 of these isotopes are shown in Figure 6.1, alongside the new isotopes presented in this work. The cross sections of each new isotope, including the five discovered in the FRIB experiment of this work, should be measured. Other fundamental properties of nuclei, such as mass, half-life, and charge radius, should also be measured. FRIB is equipped with the LEBIT [91], FDSi [92], and BECOLA [93] projects to perform such tasks.

Reaction mechanism studies are also essential for pushing further into the unknown. Several

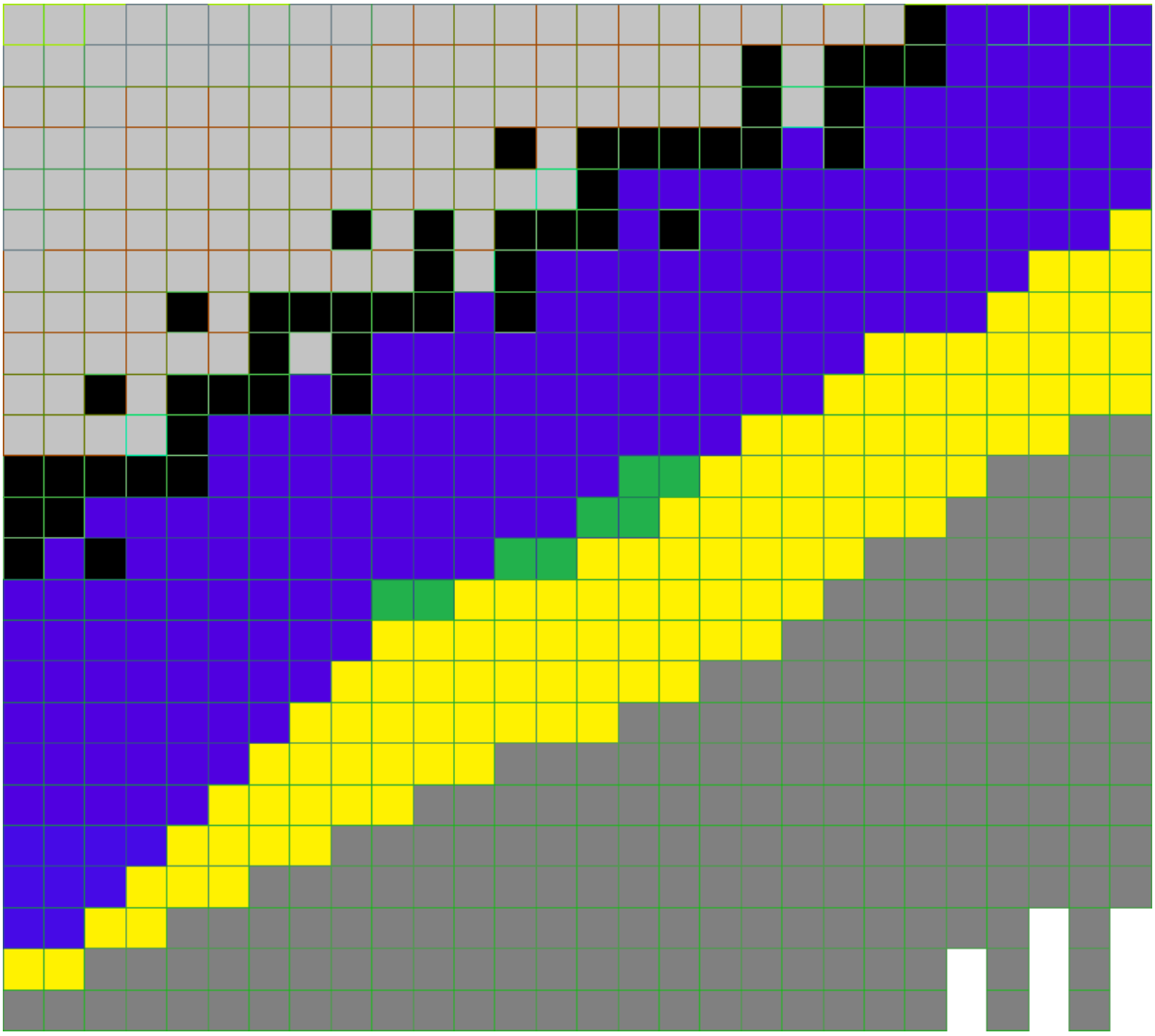

Figure 6.1: The neutron-rich region between $104 \leq N \leq 131$ as presented in Section 1.3, now highlighting the discovery capabilities of FRIB at 400 kW. The new isotopes discovered in this work are shown in green, and new isotope discoveries possible at the 400 kW setting at FRIB are shown in yellow. These estimates were made assuming a rate of roughly 1e-5 pps was necessary to detect a new isotope. Isotopes still out of reach are shown in dark grey and the dripline can be seen on the bottom right in white, indicating unbound nuclei.

directions include: considering new mechanisms that come into play at low cross sections, revising fragmentation models to be accurately tested in an experiment, and exploring new observables related to the details of the nuclear reaction. The increasingly high primary beam rates available at next-generation facilities can probe reactions with much smaller cross sections than fragmentation [26]. For example, the pick-up of several nucleons is significantly lower than the fragmentation

of several nucleons, however pick-up reactions were still observed in this work and could be used to deliver RI beams to the "right" of neutron-rich primary beams. Another contribution to production that is not normally significant, unless to act as a contaminant, is secondary reactions [94]. However, now that beams can be provided at high energies and high intensities, the production target can be made very thick, increasing the cross section of fragmentation for the primary beam and the fragments themselves. A key future advancement will be FRIB400, that may provide ten times more reach [26].

Fragmentation models rely heavily on excitation energy, a quantity that cannot be experimentally measured [32, 46, 85]. This is a major weakness of the theoretical framework surrounding fragmentation and should be reconsidered to create a stronger link between experiment and theory. This can be done in either one of two ways: (i) develop experimental techniques to measure the excitation energy of projectile fragments immediately after reaction, or (ii) restructure theoretical models to include more physical observables that directly relate to the excitation energy. The latter of these two methods could be developed by considering the relationship between the Ne_R parameter and excitation energy. This would add an extra physical observable, alongside momentum distributions, that could potentially lead to a more accurate description of the nuclear reaction.

The charge state evolution of ions passing through multiple materials in a fragment separator is a valuable direction of research for furthering our understanding of heavy-ion fragmentation at intermediate energies. At intermediate energies, heavy-ion fragments will come in several charge states for a given isotope [25]. In order to efficiently use the wealth of information produced in these experiments, it is crucial to understand the behavior of charge state fractions above just He-like, H-like, and fully-stripped ions. Accurate measurements of fractions above $Z - q = 2$ can be performed if the momentum acceptance of the fragment separator is increased to the point where multiple charge states are transmitted for each isotope. The experiments presented in this work had, at most, two ions for a given isotope. Often times, one of those ions was on the edge of the acceptance of the separator leading to a very uncertain transmission. The data set was too limited to paint a complete picture of the complexity of all charge states involved, and a larger data

set should be collected.

Ultra-thin target experiments are well suited for studying charge state distributions of heavy-ions at intermediate energies. With less material, the charge state distributions do not reach equilibrium and a greater number of charge states are experimentally observable [25]. This can be paired with a large acceptance fragment separator to create very large data sets, rich with charge state information. While such an outcome may have traditionally been undesirable due to the difficulty of separating charge states, the progress in high resolution spectrometers and particle identification allows for unequivocal charge state separation, which should be used advantageously.

Thin materials will also preserve charge state information related to the Ne_R parameter. The results of this work included the first known evidence of a relationship between Ne_R and ΔZ of heavy-ion projectile fragments. This relationship should be further studied in a more comprehensive experiment using a very thin target and few materials in the beam line. Such an experimental design would create the least possible disturbance to the Ne_R parameter, and would provide a crucial confirmation of the relationship between Ne_R and ΔZ. Performing this experiment with proton-rich nuclei should also be considered because the proton removal cross section will be much higher, providing a larger range of ΔZ to explore.

6.3 Perspectives

While there remains a considerable number of new isotopes to be discovered with projectile fragmentation, the reach of this nuclear reaction is fundamentally limited by exponentially decreasing cross sections away from stability [25, 47]. Projectile fragmentation will most likely continue to see widespread use, well into the future, as the convenience of in-flight separation is truly unrivaled by any other means of RI production [50]. However, projectile fragmentation cannot be the answer for exhaustively exploring the neutron dripline all the way up to the heaviest elements.

There is ample opportunity for fragmentation to be used as a tool for producing RI beams, and it will most likely dominate nuclear physics in the next couple decades. A wide variety of rare

isotopes can be delivered in steady beams at a desired purity and rate, without needing chemical extraction from the production target [17]. With increasing upgrades to the intensity of primary beams [26], the rates of secondary fragments will increase and more new isotopes will most likely be discovered. As the capabilities of new RI beam facilities are fully realized, accelerator technology and fragment separation will likely see growth as well. Furthermore, even after new isotopes are exhausted there still remains a wide variety of nuclear properties to be measured and studied for each and every nuclide.

On the other hand, exponentially decreasing fragmentation cross sections necessitate a new reaction mechanism for the long term development of rare isotope production toward the neutron drip-line of heavy isotopes [47]. In this work, the cross section for pure proton removal decreased by roughly two orders of magnitude with each proton removed. Improvements made to primary beam intensities will quickly be used up, and the boundary of discovery will still remain far from the dripline. This is shown in Figure 6.1 where the dripline for elements around $Z = 60$ is still more than 20 neutrons away. Therefore, in order to reach the neutron dripline up to $N = 126$ and beyond, other strategies beyond single step fragmentation will be required. For example, the pick-up reactions observed in this work present a potential candidate. While the cross sections of pick-up products are small compared to neighboring fragmentation products, they could offer a viable alternative to the production of increasingly exotic neutron-rich fragments where fragmentation cross sections diminish exponentially with pure proton removal. In these cases, heavy neutron-rich targets, such as nickel, would offer the excess neutrons to facilitate this strategy.

Ultimately, whether new strategies involve the use of multi-nucleon transfer, secondary reactions in thick targets, or an altogether new reaction that dominates at small cross sections, is yet to be discovered. This work represents a step into the terra incognita. Like the explorations of old, our ship has sailed, and we are on the way. There is a long voyage ahead with multiple discoveries likely.

References

[1] R Casten and Nazarewic W. Ria physics white paper, 2000. Accessed: July 9, 2024.

[2] John D Cockcroft and Ernest Thomas Sinton Walton. Disintegration of lithium by swift protons. *Nature*, 129(3261):649–649, 1932.

[3] John J. Cowan, Christopher Sneden, James E. Lawler, Ani Aprahamian, Michael Wiescher, Karlheinz Langanke, Gabriel Martínez-Pinedo, and Friedrich-Karl Thielemann. Origin of the heaviest elements: The rapid neutron-capture process. *Rev. Mod. Phys.*, 93:015002, Feb 2021.

[4] H. Alvarez-Pol, J. Benlliure, E. Casarejos, et al. Production of new neutron-rich isotopes of heavy elements in fragmentation reactions of ^{238}U projectiles at 1a gev. *Phys. Rev. C*, 82:041602, Oct 2010.

[5] J. Kurcewicz, F. Farinon, H. Geissel, et al. Discovery and cross-section measurement of neutron-rich isotopes in the element range from neodymium to platinum with the frs. *Physics Letters B*, 717(4):371–375, 2012.

[6] O. B. Tarasov, D. Bazin, M. Hausmann, M. P. Kuchera, P. N. Ostroumov, M. Portillo, B. M. Sherrill, K. V. Tarasova, and T. Zhang. Lise cute++, the latest generation of the lise ++ package, to simulate rare isotope production with fragment-separators. *Nuclear Instruments and Methods in Physics Research B*, 541:4–7, 2023.

[7] M Kortelainen, J McDonnell, Witold Nazarewicz, P-G Reinhard, J Sarich, N Schunck, MV Stoitsov, and SM Wild. Nuclear energy density optimization: Large deformations. *Physical Review C*, 85(2):024304, 2012.

[8] National Nuclear Data Center. Information extracted from the nudat database. `https://www.nndc.bnl.gov/nudat/`. Accessed: 2024-06-13.

[9] M. Thoennessen. *The Discovery of Nuclides*, page 5. Springer Cham, 2016.

[10] F.G. Kondev, M. Wang, W.J. Huang, S. Naimi, and G. Audi. The nubase2020 evaluation of nuclear physics properties *. *Chinese Physics C*, 45(3):030001, mar 2021.

[11] Meng Wang, Wen Jie Huang, Filip G Kondev, Georges Audi, and Sarah Naimi. The ame 2020 atomic mass evaluation (ii). tables, graphs and references. *Chinese Physics C*, 45(3):030003, 2021.

[12] D. S. Ahn, N. Fukuda, et al. Location of the neutron dripline at fluorine and neon. *Phys. Rev. Lett.*, 123:212501, Nov 2019.

[13] Hans Geissel, P Armbruster, KH Behr, A Brünle, K Burkard, M Chen, H Folger, B Franczak, H Keller, O Klepper, et al. The gsi projectile fragment separator (frs): a versatile magnetic system for relativistic heavy ions. *Nuclear Instruments and Methods in Physics Research Section B: Beam Interactions with Materials and Atoms*, 70(1-4):286–297, 1992.

[14] B.M. Sherrill, D.J. Morrissey, J.A. Nolen, and J.A. Winger. The a1200 projectile fragment separator. *Nuclear Instruments and Methods in Physics Research Section B: Beam Interactions with Materials and Atoms*, 56-57:1106–1110, 1991.

[15] K. Summerer. Improved empirical parametrization of fragmentation cross sections. *Phys. Rev. C*, 86:014601, Jul 2012.

[16] O. B. Tarasov and D. Bazin. Lise^{++}: Exotic beam production with fragment separators and their design. *Nuclear Instruments and Methods in Physics Research B*, 376:185–187, 2016.

[17] DF Geesaman, CK Gelbke, RVF Janssens, and BM Sherrill. Physics of a rare isotope accelerator. *Annu. Rev. Nucl. Part. Sci.*, 56(1):53–92, 2006.

[18] T. Yamaguchi, H. Koura, Yu.A. Litvinov, and M. Wang. Masses of exotic nuclei. *Progress in Particle and Nuclear Physics*, 120:103882, 2021.

[19] I. Angeli and K.P. Marinova. Table of experimental nuclear ground state charge radii: An update. *Atomic Data and Nuclear Data Tables*, 99(1):69–95, 2013.

[20] I. Hadjas, P. Ascough, M.H. Garnett, et al. Radiocarbon dating. *Nature Reviews Methods Primers*, 1(1):62, 2021.

[21] D. Bardayan. Recent experimental progress in nuclear astrophysics. *Physics Procedia*, 66:457–464, 12 2015.

[22] Bradley S Meyer. The r-, s-, and p-processes in nucleosynthesis. *Annual Review Astronomy and Astrophysics*, 32(NAS 1.26: 204924), 1994.

[23] O. B. Tarasov, O. Delaune, F. Farget, D. J. Morrissey, et al. Fission fragment yields from heavy-ion-induced reactions measured with a fragment separator. *The European Physical Journal A*, 54(4):66, Apr 2018.

[24] H. M. Devaraja, S. Heinz, D. Ackermann, T. Göbel, F. P. Heßberger, S. Hofmann, J. Maurer, G. Münzenberg, A. G. Popeko, and A. V. Yeremin. New studies and a short review of heavy neutron-rich transfer products. *The European Physical Journal A*, 56(9):224, 2020.

[25] K. Haak, O. B. Tarasov, P. Chowdhury, A. M. Rogers, K. Sharma, et al. Production and discovery of neutron-rich isotopes by fragmentation of ^{198}Pt. *Phys. Rev. C*, 108:034608, Sep 2023.

[26] J. Wei et al. Accelerator commissioning and rare isotope identification at the facility for rare isotope beams. *Modern Physics Letters A*, 37(09):2230006, 2022.

[27] P.-A. Söderström, J. Nyberg, P. H. Regan, et al. Spectroscopy of neutron-rich ^{168,170}Dy: Yrast band evolution close to the N_pN_n valence maximum. *Phys. Rev. C*, 81:034310, Mar 2010.

[28] K. Rykaczewski, K.-L. Gippert, N. Kaffrell, et al. Investigation of neutron-rich rare-earth nuclei including the new isotopes 177tm and 184lu. *Nuclear Physics A*, 499(3):529–545, 1989.

[29] T. Kubo, M. Ishihara, N. Inabe, et al. The riken radioactive beam facility. *Nuclear Instruments and Methods in Physics Research Section B: Beam Interactions with Materials and Atoms*, 70(1):309–319, 1992.

[30] R. Anne, D. Bazin, A.C. Mueller, J.C. Jacmart, and M. Langevin. The achromatic spectrometer lise at ganil. *Nuclear Instruments and Methods in Physics Research Section A: Accelerators, Spectrometers, Detectors and Associated Equipment*, 257(2):215–232, 1987.

[31] M. Pfützner, P. Armbruster, T. Baumann, et al. New isotopes and isomers produced by the fragmentation of 238u at 1000 mev/nucleon. *Physics Letters B*, 444(1):32–37, 1998.

[32] J. Benlliure, K. H. Schmidt, D. Cortina-Gil, T. Enqvist, F. Farget, A. Heinz, A. R. Junghans, J. Pereira, and J. Taieb. Production of neutron-rich isotopes by cold fragmentation in the reaction ^{197}Au + Be at 950 A MeV. *Nucl. Phys. A*, 660:87–100, 1999. [Erratum: Nucl.Phys.A 674, 578–578 (2000)].

[33] K. Sümmerer, W. Brüchle, D. J. Morrissey, M. Schädel, B. Szweryn, and Yang Weifan. Target fragmentation of au and th by 2.6 gev protons. *Phys. Rev. C*, 42:2546–2561, Dec 1990.

[34] F Marti, P Miller, D Poe, M Steiner, J Stetson, and XY Wu. Commissioning of the coupled cyclotron system at nscl. In *AIP Conference Proceedings*, volume 600, pages 64–68. American Institute of Physics, 2001.

[35] H. Okuno, T. Dantsuka, M. Fujimaki, et al. Present status of and recent developments at riken ri beam factory. *Journal of Physics: Conference Series*, 1401(1):012005, jan 2020.

[36] T. Ohnishi, T. Kubo, K. Kusaka, et al. Identification of new isotopes 125pd and 126pd produced by in-flight fission of 345 mev/nucleon 238u: First results from the riken ri beam factory. *Journal of the Physical Society of Japan*, 77(8):083201, 2008.

[37] O. B. Tarasov, D. S. Ahn, et al. Discovery of ^{60}Ca and implications for the stability of ^{70}Ca. *Phys. Rev. Lett.*, 121:022501, Jul 2018.

[38] O. B. Tarasov, M. Portillo, et al. Production of very neutron-rich nuclei with a ^{76}Ge beam. *Phys. Rev. C*, 80:034609, Sep 2009.

[39] O. B. Tarasov, M. Portillo, D. J. Morrissey, et al. Production cross sections from ^{82}se fragmentation as indications of shell effects in neutron-rich isotopes close to the drip-line. *Phys. Rev. C*, 87:054612, May 2013.

[40] H Suzuki, T Kubo, N Fukuda, N Inabe, D Kameda, H Takeda, K Yoshida, K Kusaka, Y Yanagisawa, M Ohtake, et al. Discovery of new isotopes mo 81, 82 and ru 85, 86 and a determination of the particle instability of 103 sb. *Physical Review C*, 96(3):034604, 2017.

[41] P. N. Ostroumov, O. B. Tarasov, et al. Acceleration of uranium beam to record power of 10.4 kw and observation of new isotopes at facility for rare isotope beams. *Phys. Rev. Accel. Beams*, 27:060101, Jun 2024.

[42] T. Kurtukian-Nieto, J. Benlliure, K.-H. Schmidt, L. Audouin, F. Becker, B. Blank, E. Casarejos, F. Farget, M. Fernández-Ordóñez, J. Giovinazzo, D. Henzlova, B. Jurado, J. Pereira, and O. Yordanov. Production cross sections of heavy neutron-rich nuclei approaching the nucleosynthesis r-process path around $a = 195$. *Phys. Rev. C*, 89:024616, Feb 2014.

[43] N. Alkhomashi, P. H. Regan, Zs. Podolyák, S. Pietri, A. B. Garnsworthy, S. J. Steer, et al. β^--delayed spectroscopy of neutron-rich tantalum nuclei: Shape evolution in neutron-rich tungsten isotopes. *Phys. Rev. C*, 80:064308, Dec 2009.

[44] S. J. Steer, Zs. Podolyák, S. Pietri, M. Górska, H. Grawe, K. H. Maier, P. H. Regan, D. Rudolph, A. B. Garnsworthy, R. Hoischen, J. Gerl, H. J. Wollersheim, et al. Isomeric states observed in heavy neutron-rich nuclei populated in the fragmentation of a ^{208}pb beam. *Phys. Rev. C*, 84:044313, Oct 2011.

[45] A. I. Morales, J. Benlliure, J. Agramunt, et al. Synthesis of $n = 127$ isotones through (p,n) charge-exchange reactions induced by relativistic ^{208}pb projectiles. *Phys. Rev. C*, 84:011601, Jul 2011.

[46] Aleksandra Kelic, M. Valentina Ricciardi, and Karl-Heinz Schmidt. ABLA07 - towards a complete description of the decay channels of a nuclear system from spontaneous fission to multifragmentation. In *Joint ICTP-IAEA Advanced Workshop on Model Codes for Spallation Reactions*. IAEA INDC, June 2009. arXiv:0906.4193 [nucl-th].

[47] T. Kurtukian-Nieto, J. Benlliure, Schmidt, et al. Production cross sections of heavy neutron-rich nuclei approaching the nucleosynthesis r-process path around $a = 195$. *Phys. Rev. C*, 89:024616, Feb 2014.

[48] Valery Zagrebaev and Walter Greiner. Production of new heavy isotopes in low-energy multinucleon transfer reactions. *Physical review letters*, 101(12):122701, 2008.

[49] EM Kozulin, Emanuele Vardaci, GN Knyazheva, AA Bogachev, SN Dmitriev, IM Itkis, MG Itkis, AG Knyazev, TA Loktev, KV Novikov, et al. Mass distributions of the system 136 xe+ 208 pb at laboratory energies around the coulomb barrier: a candidate reaction for the production of neutron-rich nuclei at n= 126. *Physical Review C*, 86(4):044611, 2012.

[50] O. Beliuskina, S. Heinz, V. Zagrebaev, V. Comas, C. Heinz, S. Hofmann, R. Knöbel, M. Stahl, D. Ackermann, F. P. Heßberger, B. Kindler, B. Lommel, J. Maurer, and R. Mann. On the synthesis of neutron-rich isotopes along the n = 126 shell in multinucleon transfer reactions. *The European Physical Journal A*, 50(10):161, Oct 2014.

[51] JS Barrett, W Loveland, R Yanez, Shaofei Zhu, AD Ayangeakaa, MP Carpenter, JP Greene, RVF Janssens, T Lauritsen, EA McCutchan, et al. Xe 136+ pb 208 reaction: A test of models of multinucleon transfer reactions. *Physical Review C*, 91(6):064615, 2015.

[52] Y. X. Watanabe, Y. H. Kim, S. C. Jeong, and other. Pathway for the production of neutron-rich isotopes around the $n = 126$ shell closure. *Phys. Rev. Lett.*, 115:172503, Oct 2015.

[53] G. Savard, M. Brodeur, J.A. Clark, R.A. Knaack, and A.A. Valverde. The n=126 factory: A new facility to produce very heavy neutron-rich isotopes. *Nuclear Instruments and Methods in Physics Research Section B: Beam Interactions with Materials and Atoms*, 463:258–261, 2020.

[54] Julia Even, Xiangcheng Chen, Arif Soylu, et al. The next project: Towards production and investigation of neutron-rich heavy nuclides. *Atoms*, 10(2), 2022.

[55] T. Niwase, Y. X. Watanabe, Y. Hirayama, et al. Discovery of new isotope ^{241}U and systematic high-precision atomic mass measurements of neutron-rich pa-pu nuclei produced via multinucleon transfer reactions. *Phys. Rev. Lett.*, 130:132502, Mar 2023.

[56] V. V. Desai, A. Pica, W. Loveland, J. S. Barrett, E. A. McCutchan, S. Zhu, A. D. Ayangeakaa, M. P. Carpenter, J. P. Greene, T. Lauritsen, R. V. F. Janssens, B. M. S. Amro, and W. B. Walters. Multinucleon transfer in the interaction of 977 mev and 1143 mev ^{204}Hg with ^{208}Pb. *Phys. Rev. C*, 101:034612, Mar 2020.

[57] VI Zagrebaev. Synthesis of superheavy nuclei: Nucleon collectivization as a mechanism for compound nucleus formation. *Physical Review C*, 64(3):034606, 2001.

[58] O. B. Tarasov, A. Gade, et al. Observation of new isotopes in the fragmentation of ^{198}Pt at frib. *Phys. Rev. Lett.*, 132:072501, Feb 2024.

[59] D.J. Morrissey, B.M. Sherrill, M. Steiner, A. Stolz, and I. Wiedenhoever. Commissioning the a1900 projectile fragment separator. *Nuclear Instruments and Methods in Physics Research B*, 204:90–96, 2003.

[60] D. Bazin, J.A. Caggiano, B.M. Sherrill, J. Yurkon, and A. Zeller. The s800 spectrograph. *Nuclear Instruments and Methods in Physics Research B*, 204:629–633, 2003.

[61] S. Paschalis, I.Y. Lee, A.O. Macchiavelli, et al. The performance of the gamma-ray energy tracking in-beam nuclear array gretina. *Nuclear Instruments and Methods in Physics Research A*, 709:44–55, 2013.

[62] Micron Semiconductor Limited. Msx25-140um 2m/2m em grade ceramic package, August 2016.

[63] N. Fukuda, T. Kubo, D. Kameda, et al. Identification of new neutron-rich isotopes in the rare-earth region produced by 345 mev/nucleon 238u. *Journal of the Physical Society of Japan*, 87(1):014202, 2018.

[64] H. Suzuki, K. Yoshida, N. Fukuda, et al. Experimental studies of the two-step scheme with an intense radioactive ^{132}Sn beam for next-generation production of very neutron-rich nuclei. *Phys. Rev. C*, 102:064615, Dec 2020.

[65] Thomas Glasmacher, Bradley Sherrill, Witek Nazarewicz, Alexandra Gade, Paul Mantica, Jie Wei, Georg Bollen, and Brad Bull. Facility for rare isotope beams update for nuclear physics news. *Nuclear Physics News*, 27(2):28–33, 2017.

[66] M. Hausmann et al. Design of the advanced rare isotope separator aris at frib. *Nuclear Instruments and Methods in Physics Research Section B*, 317:349–353, 2013.

[67] M. Portillo, B.M. Sherrill, et al. Commissioning of the advanced rare isotope separator aris at frib. *Nuclear Instruments and Methods in Physics Research Section B: Beam Interactions with Materials and Atoms*, 540:151–157, 2023.

[68] P. N. Ostroumov, K. Fukushima, T. Maruta, A. S. Plastun, J. Wei, T. Zhang, and Q. Zhao. First simultaneous acceleration of multiple charge states of heavy ion beams in a large-scale superconducting linear accelerator. *Phys. Rev. Lett.*, 126:114801, Mar 2021.

[69] Micron Semiconductor Limited. Msx25 (ss) 300, 500, 1000 2m/2m, September 2022.

[70] M. Caamaño, P. M. Walker, P. H. Regan, et al. Isomers in neutron-rich a $\approx$ 190 nuclides from 208pb fragmentation. *The European Physical Journal A - Hadrons and Nuclei*, 23:201–215, 2005.

[71] P. Sigmund. *Dielectric Stopping Theory*, pages 141–180. Springer Berlin Heidelberg, Berlin, Heidelberg, 2006.

[72] Zs. Podolyák, P.H. Regan, M. Pfützner, et al. Isomer spectroscopy of neutron rich 190w116. *Physics Letters B*, 491(3):225–231, 2000.

[73] O. B. Tarasov and D. Bazin. Lise^{++}: Radioactive beam production with in-flight separators. *Nuclear Instruments and Methods in Physics Research B*, 266:4657–4664, 2008. `https://lise.nscl.msu.edu`.

[74] Jens Lindhard and Allan H. So/rensen. Relativistic theory of stopping for heavy ions. *Phys. Rev. A*, 53:2443–2456, Apr 1996.

[75] O. Tarasov. Analysis of momentum distributions of projectile fragmentation products. *Nucl. Phys. A*, 734:536, 2004.

[76] F. Hubert, R. Bimbot, and H. Gauvin. Range and stopping-power tables for 2.5–500 MeV/nucleon heavy ions in solids. *Atom. Data Nucl. Data Tabl.*, 46:1–213, 1990.

[77] C Scheidenberger, Th Stöhlker, W.E Meyerhof, H Geissel, P.H Mokler, and B Blank. Charge states of relativistic heavy ions in matter. *Nuclear Instruments and Methods in Physics Research B*, 142(4):441–462, 1998.

[78] E. Lamour, P. D. Fainstein, M. Galassi, C. Prigent, C. A. Ramirez, R. D. Rivarola, J.-P. Rozet, M. Trassinelli, and D. Vernhet. Extension of charge-state-distribution calculations for ion-solid collisions towards low velocities and many-electron ions. *Phys. Rev. A*, 92:042703, Oct 2015.

[79] H. Suzuki, T. Kubo, N. Fukuda, et al. Discovery of new isotopes ^{81,82}Mo and ^{85,86}Ru and a determination of the particle instability of $^{\mathbf{103}}$**Sb**. *Phys. Rev. C*, 96:034604, Sep 2017.

[80] J. Besprosvany and S. Levit. Limiting temperature and limits of statistical particle emission in hot nuclei. *Physics Letters B*, 217(1):1–4, 1989.

[81] Zhuxia Li and Min Liu. Mass and isotope dependence of limiting temperatures for hot nuclei. *Phys. Rev. C*, 69:034615, Mar 2004.

[82] Mark D Baker, Wan Chang, Markus Diefenthaler, Florian Hauenstein, Or Hen, Douglas Higinbotham, Alex Jentsch, Jeong-Hung Lee, Wenliang Li, Pawel Nadel-Turonski, et al. Generic r&d proposal: Beagle, a tool to refine ir and detector requirements for the eic. Technical report, Jefferson Lab, 2022. Accessed: 2023-07-10.

[83] S. K. Tandel, T. L. Khoo, D. Seweryniak, G. Mukherjee, et al. k isomers in ^{254}No: Probing single-particle energies and pairing strengths in the heaviest nuclei. *Phys. Rev. Lett.*, 97:082502, Aug 2006.

[84] P. D. Stevenson, M. P. Brine, Zs. Podolyak, P. H. Regan, P. M. Walker, and J. Rikovska Stone. Shape evolution in the neutron-rich tungsten region. *Phys. Rev. C*, 72:047303, Oct 2005.

[85] O. B. Tarasov. References therein; LISE^{++} abrasion-ablation web page. `https://lise.nscl.msu.edu/AA`, Michigan State University.

[86] J. Benlliure and K. H. Schmidt. References therein; COFRA web page. `http://www.usc.es/genp/cofra`, Universidade de Santiago de Compostela.

[87] K-H Schmidt, MV Ricciardi, AS Botvina, and T Enqvist. Production of neutron-rich heavy residues and the freeze-out temperature in the fragmentation of relativistic 238u projectiles determined by the isospin thermometer. *Nuclear Physics A*, 710(1-2):157–179, 2002.

[88] L Audirac, A Obertelli, P Doornenbal, Davide Mancusi, Satoshi Takeuchi, Nori Aoi, Hidetada Baba, Simon Boissinot, Alain Boudard, A Corsi, et al. Evaporation-cost dependence in heavy-ion fragmentation. *Physical Review C—Nuclear Physics*, 88(4):041602, 2013.

[89] T. Mukoyama. Electron shake probability for arbitrary shell. *X-Ray Spectrom*, 52, 2023.

[90] J.A. Winger, B.M. Sherrill, and D.J. Morrissey. Intensity: a computer program for the estimation of secondary beam intensities from a projectile fragment separator. *Nuclear Instruments and Methods in Physics Research Section B: Beam Interactions with Materials and Atoms*, 70(1):380–392, 1992.

[91] S. Schwarz, G. Bollen, R. Ringle, J. Savory, and P. Schury. The lebit ion cooler and buncher. *Nuclear Instruments and Methods in Physics Research Section A: Accelerators, Spectrometers, Detectors and Associated Equipment*, 816:131–141, 2016.

[92] I. Cox, Z. Y. Xu, R. Grzywacz, W.-J. Ong, et al. Proton shell gaps in $n = 28$ nuclei from the first complete spectroscopy study with frib decay station initiator. *Phys. Rev. Lett.*, 132:152503, Apr 2024.

[93] K. Minamisono, P.F. Mantica, A. Klose, S. Vinnikova, A. Schneider, B. Johnson, and B.R. Barquest. Commissioning of the collinear laser spectroscopy system in the becola facility at nscl. *Nuclear Instruments and Methods in Physics Research Section A: Accelerators, Spectrometers, Detectors and Associated Equipment*, 709:85–94, 2013.

[94] David J Morrissey and Brad M Sherrill. In-flight separation of projectile fragments. *The Euroschool Lectures on Physics with Exotic Beams, Vol. I*, pages 113–135, 2004.

Appendix

Table A.1: ^{198}Pt + ^{9}Be Cross Sections and Errors

Z	A	Cross Section (mb)	Plus Error Bar	Minus Error Bar
70	180	1.80E-03	8.58E-04	1.31E-03
70	181	3.77E-05	1.28E-05	1.41E-05
70	182	3.63E-06	9.87E-07	9.48E-07
71	180	2.14E+00	1.17E+00	1.43E+00
71	181	3.02E-02	1.27E-02	1.90E-02
71	182	1.20E-03	3.65E-04	6.97E-04
71	183	2.20E-04	8.50E-05	2.47E-04
71	184	1.38E-04	3.68E-05	3.55E-05
71	185	1.11E-05	3.17E-06	5.91E-06
71	186	1.80E-05	5.92E-06	6.79E-06
71	187	5.54E-07	1.36E-07	1.50E-07
71	188	6.01E-08	1.60E-08	2.13E-08
71	189	4.02E-08	2.30E-08	2.82E-08
72	184	3.14E-02	1.27E-02	1.93E-02
72	185	2.26E-03	1.10E-03	2.18E-03
72	186	4.31E-04	2.96E-04	9.70E-04
72	187	1.96E-04	5.58E-05	5.57E-05
72	188	3.45E-05	9.94E-06	1.30E-05
72	189	1.36E-05	3.93E-06	4.94E-06
72	190	8.40E-07	1.94E-07	1.83E-07
72	191	1.47E-07	4.27E-08	6.90E-08
72	192	6.92E-08	3.73E-08	6.18E-08
73	185	4.27E-01	1.64E-01	2.90E-01

Table A.1 continued from previous page

Z	A	Cross Section (mb)	Plus Error Bar	Minus Error Bar
73	186	7.95E-02	3.52E-02	7.55E-02
73	187	3.26E-02	1.69E-02	3.62E-02
73	188	3.67E-03	2.35E-03	6.71E-03
73	189	1.21E-03	7.74E-04	2.21E-03
73	190	3.53E-04	8.24E-05	7.82E-05
73	191	1.01E-04	2.41E-05	2.54E-05
73	192	1.13E-05	2.87E-06	3.89E-06
73	193	9.85E-07	2.33E-07	1.59E-07
74	186	2.56E+00	2.07E+00	5.72E+00
74	188	3.67E-01	1.34E-01	1.98E-01
74	189	1.76E-01	7.85E-02	1.60E-01
74	190	7.18E-02	1.91E-02	2.88E-02
74	191	6.33E-03	2.27E-03	3.91E-03
74	192	3.40E-03	1.88E-03	4.33E-03
74	193	4.60E-04	8.83E-05	1.80E-04
74	194	1.29E-04	2.95E-05	5.33E-05
75	188	7.43E+00	4.91E+00	7.14E+00
75	189	5.01E+00	3.10E+00	5.05E+00
75	190	3.98E+00	1.15E+00	1.51E+00
75	191	5.62E-01	2.23E-01	4.08E-01
75	192	2.69E-01	1.29E-01	2.60E-01
75	193	1.07E-01	1.39E-02	2.37E-02
75	194	1.51E-02	5.69E-03	9.42E-03
75	195	9.68E-03	1.97E-03	2.60E-03
76	190	1.77E+01	4.73E+00	1.12E+01

Table A.1 continued from previous page

Z	A	Cross Section (mb)	Plus Error Bar	Minus Error Bar
76	191	4.98E+00	9.34E-01	1.89E+00
76	192	5.54E+00	1.29E+00	3.10E+00
76	193	3.34E+00	1.37E+00	2.85E+00
76	194	1.82E+00	6.04E-01	1.08E+00
76	195	1.07E+00	2.36E-01	3.97E-01
76	196	4.00E-01	7.24E-02	1.59E-01
76	197	4.07E-02	1.46E-02	2.44E-02
77	192	5.17E+01	4.36E+01	2.78E+02
77	193	4.20E+01	2.05E+01	3.03E+01
77	194	2.94E+01	1.28E+01	1.80E+01
77	195	6.45E+01	2.28E+01	2.78E+01
77	196	1.23E+01	6.70E+00	1.54E+01

Table A.2: ^{198}Pt + Ni Cross Sections and Errors

Z	A	Cross Section (mb)	Plus Error Bar	Minus Error Bar
Z	A	CS	CS-	CS+
71	181	7.25E-02	7.25E-02	2.85E-01
71	182	2.26E-02	9.70E-03	1.93E-01
71	183	1.51E-02	5.50E-03	8.81E-02
71	184	4.36E-03	1.43E-03	1.84E-02
71	185	1.32E-03	3.88E-04	3.85E-03
71	186	8.80E-04	4.38E-04	3.84E-03
72	182	N/A	N/A	1.54E-01
72	183	N/A	N/A	2.49E-01
72	184	N/A	N/A	7.51E-02
72	185	3.24E-02	9.38E-03	3.48E-02
72	186	1.38E-02	1.03E-02	2.60E-02
72	187	3.36E-03	2.58E-03	9.87E-03
73	185	N/A	N/A	2.06E-01
73	186	4.77E-02	4.77E-02	2.53E-01
73	187	3.21E-02	3.21E-02	9.68E-02
73	188	5.90E-02	2.41E-02	5.11E-02
73	189	1.47E-02	1.45E-02	6.90E-03
73	190	1.15E-03	1.07E-03	1.17E-02
73	191	8.63E-04	3.37E-04	3.76E-03
74	185	N/A	N/A	2.35E+00
74	186	1.85E+00	1.85E+00	9.30E+00
74	188	6.15E-01	6.15E-01	4.80E-01
74	189	N/A	N/A	1.87E-01

Table A.2 continued from previous page

Z	A	Cross Section (mb)	Plus Error Bar	Minus Error Bar
74	190	N/A	N/A	1.01E-01
74	191	6.29E-02	3.68E-02	2.83E-02
74	192	4.22E-03	4.22E-03	2.23E-02
74	193	3.61E-03	1.26E-03	6.78E-03
74	194	2.17E-03	8.19E-04	8.95E-03
75	187	N/A	N/A	1.75E+01
75	188	N/A	N/A	1.57E+01
75	189	N/A	N/A	1.46E+01
75	191	2.28E+00	2.00E+00	1.69E+00
75	192	1.95E-01	1.95E-01	6.78E-01
75	193	4.36E-01	1.79E-01	2.07E-01
75	194	7.49E-02	7.34E-02	3.42E-02
75	195	1.87E-01	7.52E-02	1.06E-01
75	196	3.29E-02	7.86E-03	1.29E-02
76	190	N/A	N/A	6.87E+01
76	191	1.61E+01	1.14E+01	1.08E+01
76	192	5.50E+00	5.50E+00	3.70E+01
76	193	1.65E+00	1.65E+00	1.10E+01
76	194	2.01E-01	2.01E-01	3.42E+00
76	195	N/A	N/A	3.31E+00
76	196	N/A	N/A	1.30E-01
76	197	2.68E-01	1.42E-01	1.42E-01
77	193	N/A	N/A	5.01E+02
77	194	4.76E-01	4.76E-01	6.53E+01
77	195	3.31E+01	3.31E+01	1.88E+02

Table A.2 continued from previous page

Z	A	Cross Section (mb)	Plus Error Bar	Minus Error Bar
77	196	5.18E+01	5.18E+01	6.23E+03
77	198	N/A	N/A	2.93E+01

Table A.3: Charge state distributions of ions after the FP scintillator (see Fig. 2.1 of Section 2.1) for the 23 mg/cm^2 Be target settings. Calculations were performed for elements from hafnium (Z = 72) to iridium (Z = 77) for several values of Ne_R . The fractions listed in this table are the product of the target and the scintillator fractions for a given charge state.

Z	Ne_R	$Z-q$					
		0	1	2	3	4	5
77	5	1.92e-05	5.38e-03	3.41e-01	3.34e-02	2.49e-03	2.90e-04
	4	1.56e-05	6.36e-03	3.88e-01	3.61e-02	2.27e-03	1.65e-05
	3	2.88e-05	8.59e-03	4.68e-01	3.74e-02	3.04e-04	2.50e-06
	2	5.14e-05	1.38e-02	6.34e-01	1.05e-02	4.63e-05	5.27e-07
	1	5.76e-04	1.03e-01	3.13e-01	4.33e-03	1.79e-05	2.24e-07
	0	1.09e-02	7.82e-02	1.80e-01	2.22e-03	7.82e-06	7.62e-08
76	5	0.00e+00	6.57e-03	3.54e-01	3.04e-02	2.05e-03	2.18e-04
	4	2.45e-05	8.14e-03	3.98e-01	3.15e-02	1.95e-03	1.18e-05
	3	4.27e-05	1.04e-02	4.73e-01	3.34e-02	2.46e-04	2.51e-06
	2	6.85e-05	1.63e-02	6.31e-01	8.71e-03	5.34e-05	4.57e-07
	1	6.67e-04	1.14e-01	3.04e-01	3.52e-03	1.93e-05	0.00e+00
	0	1.29e-02	8.51e-02	1.71e-01	1.72e-03	1.17e-05	0.00e+00
75	7	1.26e-05	6.28e-03	3.07e-01	2.46e-02	1.70e-03	-
	6	1.83e-05	7.09e-03	3.31e-01	2.53e-02	1.59e-03	-
	5	4.19e-05	7.99e-03	3.63e-01	2.62e-02	1.80e-03	-
	4	4.87e-05	9.93e-03	4.07e-01	2.77e-02	1.61e-03	-
	3	5.03e-05	1.26e-02	4.79e-01	2.86e-02	1.81e-04	-
	2	8.58e-05	1.93e-02	6.25e-01	7.44e-03	3.06e-05	-
	1	9.26e-04	1.26e-01	2.95e-01	2.82e-03	1.54e-05	-
	0	1.56e-02	9.18e-02	1.61e-01	1.50e-03	1.00e-05	-

Continued on next page

Table A.3 continued from previous page

Z	Ne_R	$Z-q$					
		0	1	2	3	4	5
74	7	3.01e-05	8.24e-03	3.49e-01	2.31e-02	1.48e-03	-
	6	4.58e-05	8.83e-03	3.43e-01	2.26e-02	1.38e-03	-
	5	6.12e-05	9.94e-03	3.70e-01	2.32e-02	1.38e-03	-
	4	2.61e-05	1.21e-02	4.12e-01	2.44e-02	1.26e-03	-
	3	8.98e-05	1.57e-02	4.81e-01	2.43e-02	1.57e-04	-
	2	1.59e-04	2.26e-02	6.17e-01	6.15e-03	2.69e-05	-
	1	1.19e-03	1.39e-01	2.83e-01	2.50e-03	6.53e-06	-
	0	1.84e-02	9.93e-02	1.52e-01	1.20e-03	8.80e-06	-
73	7	4.02e-05	9.58e-03	3.25e-01	1.93e-02	1.15e-03	-
	6	6.08e-05	1.06e-02	3.48e-01	1.92e-02	1.14e-03	-
	5	9.12e-05	1.27e-02	3.75e-01	2.00e-02	1.07e-03	-
	4	5.93e-05	1.46e-02	4.16e-01	2.09e-02	1.11e-03	-
	3	1.20e-04	1.85e-02	4.79e-01	2.16e-02	7.70e-05	-
	2	2.16e-04	2.67e-02	6.08e-01	4.96e-03	2.07e-05	-
	1	1.52e-03	1.52e-01	2.70e-01	2.01e-03	4.25e-06	-
	0	2.15e-02	1.07e-01	1.42e-01	9.32e-04	1.90e-06	-
72	5	9.80e-05	1.50e-02	3.79e-01	1.76e-02	9.16e-04	-
	4	7.98e-05	1.77e-02	4.15e-01	1.88e-02	8.71e-04	-
	3	2.29e-04	2.20e-02	4.74e-01	1.88e-02	6.08e-05	-
	2	2.94e-04	3.45e-02	5.53e-01	4.65e-03	1.81e-05	-
	1	2.23e-03	1.65e-01	2.57e-01	1.38e-03	0.00e+00	-
	0	2.60e-02	1.13e-01	1.32e-01	6.46e-04	0.00e+00	-

	Parameters	LISEAA+PGD
Common Parameters	AA Cross Sections Amplitude	0.5172
	dR Correction	5.7
Limiting Temperature	$A = 50$	7.9036
	$A = 150$	4.465
	$A = 250$	2.9413
Gaussian	E^* 0th Order	0
	E^* 1st Order	22.3787
	E^* 2nd Order	1.5825
	$\sigma(E^*)$ 0th	0
	$\sigma(E^*)$ 1st	19.2973
	$\sigma(E^*)$ 2nd	-1.779

Table A.4: Parameter values used to obtain best fit between LISEAA and experimental cross sections of ^{198}Pt + Be. The LISE^{++} documentation should be referenced for detailed definitions of parameters [6, 85]